Compressed Sensing Based Reconstruction Algorithm for X-ray Dose Reduction in Synchrotron Source Micro Computed Tomography

A Thesis Submitted
to the College of Graduate and Postdoctoral Studies
in Partial Fulfilment of the Requirements
for the Degree of Doctor of Philosophy
in the Department of Electrical and Computer Engineering
University of Saskatchewan

By

Seyedali Melli

Permission To Use

In presenting this thesis in partial fulfilment of the requirements for a Postgraduate degree from the University of Saskatchewan, it is agreed that the Libraries of this University may make it freely available for inspection. Permission for copying of this thesis in any manner, in whole or in part, for scholarly purposes may be granted by the professors who supervised this thesis work or, in their absence, by the Head of the Department of Electrical and Computer Engineering or the Dean of the College of Graduate and Postdoctoral Studies at the University of Saskatchewan. Any copying, publication, or use of this thesis, or parts thereof, for financial gain without the written permission of the author is strictly prohibited. Proper recognition shall be given to the author and to the University of Saskatchewan in any scholarly use which may be made of any material in this thesis.

Request for permission to copy or to make any other use of material in this thesis in whole or in part should be addressed to:

Head of the Department of Electrical and Computer Engineering
57 Campus Drive
University of Saskatchewan
Saskatoon, Saskatchewan S7N 5A9 Canada

OR

Dean
College of Graduate and Postdoctoral Studies
University of Saskatchewan
116 Thorvaldson Building, 110 Science Place
Saskatoon, Saskatchewan S7N 5C9 Canada

Acknowledgements

This dissertation would not be possible without the help and support of many people during my studies in Saskatoon. First and foremost, I would like to express my deepest gratitude toward my thesis advisors, Professor Khan Wahid and Professor Paul Babyn, for their criticism, patience, support and guidance through my research program at the University of Saskatchewan.

I would also like to extend my gratitude to Professors Artur Sowa, Aryan Saadat-Mehr, David Cooper and Francis Bui for serving in my doctoral committee. Their insightful advice and comments have improved the quality of this thesis.

I gratefully acknowledge the funding provided by the Saskatchewan Innovation and Opportunity Award and the Department of Electrical and Computer Engineering at the University of Saskatchewan for this PhD study.

I would like to express my deepest appreciation to my parents, my dearest son Edwin and my beloved wife for her understanding, support and encouragement during this long-term study.

Abstract

Synchrotron computed tomography requires a large number of angular projections to reconstruct tomographic images with high resolution for detailed and accurate diagnosis. However, this exposes the specimen to a large amount of x-ray radiation. Furthermore, this increases scan time and, consequently, the likelihood of involuntary specimen movements. One approach for decreasing the total scan time and radiation dose is to reduce the number of projection views needed to reconstruct the images. However, the aliasing artifacts appearing in the image due to the reduced number of projection data, visibly degrade the image quality. According to the compressed sensing theory, a signal can be accurately reconstructed from highly undersampled data by solving an optimization problem, provided that the signal can be sparsely represented in a predefined transform domain. Therefore, this thesis is mainly concerned with designing compressed sensing-based reconstruction algorithms to suppress aliasing artifacts while preserving spatial resolution in the resulting reconstructed image. First, the reduced-view synchrotron computed tomography reconstruction is formulated as a total variation regularized compressed sensing problem. The Douglas-Rachford Splitting and the randomized Kaczmarz methods are utilized to solve the optimization problem of the compressed sensing formulation.

In contrast with the first part, where consistent simulated projection data are generated for image reconstruction, the reduced-view inconsistent real ex-vivo synchrotron absorption contrast micro computed tomography bone data are used in the second part. A gradient regularized compressed sensing problem is formulated, and the Douglas-Rachford Splitting and the preconditioned conjugate gradient methods are utilized to solve the optimization problem of the compressed sensing formulation. The wavelet image denoising algorithm is used as the post-processing algorithm to attenuate the unwanted staircase artifact generated by the reconstruction algorithm.

Finally, a noisy and highly reduced-view inconsistent real in-vivo synchrotron phase-contrast computed tomography bone data are used for image reconstruction. A combination of prior image constrained compressed sensing framework, and the wavelet regularization is formulated, and the Douglas-Rachford Splitting and the preconditioned conjugate gradient methods are utilized to solve the optimization problem of the compressed sensing formulation. The prior image constrained compressed sensing framework takes advantage of the prior image to promote the sparsity of the target image. It may lead to an unwanted staircase artifact when applied to noisy and texture images, so the wavelet regularization is used to attenuate the unwanted staircase artifact generated by the prior image constrained compressed sensing reconstruction algorithm.

The visual and quantitative performance assessments with the reduced-view simulated and real computed tomography data from canine prostate tissue, rat forelimb, and femoral cortical bone samples, show that the proposed algorithms have fewer artifacts and reconstruction errors than other conventional reconstruction algorithms at the same x-ray dose.

Table of Contents

List of Abbreviations

ABI	Analyzer-Based Imaging
ADMM	Alternating Direction Method of Multipliers
ART	Algebraic Reconstruction Technique
ASD-POCS	Adaptive Steepest Descent Projection on to Convex Sets
BMIT-BM	Biomedical Imaging and Therapy Bending Magnet
BPDN	Basis Pursuit Denoising
CLS	Canadian Light Source
CS	Compressed Sensing
CT	Computed Tomography
DEI-CT	Diffraction Enhanced Imaging Computed Tomography
DRS	Douglas-Rachford Splitting
FBP	Filtered Back Projection
HPITRE	High performance PITRE
IID	Independent and Identically Distributed
KES-CT	K-Edge Subtraction Computed Tomography
MFISTA	Monotone Fast Iterative Shrinkage-Thresholding Algorithm
MLEM	Maximum Likelihood Expectation Maximization
NCG	Nonlinear Conjugate Gradient
PICCS	Prior Image Constrained Compressed Sensing
PITRE	Phase-sensitive x-ray Image processing and Tomography Reconstruction
POCS	Projection on to Convex Sets
PPCI	Propagation-based Phase Contrast Imaging
PSNR	Peak Signal to Noise Ratio
RE	Relative Error
RIP	Restricted Isometry Property
SB	Split-Bregman
SD	Steepest Descent
SIRT	Simultaneous Iterative Reconstruction Technique
SR	Sparsity-Regularized

SSIM	Structural SIMilarity
TV	Total Variation
XPC-CT	X-ray Phase Contrast Computed Tomography

List of Figures

List of Tables

1. Introduction

1.1 Introduction

X-ray Computed Tomography (CT) is a non-invasive imaging technique where projections taken from different viewing angles are computer processed to reconstruct the tomographic image of the scanned object. Micro-CT scanners using synchrotron radiation sources can provide higher spatial resolution than conventional CT. An additional benefit of synchrotron scanner is that x-rays generated at synchrotron beamline are almost parallel and monochromatic which reduces noise and artifacts. Synchrotron x-rays are highly intense which boosts the signal to noise ratio allowing shorter scan times. Consequently, the advantages of synchrotron micro-CT scanner including shorter scan time, fewer artifacts/noise and higher spatial resolution makes this imaging method an important non-invasive inspection tool for biological research.

1.2 Research Motivation and Objectives

Traditionally, synchrotron tomographic reconstruction techniques require a large number of projection views to reconstruct synchrotron micro-CT images with the fine spatial resolution necessary to view as much detail as possible in the sample field of view. This exposes the specimen to a large amount of x-ray radiation which can damage living specimens. Furthermore, this increases scan time and consequently the likelihood of involuntary specimen movements so the presence of motion artifact in the reconstructed images will be more likely. One way to reduce the total scan time and radiation dose is to reduce the time of radiation at each projection, in fact, this is the only parameter that can be used to control the amount of synchrotron radiation used for each projection at each angle as the radiation intensity is almost constant per projection. However, detector sensitivity and readout speed may not allow the exposure time per projection to be less than a certain value. Also, a noisy tomographic image will be reconstructed in a low exposure time per projection because of the reduced projection signal to noise ratio. Another approach for decreasing the total scan time and radiation dose is to reduce the number of projections needed to reconstruct the tomographic images. Lately, Compressed Sensing (CS) theory has spurred great interest in the signal-processing research community. According to this theory, a signal can be reconstructed from undersampled data by solving an optimization problem, provided that the signal can be sparsely represented in a predefined frame such as wavelet or gradient. At present, solution of very large-scale CS optimization problems is poorly characterized with real tomographic data which motivates us to propose fast-convergent CS-based synchrotron micro-CT reconstruction algorithms. Using the proposed reconstruction algorithms to reduce the number of projections in synchrotron micro-CT is an effective way to reduce overall x-ray dose and scan time which improves in-vivo imaging protocols.

The main goal in this research project is to develop compressed sensing based reconstruction algorithms and to consider their application in reducing x-ray dose in synchrotron micro computed tomography while reconstructing higher quality tomography images than the ones reconstructed by the existing reconstruction algorithms. Considering the existing literature and application need, we set the following research objectives:

- In order to develop CT reconstruction algorithms tailored for synchrotron imaging, the properties of synchrotron images, datasets and imaging techniques should be identified.
- The proposed algorithms should be able to reduce overall radiation dose by reducing the number of projections needed and/or exposure time per projection.
- The proposed algorithms should be able to suppress aliasing artifacts and/or noise appear in image typically reconstructed when reducing the number of projections and/or exposure time per projection.
- The proposed algorithms should be able to preserve detailed information in the image as much as possible.
- The quality of reconstructed images measured using mathematical methods should be higher than the quality of images reconstructed by existing algorithms.

1.3 Organization of the Thesis

This thesis is organized in a manuscript-based style. The results obtained are included in the form of published manuscripts. In each chapter, a brief introduction precedes each manuscript in order to connect the manuscript to the main context of the thesis. The thesis is organized as follows.

There are six chapters in total. The first chapter gives the motivation for the research and states the research objectives.

Chapter 2 introduces x-ray computed tomography and the mathematical background behind the analytical and algebraic tomographic reconstruction methods and the compressed sensing-based tomography reconstruction techniques are discussed. Furthermore, the synchrotron CT imaging techniques and the freeware programs available for use in phase contrast computed tomography reconstruction are reviewed.

The manuscript included in Chapter 3 proposes a compressed sensing based reduced-view image reconstruction algorithm to reconstruct the tomographic image from simulated synchrotron CT data. The goal is to suppress the aliasing artifacts which appear in the image because of reducing the number of projections. Poor conditioning of reduced-view synchrotron CT projection matrix and processing of large synchrotron CT data are numerical challenges which are addressed in this study. Total variation regularization and a combination of Douglas-Rachford Splitting and randomized Kaczmarz methods are used to solve these numerical issues. Visual assessment and quantitative performance evaluations of a reconstructed abdomen phantom and a reconstructed slice of a canine prostate tissue demonstrate the effectiveness of the proposed algorithm compared to other existing algorithms.

Chapter 4 includes a manuscript that proposes a compressed sensing algorithm for reduced-view image reconstruction from real ex-vivo synchrotron absorption contrast micro-CT bone data. The goal is to reduce the scan time by further reducing the number of projections needed. In contrast with chapter 3, where consistent simulated projection data are generated and used for the image reconstruction, data inconsistency caused by noisy and reduced-view projection data is addressed in this chapter. In addition to data inconsistency, staircase artifact and long reconstruction time are other image reconstruction challenges addressed in this study. The gradient-based compressed sensing algorithm enforces consistency with the noisy and reduced-view projection data and help to attenuate the aliasing artifact and recover the spatial resolution. The post-processing 2D wavelet-based image denoising algorithm is used to attenuate the unwanted staircase artifact generated by the gradient-based compressed sensing algorithm while preserving the recovered spatial resolution. The conjugate gradient method and a modified back-projection operator are used to decrease the reconstruction time. Visual and quantitative-based performance assessments of a reconstructed slice of a femoral cortical bone sample demonstrate the superiority of the proposed algorithm compared to other existing algorithms.

The manuscript included in Chapter 5 proposes a compressed sensing algorithm for reduced-view image reconstruction from real in-vivo synchrotron phase contrast CT bone data. The goal is to reduce the radiation dose and scan time by reducing the number of projections. The in-vivo phase contrast projection dataset used in this chapter is noisier than the absorption contrast micro-CT projection dataset used for the ex-vivo study proposed in Chapter 4. Furthermore, the number of acquired projections and the radiation exposure time per projection are less than the values set for the ex-vivo study. A multi-regularization constraint compressed sensing algorithm is proposed in this chapter to address the image reconstruction challenges including highly reduced-view and noisy projection data. The prior image constrained compressed sensing framework takes advantage of a prior image to promote sparsity of target image. The gradient transformation has been shown to work well when dealing with piecewise smooth images, it may lead to unwanted staircase artifact when applied to images that contain textures. The 2D wavelet transform is good at capturing point singularities and textures, but not as good for approximating piecewise smooth regions because it penalizes jumps and causes oscillations around edges. The research presented in this chapter is focused on proposing a wavelet-gradient based prior image constrained compressed sensing algorithm to enforce consistency with the highly reduced-view and noisy projection data and at the same time attenuating the aliasing, staircase and ringing artifacts while preserving piecewise smooth regions with sharp edges, point singularities, and textures. Visual and quantitative-based performance assessments of reconstructed slices of a rat forelimb sample demonstrate the advantage of the proposed algorithm compared to other existing algorithms in suppressing artifacts and noise appear in the image and preserving detailed information.

Finally, Chapter 6 summarizes the thesis and suggests potential research problems for future work.

2. Background

2.1 X-Ray Computed Tomography

X-ray Computational Tomography is a non-destructive imaging technique typically used to image specimen morphology. X-ray projections are generated on the x-ray sensors located on the opposite side of the object, either the object is rotating between the x-ray source and the sensors, or the x-ray source-sensors unit is rotating around the object. As the integral of the attenuation coefficient along the x-ray path forms the projections on the sensors, understanding the physics of x-ray interaction with matter is essential and is presented in brief here. Assume that there is a beam of x-ray photons propagating through a piece of material. The beam intensity attenuates because photons either being absorbed by the material atoms or by being scattered away from their traveling path. The Photoelectric Absorption and the Compton Scattering effects, respectively, are the mechanisms contributing to this beam intensity attenuation for the range of photon energies used for the diagnostic imaging (from 20 to 150 keV). Photoelectric Absorption effect consists of an x-ray photon giving its entire energy to a firmly bound inner electron in an atom. The electron utilizes part of this attained energy to overcome the binding energy inside its shell, and the remainder appears as the kinetic energy of the freed electron. The Compton Scattering effect, on the other hand, consists of the interaction of the x-ray photon with either a free electron or an electron lightly coupled to one of the exterior shells of an atom. This interaction results in deflection of the x-ray photon from its traveling path and loss of its energy, which is acquired by the electron. Both the Photoelectric Absorption and the Compton Scattering effects show energy dependency meaning that the likelihood of a photon to be lost from its traveling path because of either absorption or scattering is a function of the energy of that photon. The energy dependency of photoelectric absorption effect is higher than the Compton Scattering effect [C2.1].

Assume x-ray beams are of the same energy and $\mu(x, y)$ represents the x-ray attenuation coefficient distribution of tissue of a 2D object and let l represents the zero width straight x-ray path (no refraction or diffraction) from the x-ray focal spot to the detector pixel. The emitted x-ray photons are attenuated by the materials in the target object. According to Beer's law, the detected photon number I at a given sensor and the entering photon number I_0 have the following relationship [C2.2]:

$$I = I_0 \, exp\left(-\int_l \mu(x,y)dl\right) \tag{2.1}$$

Where the line integral is performed along the x-ray path. Alternatively, one can define:

$$y = \int_l \mu(x,y)\, dl = ln\left(\frac{I_0}{I}\right) \tag{2.2}$$

Where y is the so-called sinogram. Then the image reconstruction process consists of estimating the attenuation coefficients, μ, from the detected sinogram y. In digital implementation, the attenuation coefficients are digitized into the so-called pixel representations:

$$\mu(x,y) = \sum_{i \in S} \mu_i \omega_i(x,y) \tag{2.3}$$

Where S denotes the index of the set of N pixel locations, i is the pixel index, and $\omega_i(x,y)$ is the basis function. Substituting (2.3) into the line integral equation in (2.2), one can obtain:

$$y = \sum_{i \in S} \mu_i \int_l \omega_i(x,y)\, dl = \sum_{i \in S} A_{ji}\, \mu_i = A\mu \tag{2.4}$$

Where the system matrix A is given by:

$$A_{ji} = \int_{l_j} \omega_i(x,y)dl \tag{2.5}$$

Which is the line integral of the basis function $\omega_i(x,y)$ along the j_{th} x-ray path. The system matrix is only dependent on the CT scanner [C2.3]. While a CT scanner computes the linear attenuation coefficient of the tissue (at some effective energy), the numbers shown by the computer connected to the scanner are integers with values typically in the range of -1000 to 3000. These integers have been termed Hounsfield Units symbolized by HU. The relation between the linear attenuation coefficient and the equivalent Hounsfield Unit is:

$$H = \frac{\mu - \mu_{water}}{\mu_{water}} \times 1000 \tag{2.6}$$

Where H = 0 corresponds to the water attenuation coefficient and H = -1000 corresponds to $\mu = 0$, which is the air attenuation coefficient.

2.2 Mathematical Background of X-Ray CT

We are ready to introduce some mathematical tools that will be central to solving for the attenuation coefficient in Eq. (2.4).

2.2.1 Radon Transform

The Radon transform of a function $\mathrm{R}\mu(z) : R^2 \to R$ is defined by:

$$[\mathrm{R}\mu(z)](t,\theta) := \int_{l_{t,\theta}} \mu(z)\, dl \tag{2.7}$$

Where a point z on the line $l_{t,\theta}$ can be described as follows:

$$l_{t,\theta} = \{z{:}\langle z, \Omega\,(\theta)\rangle = t\} = \{t\Omega(\theta) + s\Psi(\theta){:}\, s \in R\} \tag{2.8}$$

$\langle .\,,.\rangle$ denotes the inner product in R^2. The t and θ parameters determine a specific line $l_{t,\theta}$ and s determines specific point on that line. The variable t is the orthogonal distance from the line $l_{t,\theta}$ to the origin. $\Psi(\theta) = (-sin(\theta), cos(\theta))$ is the unit vector which is aligned along the line $l_{t,\theta}$ and is perpendicular to the unit vector $\Omega(\theta) = (cos\,\theta\,, sin\,\theta)$ (see Fig. 2.1). We can imagine that the combination of t and θ define the line $l_{t,\theta}$ in the plain and as s varies we can move along the line.

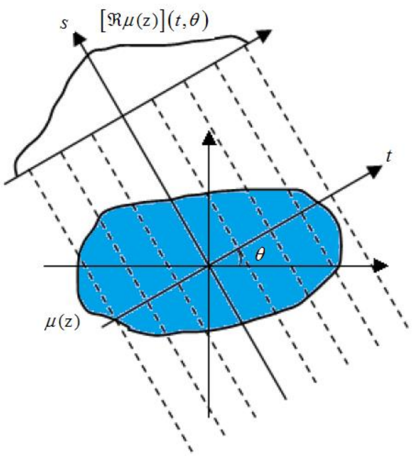

Figure 2.1 Object $\mu(z)$ and its projection are shown for an angle of θ

This parametric representation of the line $l_{t,\theta}$ gives the following formula:

$$\mathrm{R}\mu(t,\theta) := \int_{s\in R} \mu(t\cos\theta - s\sin\theta\,, t\sin\theta + s\cos\theta) ds \tag{2.9}$$

The goal is to find some type of inversion formula for the Radon transform that will allow us to recover attenuation coefficient μ.

2.2.2 Central Slice Theorem

The Central Slice Theorem, also known as the Fourier Slice Theorem, is the fundamental analytical tomography reconstruction method. It states that one dimensional Fourier transform of the object projection data obtained at the angle θ is equal to one slice of the two-dimensional Fourier transform of the object which passes through the center at the same angle [C2.4, C2.5]. Based on this theorem, it is possible to reconstruct the scanned object by performing a two-dimensional inverse Fourier transform, as shown in Figure 2.2.

To derive the Central Slice Theorem, the two-dimensional Fourier transform $F(u,v)$ of the object $\mu(x,y)$ can be defined as:

$$F(u,v) := \int_{-\infty}^{+\infty}\int_{-\infty}^{+\infty} \mu(x,y)\, e^{-i2\pi(xu+yv)}\, dx\, dy \tag{2.10}$$

The line integration in the Eq. (2.7) can be rewritten as the integration of the $\mu'(t,s)$ along the s axis:

$$P_\theta(t) = \int_{-\infty}^{+\infty} \mu'(t,s)\, ds \tag{2.11}$$

$P(\omega,\theta)$ is defined as the Fourier transform of $P_\theta(t)$:

$$P(\omega,\theta) = \int_{-\infty}^{+\infty} P_\theta(t)\, e^{-i2\pi\omega t} dt \tag{2.12}$$

$$= \int_{-\infty}^{+\infty}\int_{-\infty}^{+\infty} \mu'(t,s)\, ds\, e^{-i2\pi\omega t}\, dt$$

$$= \int_{-\infty}^{+\infty}\int_{-\infty}^{+\infty} \mu'(t,s)\, e^{-i2\pi\omega t}\, ds\, dt$$

The coordinates (t,s) can be converted to the Cartesian coordinates by the following equations:

$$t = x\cos\theta + y\sin\theta\,;\ s = -x\sin\theta + y\cos\theta \tag{2.13}$$

$$dtds = Jdxdy = \begin{vmatrix} \frac{\partial t}{\partial x} & \frac{\partial s}{\partial x} \\ \frac{\partial t}{\partial y} & \frac{\partial s}{\partial y} \end{vmatrix} dxdy \tag{2.14}$$

$$= \begin{vmatrix} \cos\theta & -\sin\theta \\ \sin\theta & \cos\theta \end{vmatrix} dxdy = dxdy$$

where J is the Jacobian determinant. Using Eqs. (2.12), (2.13) and (2.14), we have

$$P(\omega,\theta) = \int_{-\infty}^{+\infty}\int_{-\infty}^{+\infty} \mu(x,y)\, e^{-i2\pi\omega(x\cos\theta + y\sin\theta)}\, d\,xdy \tag{2.15}$$

Two Eqs. (2.10) and (2.15) are equal if $u = \omega\cos\theta$ and $v = \omega\sin\theta$, which means:

$$F(\omega\cos\theta\,,\omega\sin\theta) = P(\omega,\theta) \tag{2.16}$$

The variables $u = \omega\cos\theta$ and $v = \omega\sin\theta$ define a line that passes through the origin and has the angle θ with reference to the positive u axis.

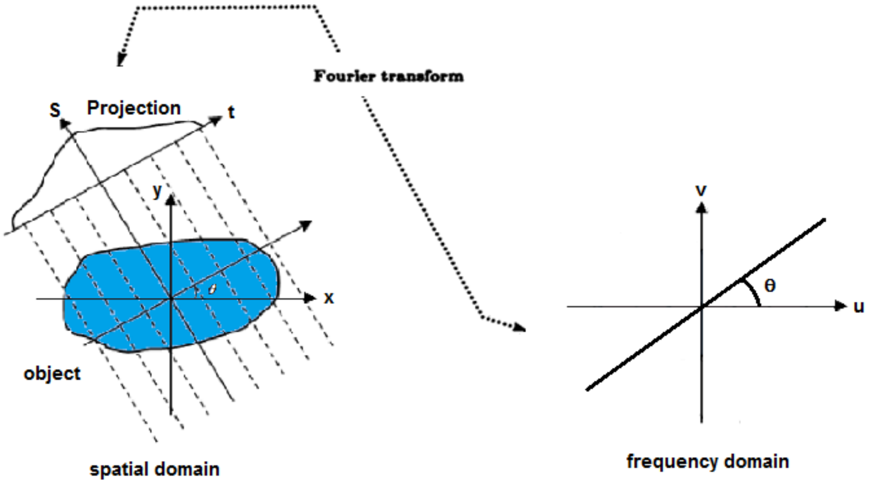

Figure 2.2 Fourier transform of a projection at the angle θ is equal to a slice of the two-dimensional Fourier transform of that object which passes through the origin at the same angle

2.3 Filtered Back Projection (FBP)

The Fourier Slice Theorem states that the 1D Fourier transform of each projection is a slice of the 2D frequency domain. Combining all these slices from all equiangular projection data form concentric circles in the frequency domain, as shown in Fig 2.3. Interpolation is necessary to fill the unknown frequency values in the Cartesian grid and then 2D Inverse Fourier transform is used to reconstruct the image. However, interpolation error in the frequency domain spreads in the spatial domain and results in some image degradation.

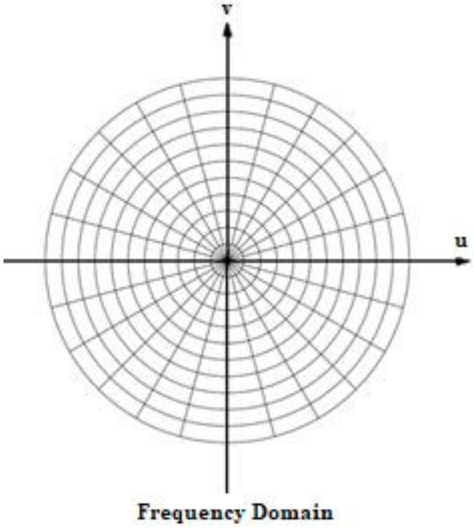

Figure 2.3 The intersection of radial lines with the concentric circles represents the frequency samples obtained from 1D Discrete Fourier transform of projection data

Filtered back projection (FBP) method avoids the interpolation error and is fast so that it has become the standard reconstruction method in clinical CT.

The image function $\mu(x, y)$, is derived by performing the inverse Fourier transform on $F(u, v)$:

$$\mu(x, y) = \int_{-\infty}^{+\infty} \int_{-\infty}^{+\infty} F(u, v)\, e^{i2\pi(xu+yv)}\, d\, udv \qquad (2.17)$$

We know from the last section:

$$u = \omega \, cos \, \theta \, ; v = \omega \, sin \, \theta \qquad (2.18)$$

And,

$$dudv = Jd\omega d\theta = \begin{vmatrix} \frac{\partial u}{\partial \omega} & \frac{\partial v}{\partial \omega} \\ \frac{\partial u}{\partial \theta} & \frac{\partial v}{\partial \theta} \end{vmatrix} d\omega d\theta \qquad (2.19)$$

$$= \begin{vmatrix} cos\, \theta & sin\, \theta \\ -\omega\, sin\, \theta & \omega\, cos\, \theta \end{vmatrix} d\omega d\theta = \omega d\omega d\theta$$

Eq. (2.20) can be derived by combining Eqs. (2.16), (2.17), (2.18) and (2.19):

$$\mu(x,y) = \int_0^{2\pi}\int_0^{+\infty} F(\,\omega\cos\theta\,,\omega\sin\theta)\,e^{i2\pi\omega(x\cos\theta+y\sin\theta)}\,\omega\,d\omega d\theta \tag{2.20}$$

$$= \int_0^{2\pi}\int_0^{+\infty} P(\omega,\theta)\,e^{i2\pi\omega(x\cos\theta+y\sin\theta)}\,\omega\,d\omega\,d\theta$$

$$= \int_0^{\pi}\int_0^{+\infty} P(\omega,\theta)\,e^{i2\pi\omega(x\cos\theta+y\sin\theta)}\,\omega\,d\omega\,d\theta$$

$$+ \int_0^{\pi}\int_0^{+\infty} P(\omega,\theta+\pi)\,e^{i2\pi\omega(x\cos(\theta+\pi)+y\sin(\theta+\pi))}\,\omega\,d\omega\,d\theta$$

$P_{\theta+\pi}(t) = P_\theta(-t)$ results in from the symmetrical property of parallel beam geometry. Eq. (2.20) can be rewritten as Eq. (2.21) by substituting $P(\omega,\theta+\pi) = P(-\omega,\theta)$ in the equation:

$$\mu(x,y) = \int_0^{\pi}\int_{-\infty}^{+\infty} P(\omega,\theta)|\omega|\,e^{i2\pi\omega(x\cos\theta+y\sin\theta)}\,d\,\omega\,d\theta \tag{2.21}$$

$$= \int_0^{\pi}[\int_{-\infty}^{+\infty} P(\omega,\theta)|\omega|\,e^{i2\pi\omega t}\,d\,\omega]d\theta$$

The inner integral of Eq. (2.21) is the Inverse Fourier transform of $P(\omega,\theta)|\omega|$. In practice, the ideal filter,$|\omega|$, is approximated by the “Ram-Lak” filter, as shown in Figure 2.4. Although the Ram-Lak filter is the best approximation to the ideal filter, it amplifies the high-frequency noise and is discontinuous in the frequency domain. Therefore, other filters such as Hamming, or Shepp-Logan filters are proposed to preserve small features in the image while attenuating high-frequency noise.

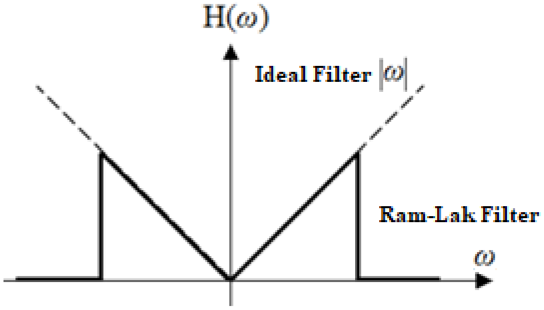

Figure 2.4 The Ram-Lak filter is used to approximate the ideal filter response

We denote $g(t)$ as the Inverse Fourier transform of $P(\omega,\theta)|\omega|$ which is equal to the convolution of $P_\theta(t)$ and $f(t)$:

$$g(t) = \int_{-\infty}^{+\infty} P(\omega,\theta)|\omega|\, e^{i2\pi\omega t}\, d\,\omega \tag{2.22}$$

$$g(t) = P_\theta(t) \otimes f(t) \tag{2.23}$$

Where $f(t)$ and $P_\theta(t)$ are the inverse Fourier transform of $|\omega|$ and $P(\omega,\theta)$ respectively, variable t is the orthogonal distance from the line $l_{t,\theta}$ to the origin and $\otimes$ is the convolution operator. After combining Eqs. (2.21) and (2.22), we have:

$$\mu(x,y) = \int_0^\pi g(t)d\theta \tag{2.24}$$

Eq. (2.24) is the Filtered Back Projection formula as it states that the value of a point (x,y) in the spatial domain is determined by the summation of all filtered projection samples passing through the point (x,y).

2.4 Aliasing Distortion

The distortions that occur due to undersampling of projection data or because not enough projection data are collected are termed the aliasing distortions. Fig. 2.5 shows parallel beam reconstructions of a Shepp-Logan phantom with different number of projections (K) and 256 number of rays in each projection (N). The original image size is 256 x 256 pixels and the images in Fig. 2.5 are displayed on a 256 x 256 matrix.

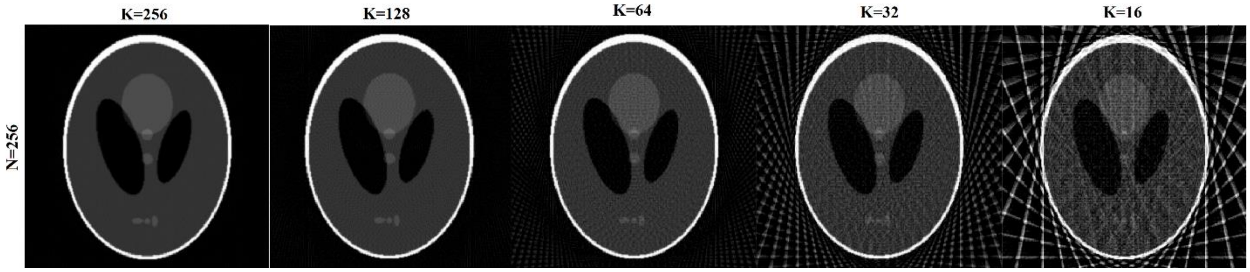

Figure 2.5 Aliasing distortion in the reconstructed images of a Shepp-Logan phantom is shown for different number of projections

It can be proved analytically that the number of projections should be roughly N and the number of rays in each projection should also be roughly N to reconstruct a distortion-free $N \times N$ image.

Based on the Fourier Slice Theorem, each radial line in the frequency domain, such as the AC line shown in Fig. 2.6 is generated by one dimensional Fourier transform of the corresponding projection data.

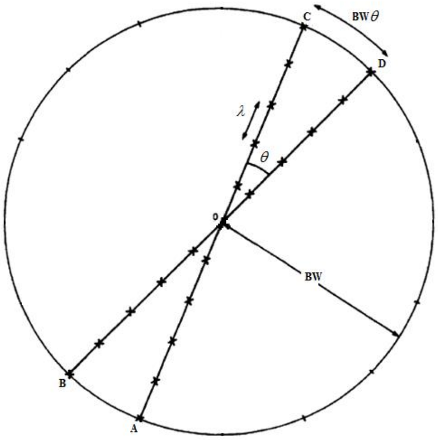

Figure 2.6 Frequency domain representation of parallel projection data

The angular interval θ between the radial lines, if K_{proj} projections are uniformly distributed over 180°, is given by:

$$\theta = \frac{\pi}{K_{proj}} \tag{2.25}$$

The spatial frequency bandwidth BW of each projection shown as the disk radius in Fig 2.6 is given by:

$$BW = \frac{1}{2\tau} \tag{2.26}$$

Where τ is the spatial sampling interval of the projections. The distance between the successive sampling points on the edge of the disk, the azimuthal resolution, is equal to CD and is given by

$$CD = BW\theta = \frac{1}{2\tau}\frac{\pi}{K_{proj}} \tag{2.27}$$

The number of sampling points in the frequency domain along the line AC is equal to N_{ray} the number of sampling points in each projection. Therefore, distance λ, the radial resolution, on the radial lines is:

$$\lambda = \frac{2BW}{N_{ray}} = \frac{1}{\tau N_{ray}} \tag{2.28}$$

The azimuthal resolution should be roughly equal to the radial resolution in the frequency domain. Using Eqs. (2.27) and (2.28) we will have:

$$\frac{1}{2\tau}\frac{\pi}{K_{proj}} \approx \frac{1}{\tau N_{ray}} \tag{2.29}$$

After rearranging Eq. (2.29):

$$\frac{K_{proj}}{N_{ray}} \approx \frac{\pi}{2} \tag{2.30}$$

Which indicates the number of projections should be approximately equal to the number of rays in each projection [C2.1].

2.5 Algebraic Reconstruction Algorithms

A large number of projections uniformly distributed over 180° or 360° are required for the Filtered Back Projection (FBP) method to produce an image with the accuracy desired in medical imaging. There are situations where it is not possible to meet these requirements.

In these situations, the linear system (2.4) can be solved by the following iterative algorithm which is called Simultaneous Iterative Reconstruction Technique (SIRT), which is used to solve large and sparse systems [C2.6, C2.7]:

$$\mu(k+1) = \mu(k) + \eta(k)\, A^T(\, y - A\mu(k)) \tag{2.31}$$

Where A is M × N system matrix, μ represents the x-ray attenuation coefficient, y is the sinogram and $\eta(k)$ is a symmetric positive definite matrix, with upper bounded eigenvalues to ensure the stability of the algorithm. In the special scalar case, the learning rate $\eta(k)$, should satisfy the constraint $0 \leq \eta(k) \leq \lambda_{max}^{-1}$ where λ_{max} is the maximum eigenvalue of $A^T A$. Generally, the algorithm converges faster if the learning rate is near the upper limit. A further increase of convergence speed can be obtained by applying the block iterative version of the algorithm. We obtain the block iterative algorithms by partitioning the dataset y into (not necessary disjoint) subsets St, t = 1,2,…,T. In extreme case for T = 1, Algebraic Reconstruction Technique (ART) which also called Kaczmarz algorithm, will be obtained. This algorithm will iterate through the set of equations in a periodic fashion and can be written as:

$$\mu(k+1) = \mu(k) + \eta(k)\frac{y_i - a_i^T\mu(k)}{a_i^T a_i}a_i \quad i = k \quad module \quad M+1 \tag{2.32}$$

Where M is the total number of rays, $0 < \eta_k < 2$ and at each iteration, we use only one row of A and a corresponding component of y successively [C2.8].

In the special two-dimensional case, the procedure starts with an initial guess. It is projected on the first line, then projecting on the second line, and projecting back onto the first line and so on.

The iterations converge to the intersection point of the lines. If the lines are perpendicular, the iterations converge in two steps. In contrast, a large number of iterations are required to find a solution if the lines are nearly parallel. The angle between the lines has a significant impact on the rate of convergence [C2.1, C2.9].

The solution does not converge to a unique point and oscillates around the intersections of the lines when the system is overdetermined i.e.; there are more lines than unknowns. On the other hand, an infinite number of solutions are possible when the system is underdetermined i.e., there are fewer lines than unknowns. Suppose there is only one line then the solution is the point on the line which is closest to the initial point [C2.7].

In addition to the computational efficiency, algebraic reconstruction algorithms can integrate prior information into the solution. For example, we know that image pixel values are nonnegative, then in each iteration, the negative pixel values may be set to zero. As another example, if image pixel values are zero outside an interest region, this information can be incorporated in the iterations.

2.6 Compressed Sensing Theory

The idea of compressed sensing is to use the low-information content of most real-life signal and reconstruct signal without (or with a small) degradation in quality from undersampled data by a non-linear reconstruction procedure [C2.10, C2.11]. In general, if you know that the signal is sparse or compressible in a known transform domain and undersampling causes incoherent (noise like) aliasing artifact, then Nyquist's limit does not apply. In this section we briefly review CS. Let x be a vector of N samples of a real-valued, discrete-time random process.

$$x = \Psi s = \sum_{i=1}^{N} s_i \Psi_i \tag{2.33}$$

Where $s = [s_1, s_2, \ldots, s_N]$ is the weight vector $s_i = < \Psi_i, x >$ and $\Psi = [\Psi_1 | \Psi_2 | \ldots \Psi_N]$ is an N × N basis matrix with Ψ_i being the i$^{\text{th}}$ basis column vector. Vector x is considered K-sparse, if only K out of N elements of S are non-zero. Most natural signals can approximately be considered as a sparse i.e., compressible because they have many non-significant (close to zero) coefficients in domains other than the spatial domain such as discrete cosine, wavelet or gradient domains.

Let y be an M-length measurement vector given by:

$$y = \Phi x \tag{2.34}$$

Where $K < M \ll N$ and Φ is M × N measurement matrix. Eq. (2.34) is an underdetermined equation, so there are an infinite number of solutions that satisfy the equation. However, signal S can be uniquely reconstructed from M measurements if the measurement matrix Φ is properly designed, i.e. if $A = \Phi\Psi$ satisfies the Restricted Isometry Property (RIP) [C2.12]. In other words, it means that all sub-matrices of $A = \Phi\Psi$ with at most K columns are well-conditioned.

Exact reconstruction of s by minimizing the l_0 norm (the number of non-zero elements) is both numerically unstable and NP-complete. Surprisingly, the convex optimization based on the l_1 norm known as "Basis Pursuit" can exactly recover the K-sparse signal with high probability using (2.35) if $M \geq cK\,log(\frac{N}{K})$:

$$\hat{s} = \underset{s}{argmin}\|s\|_1\, s.t. \quad y = \Phi\Psi s \tag{2.35}$$

In practical situations, we cannot assume that $y = \Phi x$ is known with arbitrary precision in presence of noisy data and modeling error. More appropriately, we will assume instead $y = \Phi x + e$, where e is an unknown perturbation bounded by a known value $\|e\|_2^2 < \varepsilon$. To be broadly applicable, the recovery procedure must be stable i.e. small changes in measurement vector should result in small changes in the reconstructed signal. As a result, a modified convex optimization (2.36) based on the $l1$ norm known as "Basis Pursuit Denoising" can recover the K-sparse signal with an error at most proportional to the noise level [C2.13].

$$\hat{s} = \underset{s}{argmin}\|s\|_1\, s.t. \quad \|y - \Phi\Psi s\|_2^2 < \varepsilon \tag{2.36}$$

In general, calculating RIP is NP-hard and it is only a sufficient and not necessary condition for the accurate recovery in CS problems. A necessary ingredient for accurate recovery in CS is existence of the incoherent aliasing interference in the sparse transform domain. The mutual coherence is a natural tool to measure incoherence. The mutual coherence is defined by:

$$\mu_A = \underset{i \neq j}{max}\frac{|\langle a_i, a_j\rangle|}{\|a_i\|\|a_j\|} \qquad a_i, a_j \text{ are two different columns of } A \in R^{M\times N} \tag{2.37}$$

Aliasing interference between the pixels is zero i.e. the mutual coherence is zero when $i \neq j$ under the Nyquist sampling rate. Undersampling causes interference between the pixels i.e. the mutual coherence is nonzero. A nonlinear reconstruction procedure is illustrated in Fig. 2.7. The procedure is based on thresholding the reconstructed signal to find the strongest component, then subtracting the calculated aliasing interference caused by the strongest component from the reconstructed signal. This resulting reconstructed signal shows a reduced level of aliasing interference and make it possible to threshold the previously hidden weaker components. The other signal components are reconstructed by repeating this procedure.

A one-dimensional sparse signal with three nonzero samples is shown in Fig 2.7(A). A random Gaussian matrix (each entry i.i.d. Gaussian) is used as the measurement matrix. The number of measured samples is M = 22 which is less than signal length N = 32. As illustrated in Fig 2.7(C), in the first iteration, the reconstructed signal is similar to an additive noise (incoherent aliasing). In fact, it is not an additive noise but the leakage due to undersampling causes energy of each nonzero component of the original signal leaks into adjacent bins. This pseudo-randomness eliminates the inherent uncertainty which exists in the uniform sampling. The strongest component is selected, and its calculated interference is subtracted from the reconstructed signal. This procedure is iteratively repeated for three times until all signal components are recovered. As illustrated in Fig. 2.7(F), the reconstructed signal is identical to the original sparse signal shown in Fig 2.7(A). Donoho et al. proposed a fast-approximate CS reconstruction algorithm based on the interference cancellation model [C2.14].

2.7 Compressed Sensing in X-Ray CT

2.7.1 Sparse Features in Spatial Domain

Accurate reconstruction of the vessel tree and simultaneously a great reduction in view-angle sampling can be achieved if volumetrically sparse structure of blood vessels is used to design a CS based iterative reconstruction algorithm [C2.15, C2.16].

The model shown in Eq. (2.38) used an equality constraint forcing the final image to agree with the available measured data and considered a smooth $L_{p=1.1}$ norm minimization of the voxel representation.

$$\min_{X} \quad \|x\|_P^P \quad S.T. \quad y = AX, P = 1.1 \qquad (2.38)$$

An iterative algorithm was used for the above constrained minimization problem which was based on the dual coordinate ascent method. Accurate reconstructions were reported for only 4 to 15 projections which are substantially fewer than the number of projections mentioned in standard CT scanning protocols.

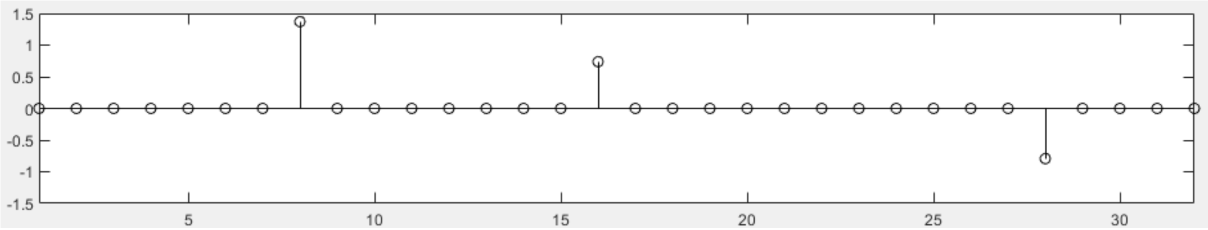

(A) Sparse signal (K = 3, N = 32)

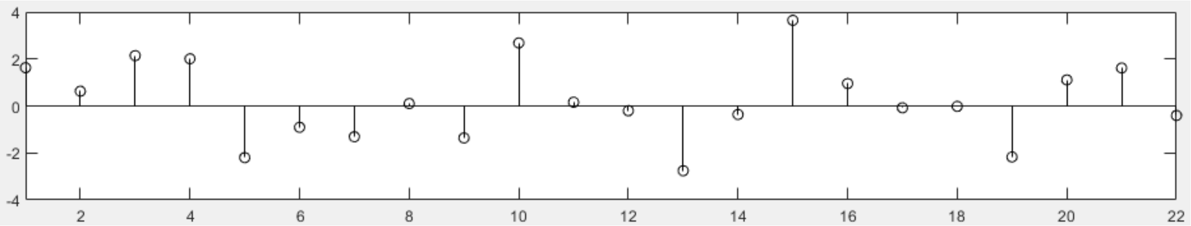

(B) Signal measured by random Gaussian measurement matrix (M = 22)

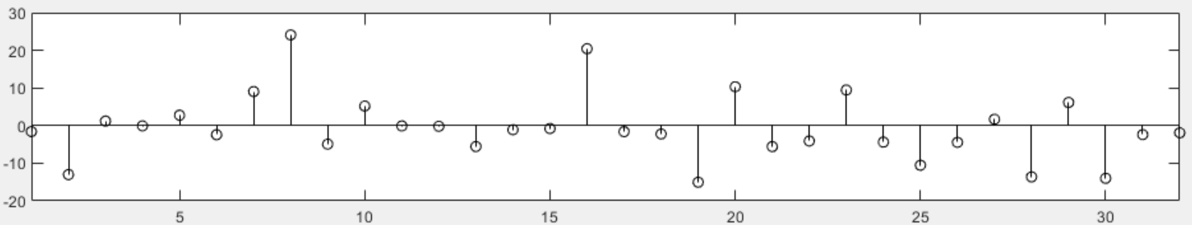

(C) Aliasing interference caused by undersampling

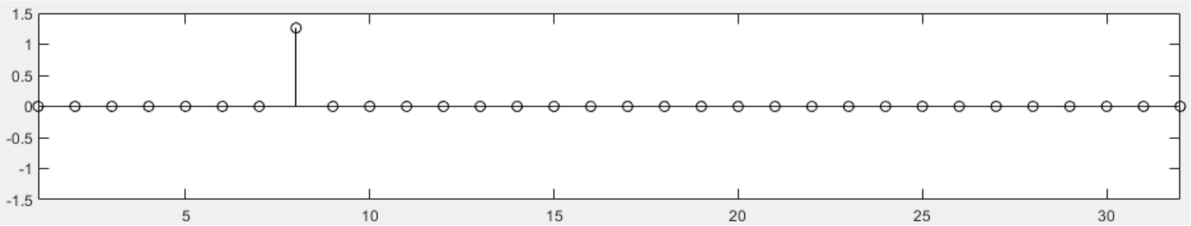

(D) Reconstructed signal in the first iteration

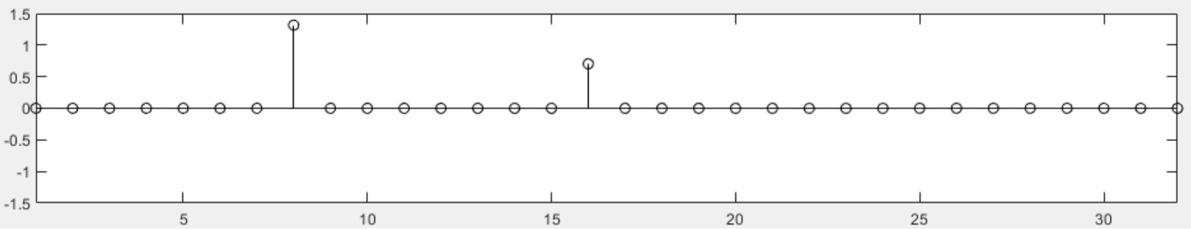

(E) Reconstructed signal in the second iteration

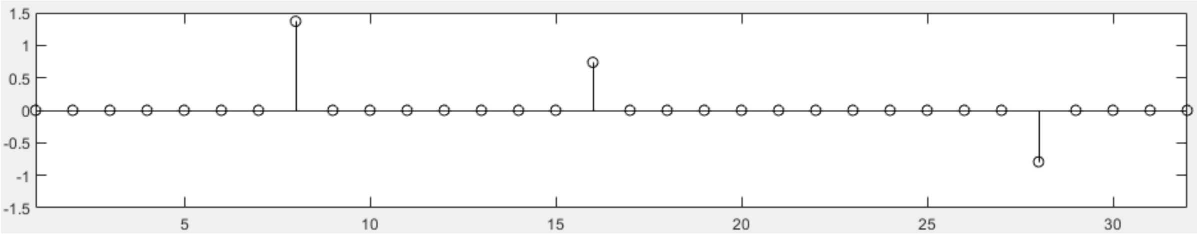

(F) Reconstructed signal in the third iteration

Figure 2.7 Reconstruction of a sparse signal from random undersampling

2.7.2 Prior Image Constrained Compressed Sensing (PICCS)

Some other research efforts have also been done to apply CS to dynamic CT imaging [C2.17]. In dynamic CT imaging, the same image slice is scanned many times to measure the object dynamic changes. In the PICCS method, the FBP algorithm was used to reconstruct a prior image X_P from the union of the interleaved dynamic projection datasets. In this prior image, the static background objects were reconstructed without aliasing artifacts while the dynamic changes in the image were attenuated. The target image was sparsified by the subtraction of prior image containing the aliasing-free static objects from the target image. In addition, the known Total Variation (TV) operator was used to further sparsify the subtracted image $X-X_P$. The following constrained minimization problem is the final cost function of PICCS image reconstruction algorithm:

$$\min_{X} \quad \alpha TV(X - X_p) + (1-\alpha)TV(X) \quad S.T. \quad y = AX \tag{2.39}$$

$TV(X)$ has been used in the PICCS cost function with a relative weight of $1-\alpha$ to mitigate the effect of potential artifacts in the prior image.

The constrained PICCS problem (2.39) was converted to the unconstrained PICCS problem (2.40) to be solved by classical minimization algorithms, given that the gradient of the cost function can be computed [C2.18].

$$\min_{X} \quad \alpha TV\left(X - X_p\right) + (1-\alpha)TV(X) + \lambda \|AX - y\|_{l_2}^2 \tag{2.40}$$

Two algorithms are commonly used to solve multivariate unconstrained minimization problem, Steepest Descent (SD) and Nonlinear Conjugate Gradient (NCG) which offer linear and quadratic rates of convergence, respectively. At each iteration, the above algorithms select a search direction and there are line search methods computing the size of the step to be taken in that direction. Thus, in [C2.18] two line searching algorithms were applied for each minimization algorithm i.e. backtracking (BT) line search and fast Newton-Raphson (NR) line search. Each algorithm was applied to the PICCS objective function (2.40) for 16 different values λ to investigate the convergence speed and reconstruction accuracy. The parameter α was set to 0.5. Based on the results in [C2.18], NCG–NR is the superior algorithm.

In-vivo experimental animal studies were conducted to validate the potential advantage of PICCS algorithm in reducing the dose. The results indicate that PICCS can reconstruct dynamic CT images accurately using 20 view angles, which corresponds to a 32-fold undersampling. The undersampled PICCS image is compared with the fully sampled FBP images with 642 views of projections in [C2.17]. The quality of reconstruction is nearly identical.

The concept of PICCS was extended to other imaging methods using an algorithm called deformable Prior Image Registration, Penalized-Likelihood Estimation (dPIRPLE) [C2.19] where superior reconstruction accuracy was reported using this algorithm as compared to other conventional reconstruction methods. The idea is that the dose can be reduced using prior images from previous studies that contain lots of patient-specific anatomical information. However, patient motion results in misregistration between the prior image and the current anatomy. In [C2.19], a joint registration-reconstruction framework was proposed that estimates the 3D deformation between an unregistered prior image and the current anatomy and reconstructs the current anatomical image using a model-based reconstruction based on the deformed prior image. The main part of this framework is to use a 3D B-spline-based free-form-deformation model. The proposed framework was solved by alternating optimization of both the registration parameters and the reconstructed image.

2.7.3 Adaptive Steepest Descent Projection On to Convex Sets (ASD-POCS)

Another important iterative algorithm, based on compressed sensing, is the work proposed in [C2.20, C2.21]. This algorithm was designed for volume reconstruction from a circular cone-beam scan, but it can also be used in other scanning geometries. The algorithm minimizes the Total Variation (TV) of the reconstructed volume subject to the constraint that the voxels are non-negative and more importantly the estimated projection data should be within a specified tolerance of the available measured data.

Generally, from all images that agree with the data within tolerance ε labeled as region $I(\varepsilon)$, the minimum TV image will be on the boundary of $I(\varepsilon)$. In this algorithm, two image distances dp and dg which are respectively the magnitudes of the change in the image due to POCS and TV-steepest descent, control the reconstruction trajectory i.e. when the current image estimate is outside of $I(\varepsilon)$, dg is controlled to be less than dp and vice versa. The resulting image trajectory terminates at the optimal solution f^* on the boundary of $I(\varepsilon)$.

A comprehensive study of using ASD-POCS for reduced-view reconstruction of real CT data was carried out in paper [C2.22] to verify the performance of the algorithm in mitigating aliasing artifacts in non-ideal practical scenarios. In this study, data were acquired using a bench-top Cone Beam Computed Tomography (CBCT) system that was designed for image-guided surgery and radiotherapy. A spectrum of quantitative performance metrics was applied with the purpose of thoroughly clarifying image quality characteristics of resulting reconstructions, including image noise, correlation, similarity (to a 'true' reference image) and task-based detectability. A full dataset related to the anthropomorphic head phantom was collected at 960 views that are uniformly distributed over 2π. 60 views which are evenly distributed over 2π was extracted from the full dataset to be used in reconstruction of image with a pixel size of 0.045 cm. The average values of ε per ray measurement were chosen to be about 1.7×10^{-5} in the ASD-POCS algorithm. As shown in [C2.22], The ASD-POCS algorithm can reconstruct detailed structures of nasal region of the head phantom that are only observed in the full-view reference image.

In [C2.23], the application of ASD-POCS algorithm in low-dose micro-CT of real animal organs was investigated. The results show that the ASD-POCS algorithm with using only one-sixth to one quarter of the 360-view data currently used in typical micro-CT imaging, can reconstruct images with quality comparable to that obtained with conventional algorithms. The image-quality evaluation was performed by different methods such as visualization-based, quantitative-metric-based, and task-specific evaluation. For example, the segmentation-based evaluation which is one form of task-specific evaluation was carried out by separating the voxels representing two types of distinct materials i.e. contrast-enhanced blood vessels and the rest of the specimen.

The disadvantage of ASD-POCS algorithm is that the convergence of this heuristic algorithm has not been demonstrated theoretically. Also, another problem with this approximate algorithm is that the reconstructed image depends on the parameters of the algorithm itself. More parameters make characterization of the algorithm more difficult.

2.7.4 First-order algorithms for total variation based image reconstruction

The nonsmooth regularizers such as total variation (TV) and sparsity-promoting ones based on the $l1$ -norm [C2.24] are not differentiable everywhere, so, conventional gradient methods (e.g., NCG or SD) employs differentiable approximation (e.g., using "corner-rounding" [C2.24]) which leads to slow convergence [C2.25]. For solving this problem, first-order splitting based algorithms such as (M)FISTA [C2.26, C2.27], and Split-Bregman-type (SB) schemes [C2.28] which can handle nonsmooth regularizers without corner rounding were proposed. In addition, there are other methods such as ADMM [C2.29] and Chambolle-Pock [C2.30, C2.31]. These algorithms are inter-related [C2.32], but there are differences in parameterization which can have significant impact on convergence in practice. Split-Bregman (SB) method converges to a reasonable practically useful precision very fast [C2.33] and was used in reduced-view CT reconstruction algorithm [C2.34]. TV-based reconstruction algorithms such as SB-TV have been shown to work well when dealing with piecewise smooth images [C2.34], but, it may lead to unwanted staircase artifact when applied to images that contain textures and shading [C2.35, C2.36].

2.8 Douglas-Rachford Splitting method

Douglas-Rachford Splitting (DRS) is a simple but powerful method for distributed convex programming which was first proposed in [C2.37]. Much like Newton's method which is a standard tool for solving unconstrained smooth minimization problems of modest size, DRS algorithm can be viewed as an analogous tool for non-smooth, constrained, large-scale problems. The algorithm solves problems in the form:

$$\min_{u\in R^n, v\in R^d} \quad f_1(u)+f_2(v) \quad ST \quad v=Gu \tag{2.41}$$

Where $G \in R^{d\times n}$. The application of this method to the problem at hand will be described in detail in the next chapters. We now recall the theorem by Eckstein and Bertsekas [C2.38], in which convergence of Douglas-Rachford Splitting (DRS) method is shown. This theorem applies to problems with the form Eq. (2.41).

Theorem (Eckstein-Bertsekas): Consider problem (2.41), where f_1 and f_2 are closed, proper convex functions, and $G \in R^{d\times n}$ has full column rank. Consider arbitrary $\mu > 0$ and $v_0, d_0 \in R^d$. Let $\eta_k \geq 0, k=0,1,\ldots$ and $\lambda_k \geq 0, k=0,1,\ldots$ be two sequences such that: $\sum_{k=0}^{\infty}\eta_k < \infty$ and $\sum_{k=0}^{\infty}\lambda_k < \infty$. Consider three sequences $u_k \in R^n,$, $v_k \in R^d$, and $d_k \in R^d, k=0,1,\ldots$ that satisfy:

$$\eta_k \geq \left\| u_{k+1} - (\underset{u}{argmin} f_1(u) + \tfrac{\mu}{2}\|Gu - v_k - d_k\|_2^2) \right\| \tag{2.42}$$

$$\lambda_k \geq \left\| v_{k+1} - (\underset{v}{argmin} f_2(v) + \tfrac{\mu}{2}\|Gu_{k+1} - v - d_k\|_2^2) \right\| \tag{2.43}$$

$$d_{k+1} = d_k + Gu_{k+1} - v_{k+1} \tag{2.44}$$

Then, if (2.41) has a solution, the sequence $\{u_k\}$ converges, $u_k \to u^*$ where u^* is a solution of (2.41). If (2.41) does not have a solution, then at least one of the sequences $\{v_k\}$ or $\{d_k\}$ diverges. One of the important consequences of this theorem is that it shows that it is not necessary to exactly solve the minimization problem in (2.42) and (2.43); as long as sequence of errors is absolutely summable, global convergence is not compromised. The convergence of the DRS method has been demonstrated theoretically so it eliminates the need to study dependence of the image on algorithm parameters; if the final image is the solution of the stated optimization problem the path taken in getting there is irrelevant.

As discussed in [C2.39], the DRS method is more general than the other unconstrained solvers such as steepest descent and nonlinear conjugate gradient in the sense that the cost function does not need to be differentiable or finite so, this algorithm can handle $l1$ regularization which is used in Basis Pursuit Denoising optimization problem (2.36) without corner rounding technique. Another disadvantage of these unconstrained solvers is that they may be quite slow, especially when ε is very small and/or the matrix A is very ill-conditioned (because of reduced-view sampling) that both conditions are true in our case. The spirit of CS-style image reconstruction involves solving unconstraint optimization problem for small ε which is technically challenging. When the slowness is caused by using a small value of ε, continuation schemes have been found quite effective in speeding up the algorithm. The idea is to use the iterative algorithm for a larger value of ε (which is usually fast), then decrease it in steps toward its desired value, running algorithm with warm start for each successive value of ε. The drawback is that as ε becomes very small, the intermediate minimization problems become very ill-conditioned, thus causing numerical problems. On the other hand, DRS method can work with small value of ε without using continuation scheme because in addition to Lagrange term, a quadratic penalty term is also included in the DRS optimization cost function. In addition, DRS algorithm can perform distributive optimization which is useful in solving large-scale problem such as synchrotron CT reconstruction. Firstly, it lets you to break up a larger problem into smaller, more manageable ones and the smaller problems can be solved using any favorite solver. After that the algorithm coordinate these smaller optimization routines to cooperatively solve the primary larger problem.

In [C2.40], several practical problems discussed to show how DRS method or generally proximal operators can be used in practice. Lasso, stochastic optimization, matrix decomposition, robust and risk-averse optimization problems and many others, are some examples in which DRS method can be applied. In [C2.41], the indicator function of the constraint set is used to transfer the BPDN optimization problem (2.36) into an unconstrained convex composite optimization problem, and the DRS method is utilized to solve the resulting problem. A closed-form solution for computation of the proximity operator of the indicator function of the constraint set is proposed in [C2.41] when the system matrix A satisfies $AA^{*} = I$. This often happens in CS when a subset of rows is randomly selected from an orthonormal matrix such as the discrete Fourier or cosine transforms. In [C2.42], the DRS method is utilized to solve a low-rank matrix approximation optimization problem which is constrained by the CS measurement equations. The CS measurement constraints prevent over smoothness. Furthermore, nonlocal similarity patches are utilized in the optimization problem to reduce the staircase artifacts generated in the Block-based CS reconstruction.

Table 2.1 summarizes some advantages and disadvantages of the CT reconstructions algorithms.

Table 2.1 Summary of CT reconstruction algorithms

Algorithm	Main advantage	Main disadvantage
FBP [C2.1]	Accuracy	problem in working with incomplete projection data
Algebraic [C2.1]	capable to handle incomplete projection data	problem in working with inconsistent data (noisy data and modeling error)
ASD-POCS [C2.20, C2.21]	capable to handle inconsistent data (noisy data and modeling error)	path-dependent convergence
SD-BT, SD-NR, NCG-BT, NGR-NR [C2.18, C2.25]	path-independent convergence	slow to achieve convergence while working with non-smooth regularizer
TV based First Order Splitting Algorithm [C2.34, C2.29, C2.31, C2.36]	fast to achieve convergence while working with non-smooth regularizer	Suffer from undesirable staircase artifact

2.9 Synchrotron CT

2.9.1 Canadian Light Source (CLS)

The electron source in the CLS is an electron gun that emits electrons using a hot tungsten cathode with a DC anode potential of 220KV. The electron gun primarily transmits electrons to the linear accelerator. The linear accelerator moves electrons to a maximum energy of 250 MeV. The next step is a booster ring in the electron path, in the booster ring, electrons get an energy boost from 250MeV to 2.9GeV from microwaves produced by radio frequency cavities. After that, electrons at very near levels of the light speed are kept in the storage ring along a circular path consisting of vacuum chambers. In general, during linear uniform motion, electrons do not radiate, but during acceleration, their electric fields are rearranged which causes electromagnetic radiation. In the storage ring, transverse acceleration due to magnetic forces is responsible for the observed synchrotron radiation. Such magnetic forces come either from bending magnets or from special insertion device magnets like undulators and wigglers. The accelerated electrons lose their energy when they generate synchrotron radiation, so a superconducting radio frequency cavity is used to compensate for this energy loss. It maintains the electron beam to stay continuous and steady. The storage ring has openings that allow the radiation to escape and follow the radiation line into the vacuum chamber of the experimenters [C2.43].

Synchrotron CT is a recognized technique for characterizing the inner 3D structure of the samples in biological and medical applications. Synchrotron-based CT has some benefits regarding the lab-based CT. Firstly, the synchrotron monochromatic beams demonstrate temporal coherence. This allows the reconstructed images to be free of nonlinear beam hardening artifacts, which make it possible to use the linear calibration procedures [C2.44]. Secondly, the small angular divergence of synchrotron beams - spatial coherence - allows the spatial resolution of the reconstructed image to be almost determined only by the detector resolution. Thirdly, the synchrotron high brilliance beam makes it possible to implement a fast CT data acquisition process [C2.45]. Finally, the spatial coherence of the beam allows the phase-sensitive imaging techniques to be used [C2.46]. On the other hand, the advantages of lab-based CT are cost effectiveness, ease of use, large field of view and high scanning speed (scanned volume per time) [C2.47].

2.9.2 X-ray Phase Contrast Imaging

X-ray phase contrast imaging uses phase changes rather than absorption, this is particularly helpful in cases where imaging soft tissue samples [C2.48] or where the attenuation coefficient is too small between various regions in the sample [C2.49]. Phase contrast imaging can also be useful in biological and medical research because it is mainly based on x-ray refraction, not absorption so it decreases at higher energy levels less rapidly than absorption contrast imaging. As a result, higher energy can be used for phase contrast imaging where the absorbed radiation dose could be lower, thereby minimizing potential tissue damage.

Several techniques have been developed for phase contrast imaging, such as interferometric, analyzer-based and propagation-based phase contrast imaging. These three techniques, at the base physics level, measure φ, $\nabla\varphi$ and $\nabla^2\varphi$ respectively, where φ is the x-ray phase change when it passes through the sample [C2.50].

2.9.2.1 X-ray Interferometry

Three similar crystals in the parallel arrangement act like an x-ray interferometer. After collimation and filtering of incident x-ray beams by a monochromator, which usually consists of additional one or more crystals so that only the x rays of the desired energy are reflected toward the interferometer, the first interferometer crystal splits the incident beam. The middle crystal works like a mirror, reflecting the beams to each other. The third crystal, the analyzer crystal, reunifies the beams. Through taking multiple interferometric images at various rotational directions of a sample, a three-dimensional map of the sample refractive index is reconstructed. The interferometer is best suited to high-resolution scanning of small samples because it requires near perfect crystal alignment and setup stabilization [C2.50].

2.9.2.2 Analyzer-Based Imaging

In a typical Analyzer-Based Imaging (ABI) setup, synchrotron radiation coming out of a monochromator is almost parallel. The x-ray beams can be absorbed, scattered or refracted by going through a sample between the monochromator and the analyzer crystal. Refraction occurs because of the small variations in the sample refractive indices. X rays that emerge from the specimen and enter the analyzer crystal will only follow the Bragg diffraction requirement for a very narrow angle range, usually of a few μrad. X rays scattered throughout the specimen will fall outside this range and will not be reflected. However, refracted x rays are reflected within this range and the reflectivity depends on the angle of incidence. This dependency is known as the Rocking Curve. If the analyzer crystal is perfectly aligned with the monochromator, the refracted x-ray beams form an image in the x-ray detector, which is like the x-ray radiograph, but its contrast is enhanced due to scatter rejection. Alternatively, if the analyzer crystal is detuned at a small angle with respect to the monochromator then there will be less reflections on x-rays refracted by a smaller angle and more refraction on x rays refracted by a greater angle. As a result, the detected image contrast is formed based on the different refraction angles in the sample.

A detuned analyzer crystal creates an image which includes both refraction and absorption effects. However, pure refraction and apparent absorption images can be reconstructed by merging images captured on either side of the rocking curve. The pure refraction image is sensitive to the refractive index gradient and greatly enhance the edges between the regions with different refracting indices [C2.50].

2.9.2.3 Propagation-based Phase Contrast Imaging

In a typical Propagation-based Phase Contrast Imaging (PPCI) or in-line holography setup, phase-contrast images can be generated when the x-ray source provides a spatially coherent illumination. The experimental setup of this synchrotron-based technique is like the setup used in radiography i.e. synchrotron x-ray source, the sample and the detector are inline, without any optical element between the sample and the detector. Instead of placing the detector directly behind the sample, which is convenient in the conventional absorption image, it is placed in some distance from the sample which is often called propagation distance. As a result, the x-rays that are refracted by different tissues due to different refractive indices inside the sample can interfere with the unaffected beam on the detector. The phase contrast image formed in the detector is sensitive to abrupt variations of refractive indices; so, the structural boundaries between different tissues inside the sample are enhanced in this technique. With this capability, the synchrotron based PPCI can provide higher tissue contrast and spatial resolution compared with conventional x-ray CT. The optimal detector location depends on the size of features of interest and the x-ray wavelength [C2.50].

The image obtained based on PPCI includes effects of absorption as well as refraction, so it needs the phase retrieval process to extract the pure phase data. The phase retrieval process usually requires at least two intensity measurements at two distinct distances between sample and detector [C2.51, C2.52]. Taking PPCT data at two different distances increases the scanning time and exposes the specimens to a higher radiation dose that might impede its biomedical applications.

2.9.3 Synchrotron CT Reconstruction

The conventional methods of phase contrast computed tomography reconstruction can be divided into two main categories. Filtered Back Projection and Algebraic Iterative Algorithms [C2.53].

Three software programs (NRecon[1], PITRE[2] and HPITRE[3]) are commonly used for the phase contrast computed tomography reconstruction in biomedical application [C2.54]. Basically, these software programs use the FBP algorithm, but include various filters to generate the required image reconstruction. The reconstruction of the phase contrast computed tomography requires the adjustment of certain settings and criteria for a given dataset. The following parameters have been adjusted either with the above listed software programs or in combination with other software. These may include dark and flat-field calibration, phase retrieval for propagation-based phase-contrast imaging, diffraction-enhanced phase-contrast imaging information extraction, sinogram generation, sinogram pre-processing before reconstruction, and finally slice reconstruction which is based on FBP algorithm [C2.55]. The approach for phase-contrast computed tomography in this thesis is the direct propagation-based phase-contrast computed tomography without phase retrieval. In other words, in this approach one acquires a single inline phase-contrast image for each tomographic projection, and 2D tomograms (two-dimensional image representing a slice) are reconstructed from the corresponding sinogram of these projection images directly without the phase retrieval by means of a CT reconstruction algorithms including FBP, algebraic reconstruction techniques, total-variation based reconstruction methods or the proposed compressed sensing based slice reconstruction algorithms.

---

[1] Software for CT reconstruction (NRecon), SkyScan (Bruker-microCT), Kontich, Belgiuim
https://www.bruker.com/service/support-upgrades/software-downloads/micro-ct.html

[2] PITRE (Phase-sensitive x-ray Image processing and Tomography REconstruction), INFN Trieste, Trieste, Italy
http://journals.iucr.org/s/issues/2012/05/00/mo5035/
https://sites.google.com/site/rongchangchen/

[3] HPITRE (High performance Phase-sensitive x-ray Image processing and Tomography REconstruction), INFN Trieste, Trieste, Italy
http://journals.iucr.org/s/issues/2012/05/00/mo5035/
https://sites.google.com/site/rongchangchen/

References

[C2.1] A. C. Kak and M. Slaney, “Principles of Computerized Tomographic Imaging” , Society of Industrial and Applied Mathematics, 2001.

[C2.2] H. P. Hiriyannaiah, “X-ray computed tomography for medical imaging”, Signal Processing Magazine, IEEE, vol. 14, pp. 42-59, 1997.

[C2.3] W. A. Kalender, “Computed Tomography: Fundamentals, System Technology, Image Quality, Applications”, Germany: Erlangen, 2005.

[C2.4] J. Hsieh, “Computed tomography: principles, design, artifacts and recent advances”, Washington: SPIE Press, 2003.

[C2.5] T. M. Buzug, “Computed tomography: from photon statistics to modern cone-beam CT”, Springer, 2008.

[C2.6] S. Kaczmarz, “Angenaherte auflosung von systemen linearer gleichungen”, Bull. Acad. Pol. Sci. Lett. A, vol. 6-8A, pp. 355-357, 1937.

[C2.7] K. Tanabe, “Projection method for solving a singular system”, Numer. Math., vol. 17, pp. 203-214, 1971.

[C2.8] A. Cichocki, S.I. Amari, “Adaptive Blind Signal and Image Processing”, Wiley, New York, 2002.

[C2.9] G. N. Hounsfield, “A method of and apparatus for examination of a body by radiation such as x-ray or gamma radiation”, Patent Specification 1283915, The Patent Office, 1972.

[C2.10] Y. Tsaig, DL Donoho, “Compressed sensing”. IEEE Transactions on Information Theory. 52:1289–1306, 2006.

[C2.11] EJ. Candés, J. Romberg, T. Tao, “Robust uncertainty principles: exact signal reconstruction from highly incomplete frequency information”. IEEE Transactions on Information Theory, 52(2):489–509, 2006.

[C2.12] IEEE Signal Processing Magazine, Special Issue on Compressive Sampling, March 2008.

[C2.13] V. Stanković, L Stanković, and S. Cheng, “Compressive image sampling with side information, Image Processing (ICIP)”, 16th IEEE International Conference on. IEEE, 2009.

[C2.14] DL Donoho, I. Drori, Y. Tsaig, and JL Starck. “Sparse solution of underdetermined linear equations by stagewise orthogonal matching pursuit”. Department of Statistics, Stanford University, 2006.

[C2.15] M. Li, H. Yang, and H. Kudo. “An accurate iterative reconstruction algorithm for sparse objects: application to 3D blood vessel reconstruction from a limited number of projections” , Physics in medicine and biology 47.15: 2599 (2002).projections”,

[C2.16] M. Li, H. Kudo, J. Hu & R.H. Johnson, “Improved iterative algorithm for sparse object reconstruction and its performance evaluation with micro-CT data”, Nuclear Science, IEEE Transactions on, 51(3), 659-666, 2004.

[C2.17] G.H. Chen, J. Tang, & S. Leng, “Prior image constrained compressed sensing (PICCS): a method to accurately reconstruct dynamic CT images from highly undersampled projection data sets”, Medical physics, 35(2), 660-663, 2008.

[C2.18] P.T. Lauzier, J. Tang & G. H. Chen, “Prior image constrained compressed sensing: Implementation and performance evaluation”, Medical physics, 39(1), 66-80, 2012.

[C2.19] H. Dang, A. S. Wang, M. S. Sussman, J. H. Siewerdsen, & J. W. Stayman, “dPIRPLE: a joint estimation framework for deformable registration and penalized-likelihood CT image reconstruction using prior images”. Physics in medicine and biology, 59(17), 4799, 2014.

[C2.20] E. Y. Sidky and X. Pan, “Image reconstruction in circular cone-beam computed tomography by constrained, total-variation minimization”, Phys. Med. Biol. 53, 4777-4807, 2008.

[C2.21] E.Y. Sidky, C. M. Kao, & X. Pan. “Accurate image reconstruction from few-views and limited-angle data in divergent-beam CT”. Journal of X-ray Science and Technology, 14(2), 119-139, 2006.

[C2.22] J. Bian, J. H. Siewerdsen, X. Han, E.Y. Sidky, J. L. Prince, C. A. Pelizzari, & X. Pan. “Evaluation of sparse-view reconstruction from flat-panel-detector cone beam CT”, Physics in medicine and biology, 55(22), 6575, 2010.

[C2.23] X. Han, J. Bian, D. R. Eaker, T. L. Kline, E. Y. Sidky, E. L. Ritman, & X. Pan. "Algorithm-enabled low-dose micro-CT imaging", Medical Imaging, IEEE Transactions on, 30(3), 606-620, 2011.

[C2.24] S. Ramani and J. A. Fessler, "Parallel MR image reconstruction using augmented Lagrangian methods", IEEE Trans. Med. Imag., vol. 30, no. 3, pp. 694–706, Mar. 2011.

[C2.25] S. Ramani and J. A. Fessler, "An accelerated iterative reweighted least squares algorithm for compressed sensing MRI", in Proc. IEEE Int. Symp. Biomed. Imag, pp. 257–260, 2010.

[C2.26] A. Beck and M. Teboulle, "A fast iterative shrinkage-thresholding algorithm for linear inverse problems", SIAM J. Imag. Sci., vol. 2, no. 1, pp. 183–202, 2009.

[C2.27] A. Beck and M. Teboulle, "Fast gradient-based algorithms for constrained total variation image denoising and deblurring problems", IEEE Trans. Image Process., vol. 18, no. 11, pp. 2419–2434, Nov. 2009.

[C2.28] T. Goldstein and S. Osher, "The split Bregman method for L1-regularized problems", SIAM J. Imag. Sci., vol. 2, no. 2, pp. 323–343, 2009.

[C2.29] S. Ramani, & J. A. Fessler, "A splitting-based iterative algorithm for accelerated statistical X-ray CT reconstruction". Medical Imaging, IEEE Transactions on, 31(3), 677-688, 2012.

[C2.30] A. Chambolle, & T. Pock, "A first-order primal-dual algorithm for convex problems with applications to imaging". Journal of Mathematical Imaging and Vision, 40(1), 120-145, 2011.

[C2.31] E. Y. Sidky, H. J. Jakob & X. Pan, "Convex optimization problem prototyping for image reconstruction in computed tomography with the Chambolle-Pock algorithm". Physics in medicine and biology, 57(10), 3065, 2012.

[C2.32] E. Esser, X. Zhang & T. F. Chan, "A general framework for a class of first order primal-dual algorithms for convex optimization in imaging science". SIAM Journal on Imaging Sciences, 3(4), 1015-1046, 2010.

[C2.33] M. V. Afonso, J. M. Bioucas-Dias, and M. AT Figueiredo. "Fast image recovery using variable splitting and constrained optimization". Image Processing, IEEE Transactions on 19.9: 2345-2356, 2010.

[C2.34] B. Vandeghinste, B. Goossens, J. D. Beenhouwer, A. Pizurica, W. Philips, S. Vandenberghe, and S. Staelens, “Split-Bregman-based sparse-view CT reconstruction”, in Proc. Int. Meeting Fully 3-D Image Recon. Rad. Nucl. Med, pp. 431–434, 2011.

[C2.35] L. Ritschl, F. Bergner, C. Fleischmann, & M. Kachelrieß. “Improved total variation-based CT image reconstruction applied to clinical data”. Physics in medicine and biology, 56(6), 1545, 2011.

[C2.36] J. Song, Q. H. Liu, G. A. Johnson, & C. T. Badea. “Sparseness prior based iterative image reconstruction for retrospectively gated cardiac micro-CT”. Medical physics, 34(11), 4476-4483, 2007.

[C2.37] J. Douglas and HH Rachford, “On the numerical solution of heat conduction problems in two or three space variables”, Trans. Amer. Math. Soc; 82:421–439, 1956.

[C2.38] J. Eckstein and D. Bertsekas, “On the Douglas Rachford splitting method and the proximal point algorithm for maximal monotone operators”, Mathematical Programming, vol. 5, pp. 293-318, 1992.

[C2.39] S. Boyd, N. Parikh, E. Chu, B. Peleato, & J. Eckstein. “Distributed optimization and statistical learning via the alternating direction method of multipliers”. Foundations and Trends® in Machine Learning, 3(1), 1-122, 2011.

[C2.40] N. Parikh, & S. P. Boyd. “Proximal Algorithms. Foundations and Trends in optimization”, 1(3), 127-239, 2014.

[C2.41] Y. Yu, J. Peng, X. Han, and A. Cui, ‘‘A primal Douglas–Rachford splitting method for the constrained minimization problem in compressive sensing’’ Circuits, Syst. Signal Process., vol. 36, no. 10, pp. 4022–4049, 2017.

[C2.42] S. Li and H. Qi, “A douglas–Rachford splitting approach to compressed sensing image recovery using low-rank regularization,” IEEE Trans. Image Process., vol. 24, no. 11, pp. 4240–4249, Nov. 2015.

[C2.43] P. Grochulski. “Introduction to Canadian Light Source”. The Polish Institute of Arts and Sciences in Canada and the Polish Library, Bulletin, 22, 31-37, 2005.

[C2.44] R. C. Chen, R. Longo, L. Rigon, F. Zanconati, A. De Pellegrin, F. Arfelli, D. Dreossi, R. H. Menk, E. Vallazza, T. Q. Xiao, and E. Castelli, “Measurement of the linear attenuation coefficients of breast tissues by synchrotron radiation computed tomography”, Phys. Med. Biol. 55(17), 4993–5005, 2010.

[C2.45] J. L. Fife, M. Rappaz, M. Pistone, T. Celcer, G. Mikuljan, & M. Stampanoni, “Development of a laser-based heating system for in situ synchrotron-based X-ray tomographic microscopy”. J. Synchroton Rad. 19, 352–358, 2012.

[C2.46] P. Cloetens, R. Barrett, J. Baruchel, J. P. Guigay & M. Schlenker, “Phase objects in synchrotron radiation hard x-ray imaging”. J. Phys. D 29, 133–146, 1996.

[C2.47] O. Brunke, K. Brockdorf, S. Drews, B. Müller, T. Donath, J. Herzen, F. Beckmann, Comparison between x-ray tube based and synchrotron radiation based µct, Proceedings of SPIE 7078, 12, 2008.

[C2.48] A. Snigirev, I. Snigireva, V. Kohn, S. Kuznetsov, & I. Schelokov, “On the possibilities of x-ray phase contrast microimaging by coherent high-energy synchrotron radiation”. Rev. Sci. Instrum. 66, 5486–5492, 1995.

[C2.49] P. Cloetens, M. Pateyron-Salome´, J. Y. Buffie`re, G. Peix, J. Baruchel, F. Peyrin & M. Schlenker. “Observation of microstructure and damage in materials by phase sensitive radiography and tomography”. Journal of Applied Physics, 81, 5878-5886, 1997.

[C2.50] R. Fitzgerald, “Phase-sensitive x-ray imaging”. Physics Today; 53:23–26, 2000.

[C2.51] P. Cloetens, W. Ludwig, J. Baruchel, D. Van Dyck, J. Van Landuyt, J. P. Guigay, and M. Schlenker, “Holotomography: Quantitative phase tomography with micrometer resolution using hard synchrotron radiation x rays”, Appl. Phys. Lett. 75, 2912 – 2914, 1999.

[C2.52] S. A. Zhou, A. Brahme, “Development of phase-contrast X-ray imaging techniques and potential medical applications”, Phys Med. 24, 129 –148, 2008.

[C2.53] L. A. Flores, V. Vidal, P. Mayo, F. Rodenas, G. Verdu, “CT Image Reconstruction Based on GPUs”, Procedia Computer Science, 18: 1412–1420, 2013.

[C2.54] B. Wolkowski, E. Snead, M. Wesolowski, J. Singh, M. Pettitt, R. Chibbar, S. A. Melli, and J. Montgomery, “Assessment of freeware programs for the reconstruction of tomography datasets obtained with a monochromatic synchrotron-based X-ray source”, J. Synchrotron Radiat. 22(4), 1130–1138, 2015.

[C2.55] C. Rong-Chang, D. Dreossi, L. Mancini, R. Menk, L. Rigon, T. Q. Xiao, and R. Longo. “PITRE: software for phase-sensitive X-ray image processing and tomography reconstruction” Journal of Synchrotron Radiation 19.5, 2012.

3. Compressed Sensing based Reduced-view Image Reconstruction from Simulated Synchrotron CT Data

Published as: Melli, Seyed Ali, Khan A. Wahid, Paul Babyn, James Montgomery, Elisabeth Snead, Ali El-Gayed, Murray Pettitt, Bailey Wolkowski, and Michal Wesolowski. "A compressed sensing based reconstruction algorithm for synchrotron source propagation-based X-ray phase contrast computed tomography." Nuclear Instruments and Methods in Physics Research Section A: Accelerators, Spectrometers, Detectors and Associated Equipment 806 (2016): 307-317.

In the previous chapter, analytical and algebraic reconstruction methods which are often used in the commercial CT scanners are discussed. These methods have acceptable performance when there are a large number of closely sampled projections over the scanning angular range, otherwise, artifacts will occur in the reconstructed image. Therefore, compressed sensing-based algorithm such as ASD-POCS, PICCS and Split-Bregman-type (SB) schemes are discussed to recover images from highly undersampled data.

The manuscript included in this chapter proposes a compressed sensing based reduced-view image reconstruction algorithm to reconstruct the tomographic image from simulated synchrotron CT data. The goal is to suppress the aliasing artifacts that appear in the image because of the reduction of the number of projections. Poor conditioning of reduced-view synchrotron CT projection matrix and the processing of large synchrotron CT data are numerical challenges which are addressed in this study. Total variation regularization and a combination of Douglas-Rachford Splitting and randomized Kaczmarz methods are used to solve these numerical issues. Visual and quantitative performance evaluations of a reconstructed abdomen phantom and a reconstructed slice of a canine prostate tissue demonstrate the effectiveness of the proposed algorithm compared to other existing algorithms.

The student (first author) designed the algorithm, processed the raw data, performed the numerical simulation, interpreted the results, designed the figures and wrote the manuscript, K. A. Wahid and, P. Babyn provided equal supervision effort. Other authors were involved in collection of synchrotron data at the Canadian Light Source, including the methods used to collect the data and the technical analyses supporting the quality of the measurements.

A compressed sensing-based reconstruction algorithm for synchrotron source propagation-based X-ray phase contrast computed tomography

Ali Melli, Khan A. Wahid, Paul Babyn, James Montgomery, Elisabeth Snead, Ali El-Gayed,

Murray Pettitt, Bailey Wolkowski, Michal Wesolowski

Abstract

Synchrotron source propagation-based X-ray phase contrast computed tomography is increasingly used in pre-clinical imaging. However, it typically requires a large number of projections, and subsequently a large radiation dose, to produce high quality images. To improve the applicability of this imaging technique, reconstruction algorithms that can reduce the radiation dose and acquisition time without degrading image quality are needed. The proposed research focused on using a novel combination of Douglas-Rachford Splitting and randomized Kaczmarz algorithms to solve large-scale total variation based optimization in a compressed sensing framework to reconstruct 2D images from a reduced number of projections. Visual assessment and quantitative performance evaluations of a synthetic abdomen phantom and real reconstructed image of an *ex-vivo* slice of canine prostate tissue demonstrate that the proposed algorithm is competitive in reconstruction process compared with other well-known algorithms. An additional potential benefit of reducing the number of projections would be reduction of time for motion artifact to occur if the sample moves during image acquisition. Use of this reconstruction algorithm to reduce the required number of projections in synchrotron source propagation-based X-ray phase contrast computed tomography is an effective form of dose reduction that may pave the way for imaging of *in-vivo* samples.

Index terms

synchrotron source imaging; propagation-based X-ray phase contrast computed tomography; compressed sensing; low X-ray dose computed tomography reconstruction algorithm.

3.1 Introduction

One limitation of conventional x-ray Computed Tomography (CT) is that the tissue attenuations of soft tissue structures are similar in hard x-rays and these tissues cannot be examined without using iodine. For example, conventional x-ray CT cannot discriminate minor differences in tissue density/variation which occurs in the early stages of prostate cancer [C3.1]. To address this issue, X-ray Phase Contrast Computed Tomography (XPC-CT) [C3.2, C3.3] has been utilizing the change in phase of x-ray beams as they pass through a sample rather than solely relying on the amplitude attenuation, as is the case with conventional x-ray CT. The phase sensitivity to mild density variation in the soft tissues is three orders of magnitude higher than the amplitude sensitivity at 10-100 keV range [C3.4]. Therefore, XPC-CT has an improved ability to differentiate amongst different soft tissue structures without need for exogenous contrast.

There are several experimental setups available to generate x-ray phase contrast images. Among them, propagation-based XPC-CT (also known as "in-line holography") has a simple setup with high spatial resolution (a few tens of microns) and low dose capability. Some encouraging results have been reported for the application of this technique in clinical experiments [C3.5]. Phase-contrast images can be generated with this technique when the x-ray source provides a spatially coherent illumination [C3.6]. Propagation-based XPC-CT techniques have been developed with synchrotrons sources as they provide spatially coherent high brilliance radiation [C3.7, C3.8]. The experimental setup of this synchrotron-based technique is like the setup used in radiography i.e. synchrotron x-ray source, the sample and the detector are inline, without any optical element between the sample and the detector. Instead of placing the detector directly behind the sample, which is convenient in radiography, it is placed in some distance from the sample (often called propagation distance). As a result, the x-rays that are refracted by different tissues due to different refractive indices inside the sample can interfere with unaffected beam on the detector [C3.9]. The phase contrast image formed in the detector is sensitive to abrupt variations of refractive indices; so the structural boundaries between different tissues inside the sample are enhanced in this technique [C3.10].

With this capability, the synchrotron-based propagation-based XPC-CT can provide higher tissue contrast and spatial resolution of prostate images compared with conventional x-ray CT [C3.11]. To achieve the requisite spatial resolution, a large number of projection views (>1000) is necessary to discriminate fine details of small structures in the sample field of view [C3.12, C3.13, C3.14]. This exposes the specimen to high radiation that would be detrimental when imaging a live patient or animal in-vivo. One approach to decrease total x-ray dose and imaging time is to reduce exposure time per projection which is the only parameter that can be used to control the amount of x-ray dose in each projection since the photon brightness of synchrotron x-ray is fixed [C3.15]. However, the minimum exposure time is limited by detector sensitivity and readout speed. Also, low exposure time generally results in lower projection signal to noise and accordingly lower quality of reconstructed image [C3.16]. Sparse-view imaging technique is another approach which can reduce the number of projections and consequently the total x-ray dose and imaging time, while maintaining acceptable diagnostic image quality.

Analytical algorithms such as Filtered Back Projection (FBP) remain the standard reconstruction algorithm for most commercial CT scanners. When sparse-view imaging technique is used with this algorithm, serious aliasing artifacts, such as sharp streaks, can be observed in the reconstructed images [C3.17]. Unlike analytical algorithms, iterative algorithms are increasingly used for reconstruction of images when noisy and incomplete projection data are available [C3.18]. Iterative algorithms are based on solving a system of linear equations subject to the constraints that are obtained from prior information about the reconstructed image. A number of well-known iterative algorithms include: Projection onto Convex Sets (POCS) [C3.19], Maximum Likelihood Expectation Maximization (MLEM) [C3.20] and Adaptive Steepest Descent - Projection onto Convex Sets (ASD–POCS) [C3.21]. POCS, also known as the alternating projection algorithm, has relatively low computational complexity and is utilized to find the intersection point of two or more closed convex sets to solve a system of linear equations. The MLEM algorithm attempts to solve a system of linear equations which have non-negative coefficients in both the system matrix and observation vector. The ASD–POCS algorithm attempts to reconstruct the assumed non-negative images by minimizing the total variation semi-norm in the image, subject to the constraint that the estimated projected data should be within a known tolerance of the acquired data.

Recently, Compressed Sensing (CS) theory has attracted huge attention in the imaging community because of its ability to formulate the principles for exact recovery of signal from highly incomplete frequency information [C3.22, C3.23]. This theory is applicable to images that are compressible in a predefined basis/frame such as wavelet, gradient, Fourier i.e. most of the transformed image pixels should be approximately zero. Use of the gradient basis such as Total Variation (TV) has proven advantageous for tomographic images as they have uniform tissues with only abrupt changes at boundaries [C3.24]. It motivates us to propose a CS-based algorithm to reconstruct large-scale high-resolution images from significantly reduced projection data.

The algorithm proposed in this paper aims to recover the image from sparse-view synchrotron source propagation-based phase contrast data using a combination of Douglas-Rachford Splitting (DRS) and randomized Kaczmarz algorithms to optimize large-scale TV-based optimization in a compressed sensing framework. The DRS algorithm was first formulated in [C3.25] and is applicable to convex programming in which a large problem can be divided into smaller and easier to solve problems. The randomized Kaczmarz algorithm is an iterative algorithm that can be used to solve linear equations. One application of this algorithm in solving linear equations is illustrated by reconstruction of a band-limited function from non-uniform spaced sampling values in [C3.26]. We hypothesize that the proposed algorithm can reconstruct smooth image regions while preserving prominent edges at the borders of different regions better than existing reconstruction algorithms.

Our proposed algorithm may also be applicable to other synchrotron-based medical imaging technologies including micro Computed Tomography (micro-CT) [C3.27], K-Edge Subtraction Computed Tomography (KES-CT) [C3.28] and Diffraction Enhanced Imaging Computed Tomography (DEI-CT) [C3.29] to reduce radiation dose and imaging time.

3.2 Material and Methods

3.2.1 XPC-CT data acquisition

Phase contrast projection data were collected at the Biomedical Imaging and Therapy Bending Magnet (BMIT-BM) Beamline at the Canadian Light Source, Inc. (CLS) [C3.15]. This is a bend magnet beamline with a field strength of 1.354 T. The ring energy is 2.9 GeV and the storage ring current is a maximum of 250 mA operating in decay mode. The critical energy of the bend magnet source is 7.57 keV. The Beamline uses a Si (2,2,0) Bragg double crystal monochromator at a distance of 13.2 m from the source. A formalin fixed canine prostate was suspended in a plastic specimen tube within Knox Gelatin[4]. The sample was placed on a rotating mechanical stage that was 25m away from the synchrotron source so that the x-ray beam can be assumed to be parallel. The x-ray beam energy was 30 keV. A Photonic Science VHR-90 radiation detector[5] (FOP coupled CCD detector, 18.67 µm x 18.67 µm pixel size) was placed 5m behind the sample to allow propagation phase contrast imaging. The sample was then rotated over 180.096˚ and 3,751 projections were taken, each at a rotational step size of 0.048˚. Dark and flat calibration images were taken before and after the tomogram projections for each 3.1 mm thick slice of the prostate gland under scan. The detector processed these projections in a 12-bit TIFF greyscale digital format.

Synchrotron source propagation-based XPC-CT raw data requires preprocessing prior to reconstruction, including dark and flat field calibration, rotation center alignment and ring artifact correction. These modifications should be done before application of the reconstruction algorithm [C3.30]. NRecon developed in Bruker microCT[6] [C3.31] and PITRE (Phase-sensitive X-ray Image processing and Tomography REconstruction) [C3.32] are two commercial software systems used at the Canadian Light Source to preprocess raw data and reconstruct tomographic images. PITRE offers parallel-beam tomographic reconstruction for phase contrast CT data. In this program, dark and flat field calibration is performed on the projections. After sinogram generation, PITRE implements image cutting, extended field of view CT data conversion, ring artifacts correction and rotation center alignment. On the other hand, NRecon is a general-purpose and easy to use software. It does not support some preprocessing tasks which are required for preparation of synchrotron CT raw data for reconstruction; for example, the software does not implement dark and flat field calibration. Consequently, a macro plugin for ImageJ [C3.33] is used for dark and flat field calibration. After opening calibrated raw data in NRecon, it will automatically find the best settings for rotation center alignment, ring artifact correction and smoothing filter. NRecon needs a large number of angular projections to generate the reference image and the corresponding sinogram dataset for performance evaluation of different algorithms.

---

[4] Knox Gelatin, Associated Brands LP, Toronto, ON

[5] Photonic Science VHR90, Photonic Science, Ltd., Millham, Mountfield, UK

[6] Bruker microCT, Kontich, Belgium

3.2.2 Sparse View Imaging

It is possible to reconstruct a significant (high signal to noise) 3D object from non-significant (low signal to noise) 2D projections, if the number of projections is large [C3.34]. In practice, the upper limit to the number of projections over which the dose can be fractionated is given by the requirement that the 2D projections have to be aligned to a common origin before a 3D reconstruction can be computed [C3.35]. After some trial and error, we have concluded that shortening the exposure time per projection to less than 100 milliseconds would lead to significant decrease in projection signal to noise so the requirement that the 2D projections must be aligned to a common origin may be violated. Each prostate requires between 6 and 12 slices to image the whole gland with each slice consisting of nearly 4000 projections as per Nyquist-Shannon sampling theory to guarantee appropriate reconstruction [C3.14, C3.36]. As a result, high total radiation exposure is inevitable which is harmful to live bodies. Besides, an average acquisition time of 60 minutes to image the whole gland tends to be too long for live bodies because motion artifact may occur if the sample moves during image acquisition. The compressed sensing theory intends to reconstruct images with a good accuracy from considerably fewer projections than required by the Nyquist-Shannon theory [C3.37]. The proposed compressed sensing-based method reduces the number of projections to proportionally decrease radiation dose as well as acquisition time while maintaining acceptable diagnostic contrast and spatial resolution in the reconstructed image.

3.2.3 Imaging model and optimization formulation

In the XPC-CT experiment, the collected noisy data $b = (b_1, b_2, \dots, b_M)^T$and the reconstructed image $x = (x_1, x_2, \dots, x_N)^T$, where T is the transpose of a vector, can be inferred as a discrete linear system:

$$b = Ax + n \tag{3.1}$$

Where, A represents an underdetermined $M \times N$ $(M < N)$ system matrix that models a parallel x-ray beam forward projection and n represents zero mean additive white Gaussian noise model. The objective is to accurately reconstruct an image from incomplete noisy data. When $M < N$, a unique solution of Eq. (3.1) does not exist leading to an infinite number of solutions. To solve this problem, regularization should be applied which outlines a weak smoothness constraint for selecting a solution from a set of infinite solutions. In other words, the regularization controls the trade-off between fidelity to measured data and to prior information (smoothness of computed tomography images), so the regularized energy function to be minimized is a weighted sum of two functions as shown below in Eq. (3.2):

$$J(x,\alpha) = \frac{1}{2}\|Ax-b\|_2^2 + \alpha J(x) \quad \text{With} \quad \alpha > 0 \tag{3.2}$$

Where the first term is the data fidelity function and the second term is the regularizing function. One well known regularizing function is Tikhonov function [C3.38] where the J(x) is the squared L2-norm (the square root of the sum of the squared pixel values, i.e. ${\|x\|_2}^2 = {x_1}^2 + {x_2}^2 + \cdots + {x_n}^2$ of an image. However, Tikhonov function tends to make images excessively smooth and poorly preserves important image characteristics, such as sharp edges. As a result, L1-norm (the sum of the absolute pixel values, i.e.$\|x\|_1 = |x_1| + |x_2| + \cdots + |x_n|$ of the gradient image also known as total variation (TV) function [C3.39] is commonly used as the regularizing function for image reconstruction [C3.40]. The benefit of TV regularization over Tikhonov quadratic regularization is that it makes the recovered image sharper by accurately preserving the edges especially in piecewise smooth images and the solution is insensitive to some data values that are far away from others [C3.41].

According to the above description, let us consider a TV-based optimization problem called generalized Lasso [C3.42]:

$$\text{Minimize} \quad \frac{1}{2}\|Ax-b\|_2^2 + \lambda\|Fx\|_1 \tag{3.3}$$

Here, parameter λ compromises between data fidelity and regularizing function. Let $x_{i,j}$ denote the pixel in the ith row and jth column of an $n \times n$ image x and define the difference operators as follows:

$$FH_{ij}x = \begin{cases} x_{i+1,j} - x_{i,j} : i < n \\ 0 \quad : i = n \end{cases} \qquad Fv_{ij}x = \begin{cases} x_{i,j+1} - x_{i,j} : j < n \\ 0 \quad : j = n \end{cases} \qquad F_{ij}x = \begin{pmatrix} FH_{ij}x \\ Fv_{ij}x \end{pmatrix} \tag{3.4}$$

Where, $FH_{ij}x$ and $Fv_{ij}x$ are horizontal and vertical difference operators respectively. With this definition, the second term in Eq. (3.3) is called TV operator. The difficulties that arise in solving this optimization problem are related to non-differentiability of L1-norm $\|Fx\|_1$at zero which leads to numerical instabilities for common gradient-based optimization algorithms. Some are related to noisy data and ill-conditioning of the system matrix which causes the solution of optimization problem deviate strongly from noise-free solution. Lastly, optimization in large-scale makes some methods which use second order primal-dual interior-point inefficient and impractical.

3.2.4 Proposed algorithm

Our approach to solve the problem is to modify Eq. (3.3) into an equivalent constrained optimization problem as shown in Eq. (3.5) below:

$$\underset{x}{Minimize}\ \ \frac{1}{2}\|Ax-b\|_2^2+\lambda\|z\|_1 \text{ subject to } Fx-z=0 \tag{3.5}$$

In order to find a global minimum of a function subject to equality constraint, an unconstrained optimization problem should be formed as follows:

$$\underset{x,z,y}{Minimize}\ \ L_\rho(x,z,y)=\frac{1}{2}\|Ax-b\|_2^2+\lambda\|z\|_1+y^T(Fx-z)+\frac{\rho}{2}\|Fx-z\|_2^2 \tag{3.6}$$

Where, $y^T$is called the vector of dual variables and $\rho>0$ is called the penalty parameter [C3.43, C3.47]. The benefit of including the penalty term $\frac{\rho}{2}\|Fx-z\|_2^2$ is to ensure global convergence which means better handling of ill-conditioned measurement. The measurement equation $b=Ax$ is ill-conditioned because small changes in b or even A may lead to large changes in solution vector x. Defining the residual $r=Fx-z$ and using Eq. (3.7) that is a simple mathematic formula, Eq. (3.6) can be rewritten in a new form that is illustrated in Eq. (3.8) by merging the linear function $y^T(Fx-z)$ and quadratic function $\frac{\rho}{2}\|Fx-z\|_2^2$, and scaling the dual variables.

$$y^Tr+\frac{\rho}{2}\|r\|_2^2=\frac{\rho}{2}(\|r+u\|_2^2-\|u\|_2^2)\qquad u=\frac{y}{\rho} \tag{3.7}$$

$$\underset{x,z,u}{Minimize}\ \ L_\rho(x,z,y)=\frac{1}{2}\|Ax-b\|_2^2+\lambda\|z\|_1+\frac{\rho}{2}\|Fx-z+u\|_2^2-\frac{\rho}{2}\|u\|_2^2 \tag{3.8}$$

We propose to solve the minimization problem in Eq. (3.8) by applying Douglas-Rachford Splitting (DRS) algorithm [C3.44]. Using this algorithm, Eq. (3.8) will be decomposed into sub optimization problems by separately minimizing it with respect to x and z while assuming the other variable to be fixed. This method is most useful when the optimization problem with respect to x and z (i.e. Eq. (3.9) and Eq. (3.10)) can be efficiently evaluated whereas the joint minimization of Eq. (3.8) is not easy to evaluate. This minimizing process is completed by a dual variable update operation. The sub optimization steps are given below:

Loop

$$x^{k+1} = \underset{x}{Minimize}\ \frac{1}{2}\|Ax - b\|_2^2 + \frac{\rho}{2}\|Fx - z^k + u^k\|_2^2 \tag{3.9}$$

$$z^{k+1} = \underset{z}{Minimize}\ \lambda\|z\|_1 + \frac{\rho}{2}\|Fx^{k+1} - z + u^k\|_2^2 \tag{3.10}$$

$$u^{k+1} = u^k + Fx^{k+1} - z^{k+1} \tag{3.11}$$

Until stop condition is satisfied

Where, k is a loop counter. In each of the x and z -update steps, $L_\rho(x, z, y)$ is minimized over the corresponding variable, using the most recent value of the other variables x, z and u. The fixed terms such as $\frac{\rho}{2}\|u\|_2^2$ that are ineffective in finding the optimal solution are removed from sub optimization update steps. Structures in Eq. (3.9) and Eq. (3.10) can be utilized to find closed form solution or an iterative formulation to update x and z efficiently.

Although $\lambda\|z\|_1$ in Eq. (3.10) is not differentiable, sub differential calculus techniques [C3.45, C3.47] can be used to compute a closed form formula. The solution is an element-wise soft threshold formula as given below:

$$z^{k+1} = S_{\frac{\lambda}{\rho}}(Fx^{k+1} + u^k) \tag{3.12}$$

Where, operator S is defined as follows:

$$S_\kappa(a) = \begin{cases} a - \kappa & a > \kappa \\ 0 & |a| \leq k \\ a + \kappa & a < -k \end{cases} \tag{3.13}$$

This formula shrinks the vector elements toward zero without making any discontinuity. The next step is to find a closed form formula to solve optimization problem in Eq. (3.9). This is a least square minimization problem and the solution is as follows [C3.46]:

$$x^{k+1} = (A^TA + \rho F^TF)^{-1}(A^Tb + \rho F^T(z^k - u^k)) \tag{3.14}$$

According to Eq. (3.14), a system of linear equations with the coefficient matrix $A^TA + \rho F^TF$ and right hand matrix $A^Tb + \rho F^T(z^k - u^k)$ should be solved to update x.

Here, we propose to use the randomized Kaczmarz iterative algorithm for solving large-scale linear systems. The algorithm converges to the accurate answer without a need to inverse the coefficient matrix. The randomized Kaczmarz algorithm is as follows [C3.26]:

Algorithm (Randomized Kaczmarz algorithm): Assume $Ax = b$, $A \in R^{M\times N}$ to be a system of linear equations and x_0 be the first approximation of the final solution. We represent the rows of A by $a_1, a_2, \dots, a_M$ and let $b = (b_1, b_2, \dots, b_M)^T$. The iterative formula to compute the final solution is as follows:

$$x^{k+1} = x^k + \frac{b_{r(i)} - \langle a_{r(i)}, x_k\rangle}{\|a_{r(i)}\|_2^2} \tag{3.15}$$

Where, $r(i)$ is randomly selected with probability proportional to $\|a_{r(i)}\|_2^2$ from the number set {1, 2 . . . M}.

The proposed algorithm is summarized below:

Initialize: A, b, F and $\rho, \lambda > 0$

Loop

Compute x^{k+1} using Eq. (3.14) with $z = z^k$, $u = u^k$ - randomized Kaczmarz

Compute z^{k+1} using Eq. (3.12) with $x = x^{k+1}$, $u = u^k$ - soft threshold

Compute u^{k+1} using Eq. (3.11) with $z = z^{k+1}$, $x = x^{k+1}$ and $k = k + 1$

Until $\frac{\|x^{k+1} - x^k\|_2}{Max\{\|x^k\|_2, 1\}} < \varepsilon$ (tolerance ε, e.g. 10^{-4})

We can now “warm start” each iteration in randomized Kaczmarz algorithm by initializing each iteration with solution x_k which is obtained in the previous DRS iteration. See [C3.47] for further explanation. Therefore, the number of x-update iterations in randomized Kaczmarz algorithm (inner iterations) reduces to a small number while the global DRS algorithm (outer iterations) converges. This can provide considerable time savings.

The proposed algorithm was implemented using MATLAB R2014b. Element-wise soft threshold formula in Eq. (3.12) was implemented by “wthresh” command in the MATLAB environment. Randomized Kaczmarz algorithm in Eq. (3.14) was implemented by “randkaczmarz” command which is included in the “AIR Tools” package in MATLAB [C3.48].

3.2.5 Assessment of image quality

Both visual and quantitative evaluations are used to compare the performance of the proposed algorithm with other related algorithms. They are described in the next section.

3.2.5.1 Quantitative based assessment

Three quantitative metrics, Structural SIMilarity (SSIM) index, Peak Signal to Noise Ratio (PSNR), and Relative Error (RE) are used to evaluate the quality of reconstructed images. The SSIM is a degradation-based quality metric for measuring the structural similarity between two images and it has been proven to be consistent with human visual system [C3.49]. If ρ and t are two local image windows selected from the same position of two input images, SSIM can be calculated as:

$$SSIM(\rho, t) = \frac{2\mu_\rho\mu_t + C1}{\mu_\rho^2 + \mu_t^2 + C1} . \frac{2\sigma_\rho\sigma_t + C2}{\sigma_\rho^2 + \sigma_t^2 + C2} . \frac{\sigma_{\rho t} + C3}{\sigma_\rho\sigma_t + C3} \tag{3.16}$$

Where, μ_ρ and μ_t are the averages, σ_ρ and σ_t are the standard deviations and $\sigma_{\rho t}$ is the covariance of the local windows. $2C3 = C2$, $C1$ are constants to stabilize division. The overall SSIM index is calculated by averaging the SSIM map along the entire image. A higher SSIM index indicates superior image quality.

The PSNR is an error sensitive quality metric used to estimate reconstruction accuracy and is defined as follows:

$$PSNR(db) = 10\, log_{10}\left(\frac{Peak^2}{MSE}\right) \tag{3.17}$$

Where, Peak is the highest pixel value, e.g. in the case of 12-bit pixel representation, it is 1023; MSE is the mean square error between the reconstructed and reference images.

Lastly, Relative error between a reconstructed and reference image is defined as follows:

$$RE(\%) = \frac{\left\|x_{ref} - x_{rec}\right\|_2}{\left\|x_{ref}\right\|_2} \times 100 \tag{3.18}$$

3.2.5.2 Visual Assessment

The images were reconstructed by five different algorithms at four different sampling rates of projected data. In addition to comparison of these reconstructed images, enlarged regions of interest from these images were also compared with the corresponding region of interest from reference image to visually assess the reconstruction process.

3.3 Experimental Results and Discussion

The proposed algorithm along with four existing methods were used to reconstruct a synthetic abdomen phantom image and a 3.1 mm thick single transverse slice of a canine prostate. In both cases, the reconstruction algorithms were implemented at different number of projected data that are uniformly extracted from a full dataset. MATLAB R2014b software was used to implement the algorithms on a Desktop PC with Intel® Xeon® CPU 2GHz processor and 32GB memory.

3.3.1 Reconstructed images of synthetic abdomen phantom

A noise-free synthetic abdomen phantom [C3.50] is used as the first experiment because it covers large and small structures. The size of this phantom image is 512×512 pixels. Five images were reconstructed using FBP, POCS, MLEM, ASD-POCS and the proposed algorithm where equally spaced 7%, 10%, 20% and 40% of the full dataset have been used. Fig. 3.1 shows the reference image compared with reconstructed images using 20% (72 views) of the full dataset. As it is evident from Fig. 3.1, the proposed algorithm is able to perfectly reconstruct the phantom image using only 20% of projected data. Fig. 3.2 shows structure similarity index maps for four algorithms so that a pixel-by-pixel comparison can be performed. The SSIM map was not shown for the proposed algorithm because the reconstruction is almost perfect for this algorithm. The enlarged image areas are shown in Fig. 3.3 to better illustrate the quality of the reconstructed images. As shown in Figs. 3.1, 3.2 and 3.3, FBP reconstructs detailed (high spatial frequency) features such as edges better than POCS and MLEM; however, the POCS and MLEM algorithms can better recover smooth (low spatial frequency) regions and suppress streak artifacts generated by incomplete projected data relative to images reconstructed with FBP. Also, ASD-POCS and the proposed algorithm can recover prominent edges and simultaneously reduce or completely remove streak artifacts which means that these two algorithms are more successful in forming artifact-resolution trade-off than FBP, POCS and MLEM algorithms.

Table 3.1 shows the quality metrics for different number of projected data. To better illustrate the effectiveness of the proposed algorithm, the quality metrics are plotted and shown individually in Fig. 3.4. It can be seen from Table 3.1 and Fig. 3.4 that the proposed algorithm has lower reconstruction error and higher structural similarity to the reference image compared with other algorithms. This advantage is the result of combination of the total variation regularizer which is well suited to piecewise smooth images with DRS and randomized Kaczmarz algorithm.

3.3.2 Reconstructed images of ex-vivo canine prostate

The proposed algorithm was used to reconstruct a 3.1 mm thick single transverse slice of an ex-vivo canine prostate. The raw data were collected at the Canadian Light Source by the Prostate Imaging Research Group. A reference image is reconstructed by SkyScan NRecon package using all 3,751 projections. The size of the image is 2500×2500 pixels. Like before, five images were then reconstructed by FBP, POCS, MLEM, ASD-POCS and the proposed algorithm using equally spaced 20%, 30%, 40% and 50% of the full dataset. Figs. 3.5, 3.6 and 3.7 show the visual comparison among the reference image and reconstructed images using 20% (750 views) and 50% (1875 views) of full dataset. Table 3.2 shows three quality metrics, SSIM, PSNR, RE related to different percentages of the projected data. To make clear the advantage of the new proposed algorithm, the quality metrics are plotted separately and shown in Fig. 3.8. Each quality metric is sensitive to a different aspect of image quality and it is shown that the proposed algorithm is superior in all metrics compared to the existing reconstruction algorithms. Fig. 3.9 shows the horizontal intensity profile of images reconstructed by the proposed algorithm and other algorithms. These graphs show that the intensity profile of the proposed algorithm was much closer to the reference image intensity profile in non-edge and specifically in edge regions demonstrating its ability to produce superior quality edges.

Table 3.1 Quality metrics of reconstructed synthetic abdomen phantom

Data Percentage	7%			10%			20%			40%		
Method	SSIM	RE%	PSNR	SSIM	RE%	PSNR	SSIM	RE%	PSNR	SSIM	RE%	PSNR
Proposed	0.97	0.93	50.64	1	0.05	74.78	1	0.02	82.60	1	0.01	84.83
FBP	0.12	34.96	19.18	0.14	29.19	20.75	0.27	16.57	25.67	0.55	9.6	30.41
POCS	0.82	13.28	27.59	0.84	11.59	28.77	0.89	9.82	30.21	0.93	9.21	30.77
MLEM	0.88	11.44	28.89	0.89	9.39	30.60	0.91	6.98	33.17	0.96	5.54	35.17
ASDPOCS	0.88	10.8	29.39	0.93	7.32	32.76	0.96	4.6	36.80	0.98	2.6	41.75

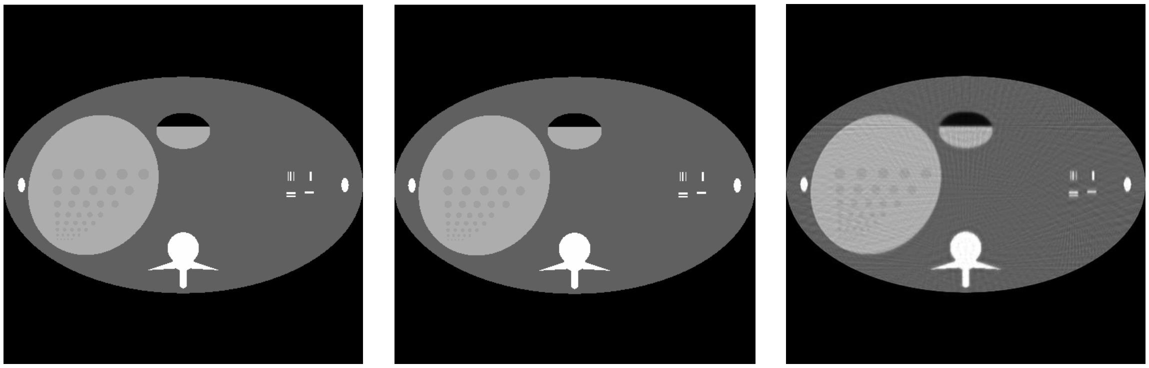

A) Reference **B) Proposed** **C) MLEM**

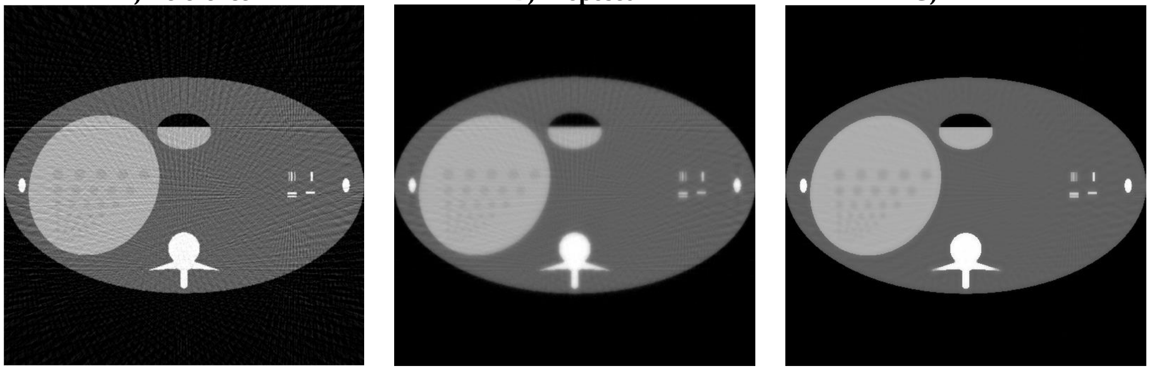

D) FBP **E) POCS** **F) ASD-POCS**

Figure 3.1 Reconstructed synthetic abdomen phantom images with 20% of projected data

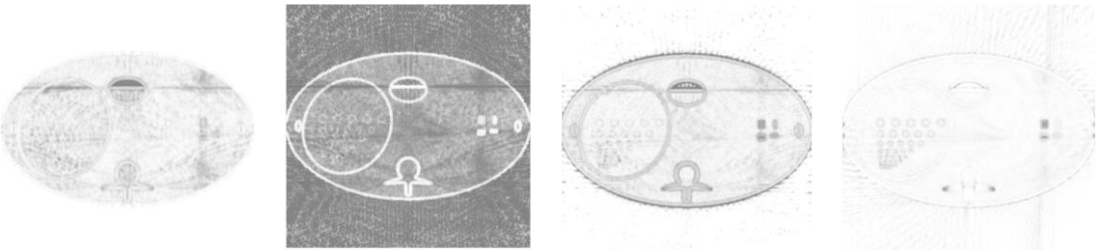

A) MLEM **B) FBP** **C) POCS** **D) ASD-POCS**

Figure 3.2 SSIM index map of images reconstructed with 20% of projected data

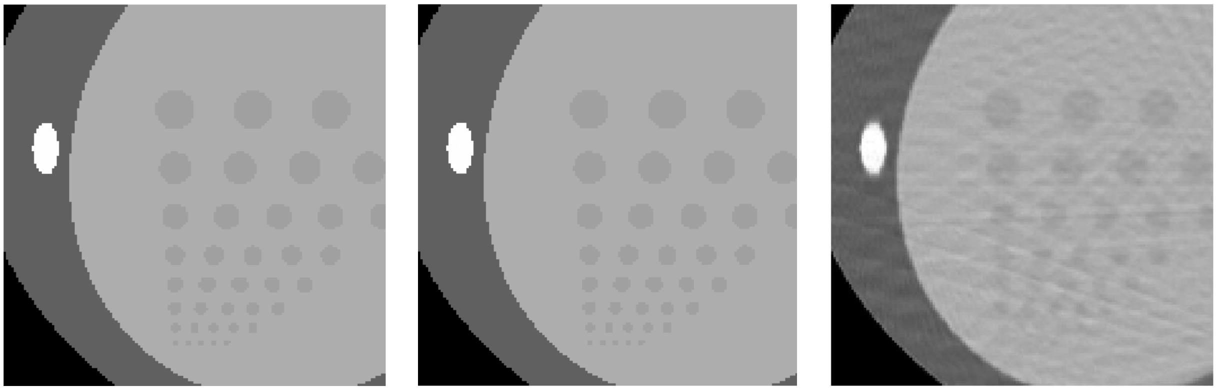

A) Reference **B) Proposed** **C) MLEM**

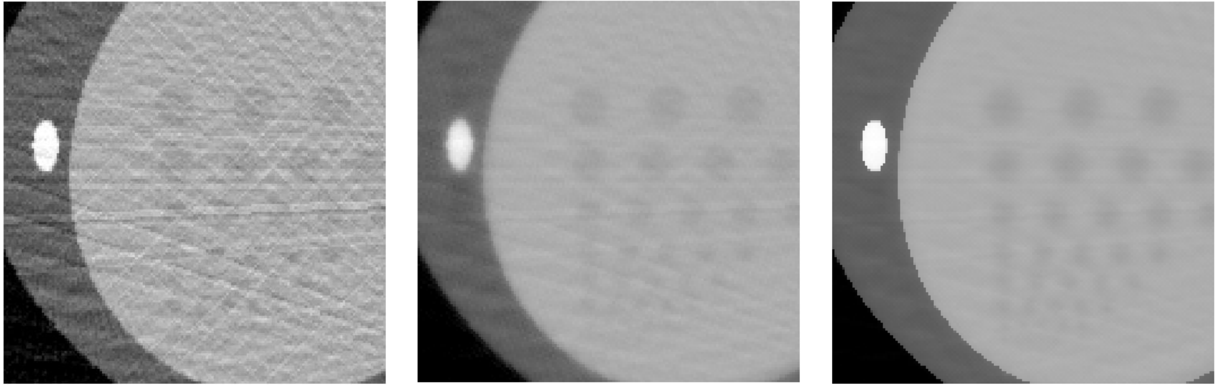

D) FBP **E) POCS** **F) ASD-POCS**

Figure 3.3 Enlarged region of interest in Fig. 3.1

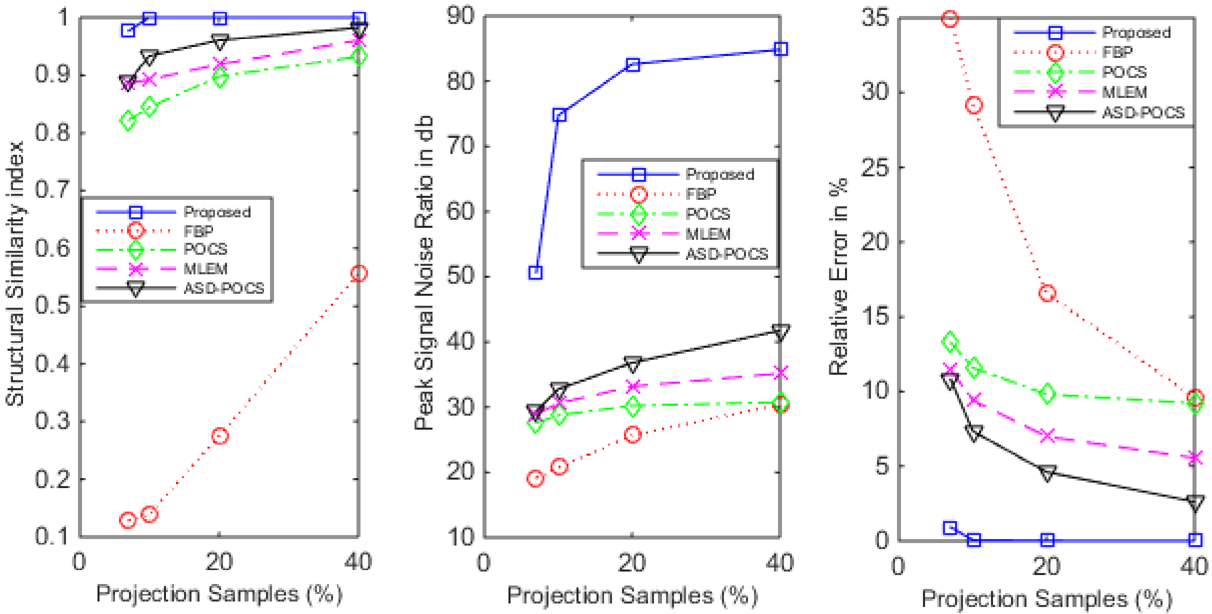

A)SSIM **B)PSNR** **C)RE**

Figure 3.4 Phantom quality metrics vs percentage of projected data

One slice of these reconstructed images is shown in Fig. 3.5, the prostatic urethra is in the central part of image and is zoomed in Figs. 3.6 and 3.7 to better visualize performance of the various algorithms. The FBP reconstructed images in Figs. 3.6 and 3.7 and the line profile in Fig. 3.9 show a large number of pervasive streak artifacts because of the low sample rate. The resolution and image quality are considerably reduced due to these artifacts. As shown in Figs. 3.6 and 3.7 and the line profile in Fig. 3.9, in the POCS and MLEM images, the streak artifacts and noise are decreased, but residual artifacts are still pervasive especially in the POCS (noise and streak artifacts in the black background surrounding the prostate in Fig. 3.5). Moreover, blurring artifact is present and low contrast structures are not visible.

Table 3.2 Quality metrics of reconstructed canine prostate images

Sample Percentage	20%			30%			40%			50%		
Method	SSIM	RE%	PSNR	SSIM	RE%	PSNR	SSIM	RE%	PSNR	SSIM	RE%	PSNR
Proposed	0.61	8.55	28.49	0.68	7.33	29.82	0.74	6.43	30.97	0.78	5.72	31.98
FBP	0.38	15.52	23.31	0.53	11.09	26.23	0.54	10.64	26.59	0.70	7.31	29.85
POCS	0.55	13.25	24.68	0.59	12.39	25.27	0.61	11.96	25.57	0.63	11.7	25.76
MLEM	0.54	11.48	25.93	0.56	10.68	26.56	0.58	10.10	27.04	0.62	8.74	28.30
ASD-POCS	0.60	10.49	26.72	0.66	9.09	27.96	0.70	8.27	28.78	0.73	7.73	29.37

It can be seen in Table 3.2 and Fig. 3.8 that POCS and MLEM algorithms are better than FBP with respect to existing quality metrics at the lower sampling rate (20%). Contrary to this, FBP is more successful than POCS and MLEM using a higher sampling rate (50%). ASD-POCS applies total variation to remove streak artifacts without generation of undesirable effects but as illustrated in Figs. 3.6 and 3.7 a number of low frequency blocky-shaped structures are seen in the smooth regions. In clinical practice, these blocky-shaped structures may obscure the presence of small low contrast details. Finally, as demonstrated in Figs. 3.6 and 3.7 and the line profile in Fig. 3.9, the proposed algorithm is successful in controlling the trade-off between artifact suppression and spatial resolution. We can also see from Fig. 3.8 that the RE is below 10% and the PSNR is more than 25dB for the proposed algorithm. These results indicate that high reconstruction accuracy is achieved using the proposed algorithm. As well, from the SSIM value and visual observation of Figs. 3.6 and 3.7, one may conclude that the proposed algorithm is capable of suppressing streak artifacts and noise, leading to a9n image of acceptable quality from a lower number of views.

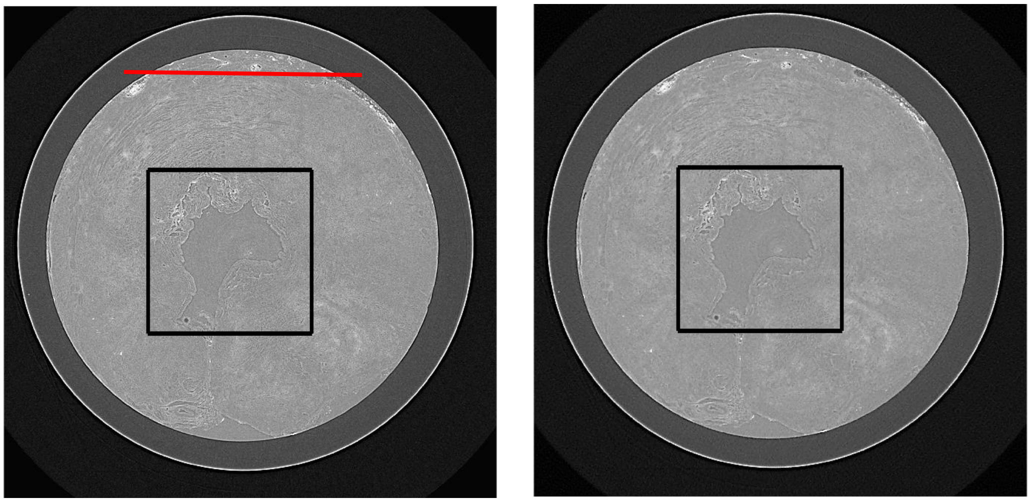

A) Reference B) Proposed

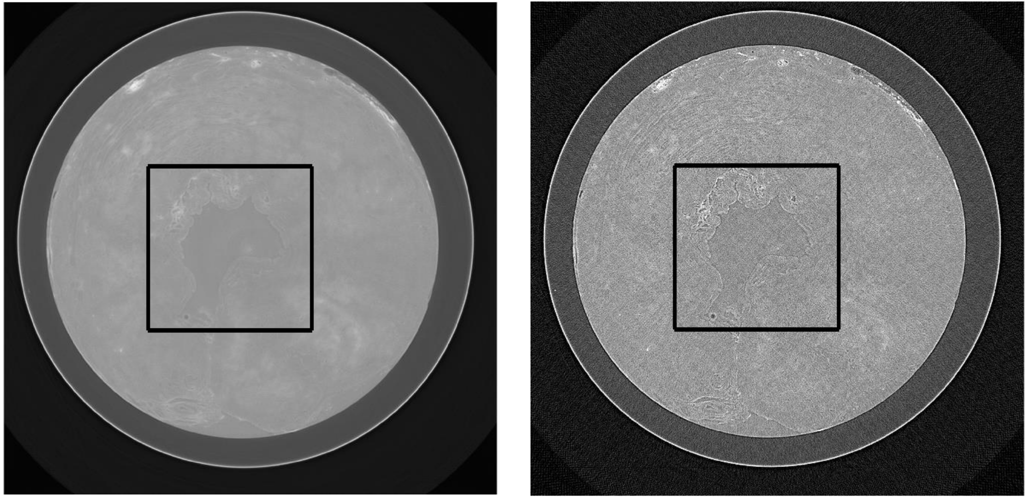

C) MLEM D) FBP

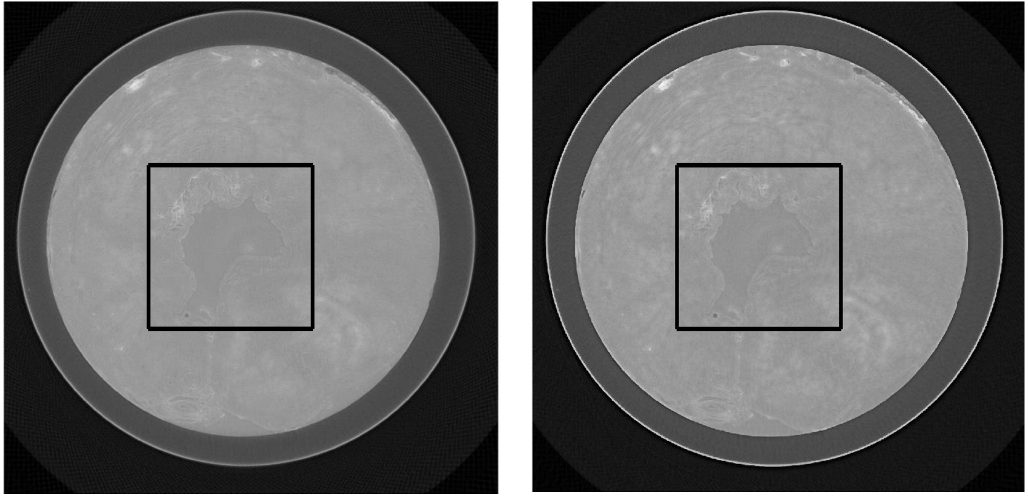

E) POCS F) ASD-POCS

Figure 3.5 Reconstructed canine prostate slice with 20% of projected data; the corresponding zoomed areas are shown in Fig. 3.6

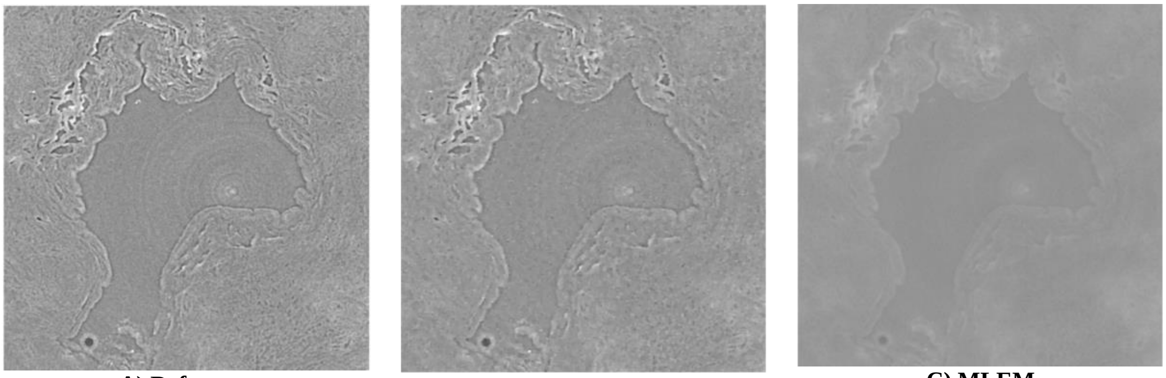

A) Reference **C) Proposed** **C) MLEM**

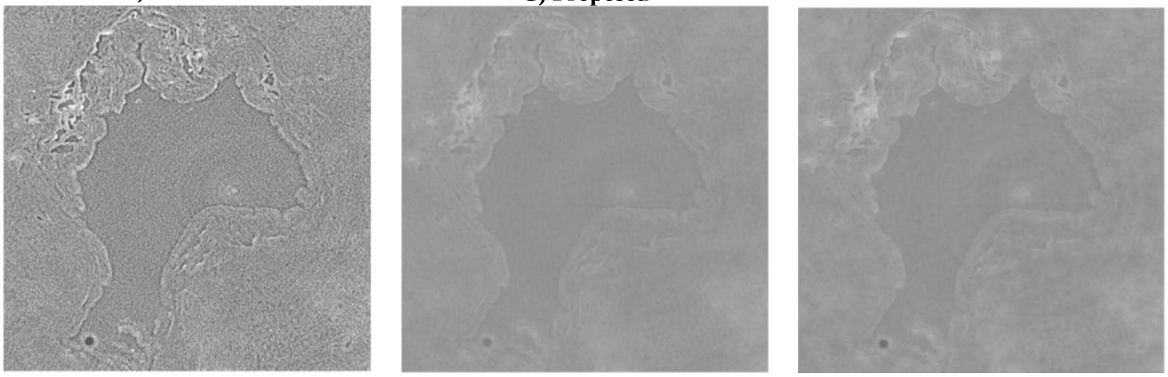

D) FBP **E) POCS** **F) ASD-POCS**

Figure 3.6 Zoomed reconstructed canine prostate slice with 20% of projected samples

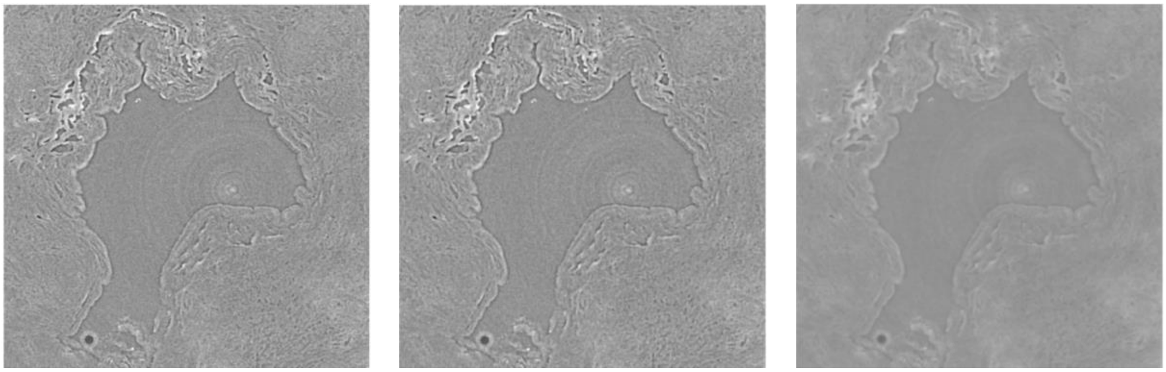

A) Reference **B) Proposed** **C) MLEM**

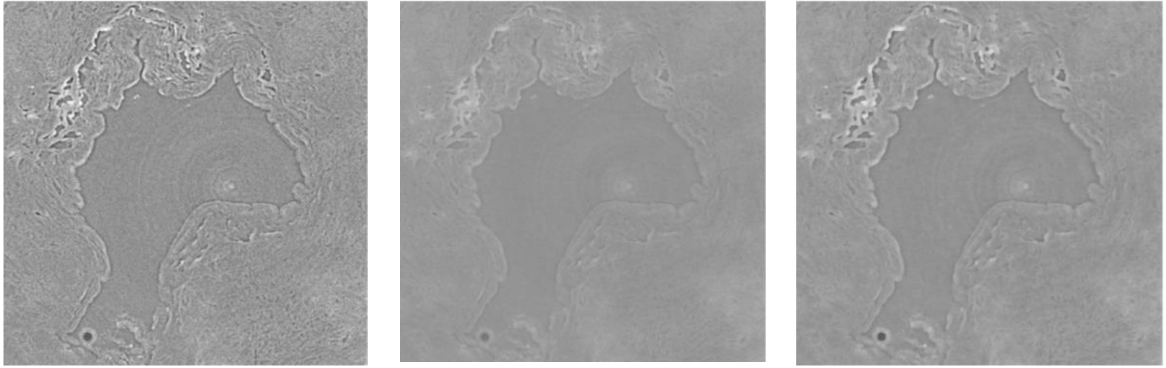

D) FBP **B) POCS** **B) ASD-POCS**

Figure 3.7 Zoomed reconstructed canine prostate slice with 50% of projected samples

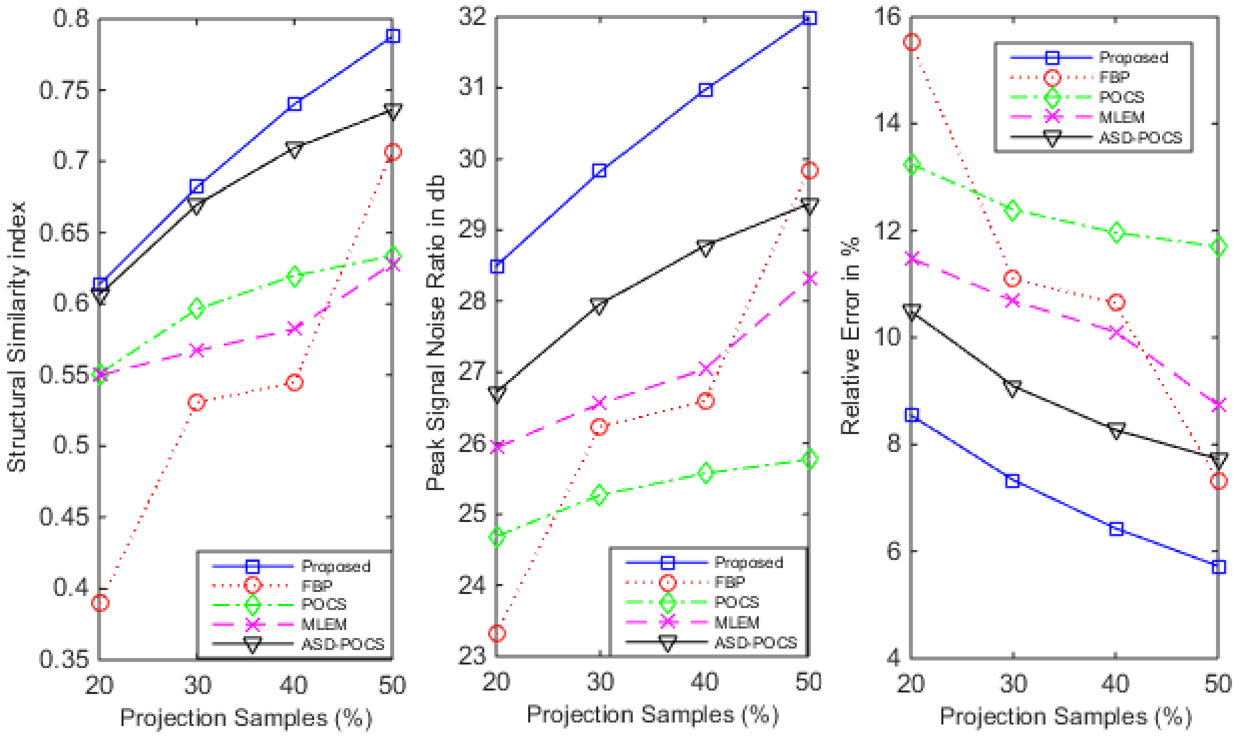

A)SSIM **B)PSNR** **C)RE**

Figure 3.8 Canine prostate image quality metrics vs percentage of projected data

The future work is directed towards using distributed hardware (such as, cloud computing) with our algorithm to reconstruct images from a very large dataset which is typical in synchrotron based medical tomography.

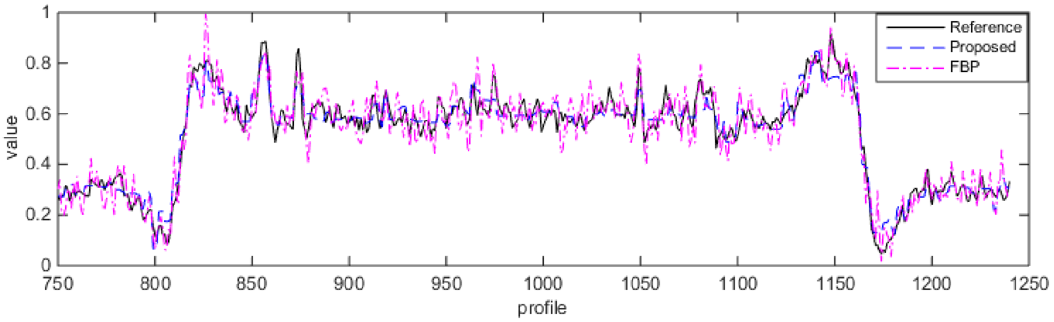

A)FBP

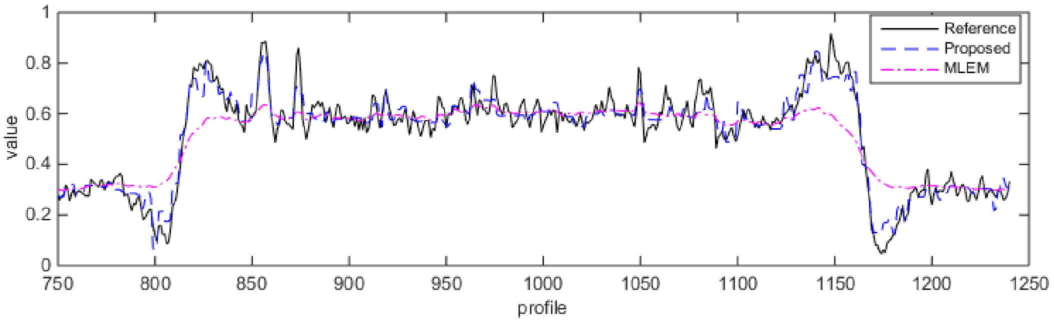

B)MLEM

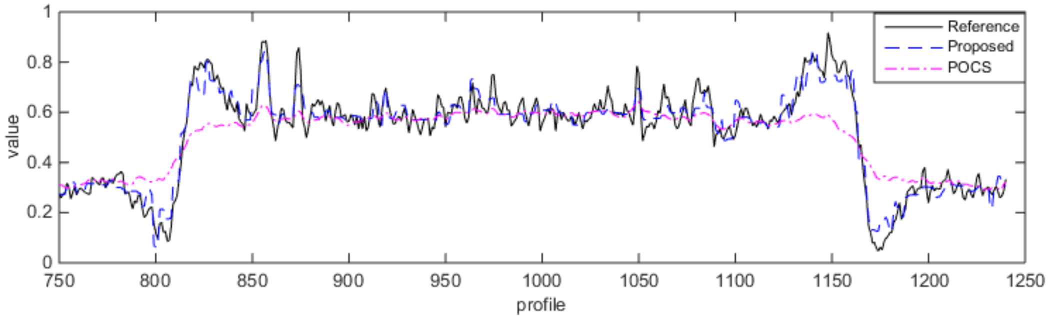

C) POCS

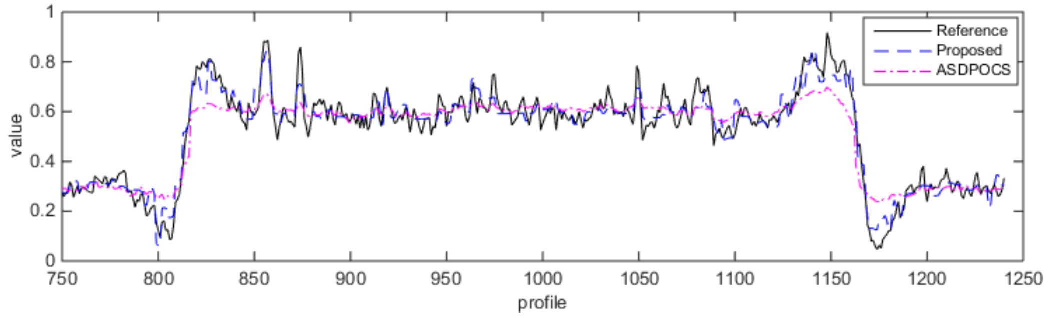

D) ASDPOCS

Figure 3.9 Intensity profiles (red line in Fig. 3.5) of reconstructed canine prostate images with 20% of projected data

3.4 Conclusions

The proposed research reveals the potential of total variation minimization in reconstructing Synchrotron source propagation-based X-ray Phase Contrast Computed Tomography (XPC-CT) by using a novel combination of Douglas-Rachford Splitting (DRS) and randomized Kaczmarz algorithms. After applying DRS to optimize this large-scale non smooth regularized model and using iterative randomized Kaczmarz algorithm, an optimal balance between artifact suppression and spatial resolution is obtained. The algorithm is applied to tomography data collected in the Biomedical Imaging and Therapy Bending Magnet (BMIT-BM) beamline at the Canadian Light Source Visual assessment and quantitative based evaluation metrics are used to show the superiority of the proposed algorithm with respect to a number of recognized reconstruction algorithms using different numbers of projections. The results show that, without compromising image quality, the radiation dose and imaging time can be reduced which is an important step towards transitioning to clinically applicable propagation-based XPC-CT.

References

[C3.1] Heijmink, S.W.T.P.J., Fütterer, J.J., Strum, S.S., Oyen, W.J.G., Frauscher, F., Witjes, J.A. and Barentsz, J.O. State-of-the-art uroradiologic imaging in the diagnosis of prostate cancer. Acta Oncologica 2011; 50 Suppl 1:25-38.

[C3.2] Davis TJ, Gao D, Gureyev TE, Phase-contrast imaging of weakly absorbing materials using hard X-rays. Nature 1995; 373:595-598.

[C3.3] Wilkins SW, Gao D, Pogany A, Phase-contrast imaging using polychromatic hard x-rays. Nature 1996; 384:335-338.

[C3.4] Wu X, Liu H. A general formalism for x-ray phase contrast imaging. J X-Ray Sci Technol 2003; 11:33–42.

[C3.5] Tanaka T., Honda C., Matsuo S., Noma K., Oohara H., Nitta N. The first trial of phase contrast imaging for digital full-field mammography using a practical molybdenum X-ray tube. Invest Radiol 2005; 40(7):385-96.

[C3.6] Wu X, Liu H. Clarification of aspects in in-line phase-sensitive X-ray imaging. Med Phys 2007; 34(2):737-43.

[C3.7] Bravin A., Coan P., Suortti P. X-ray phase-contrast imaging: from pre-clinical applications towards clinics. Phys. Med. Biol 2013; 58:1–35.

[C3.8] Tang L., Li G., Sun YS., Li J., Zhang XP. Synchrotron-radiation phase-contrast imaging of human stomach and gastric cancer: in vitro studies. J Synchrotron Radiat. 2012; 19:319-22.

[C3.9] Snigirev A., Snigireva I., Kohn V., Kuznetsov S., Schelokov I., On the possibilities of x-ray phase contrast microimaging by coherent high-energy synchrotron radiation. Review of Scientific Instruments, 1995; 66 (12): 5486–5492.

[C3.10] Cloetens P., Pateyron-Salomé M., BuffièRe JY., Peix G., Baruchel J., Peyrin F., Schlenker M., Observation of microstructure and damage in materials by phase sensitive radiography and tomography. Journal of Applied Physics 1997; 81 (9): 5878–5886.

[C3.11] Chen, R., Xie, H., Rigon, L., Du, G., Castelli, E., and Xiao, T. Phase Contrast Micro-Computed Tomography of Biological Sample at SSRF. Tsinghua Science and Technology 2010; 15:102-107.

[C3.12] McEwen BF., Downing KH., Glaeser RM. The relevance of dose-fractionation in tomography of radiation-sensitive specimens. Ultramicroscopy 1995; 60:357‑373.

[C3.13] Crowther RA., DeRosier DJ., Klug A. The reconstruction of a three dimensional structure from projections and its application to electron microscopy. Proc. R. Soc. B, 1970; 317:319-340.

[C3.14] Kak AC and Slaney M, Principles of Computerized Tomographic Imaging, New York: IEEE Press 1988.

[C3.15] Wysokinski T., Chapman D., Adams G., Renier M., Suortti P., Thomlinson W. Beamlines of the biomedical imaging and therapy facility at the Canadian Light Source-Part 1. Nuclear Instruments and Methods in Physics Research A, 2007; 582-1:73-76.

[C3.16] Hsieh J. Computed tomography principles, designs, artifacts, and recent advances. Bellingham, WA: SPIE Press; 2003.

[C3.17] Barrett JF, Keat N. Artifacts in CT: recognition and avoidance. Radiographics 2004;24:1679–91.

[C3.18] Beister M, Kolditz D, Kalender WA. Iterative reconstruction methods in X-ray CT. Phys Med 2012; 28:94–108

[C3.19] Herman G.T., Lent A. and Rowland S.W. ART: mathematics and applications. A report on the mathematical foundations and on the applicability to real data of the algebraic reconstruction techniques. Journal of Theoretical Biology, 1973; 42-1:1–32

[C3.20] Shepp L, Vardi Y. Maximum likelihood reconstruction for emission tomography. IEEE Trans Med Imaging 1982; 1:113–22.

[C3.21] Sidky EY, Pan X. Image reconstruction in circular cone-beam computed tomography by constrained, total-variation minimization. Phys Med Biol 2008; 53:4777–807.

[C3.22] Tsaig Y., Donoho DL. Compressed sensing. IEEE Transactions on Information Theory. 2006; 52:1289–1306

[C3.23] Candés EJ., Romberg J., Tao T. Robust uncertainty principles: exact signal reconstruction from highly incomplete frequency information. IEEE Transactions on Information Theory 2006; 52(2):489–509.

[C3.24] Ritschl L., Bergner F., Fleischmann C., Kachelriess M. Improved total variation-based CT image reconstruction applied to clinical data. Phys. Med. Biol. 2011; 56:1545–1561.

[C3.25] Douglas J and Rachford HH, On the numerical solution of heat conduction problems in two or three space variables, Trans. Amer. Math. Soc 1956; 82:421–439.

[C3.26] Strohmer T, Vershynin R., A randomized Kaczmarz algorithm for linear systems with exponential convergence, J. Fourier analysis Appl 2009; 15:262–278.

[C3.27] Ritman EL, Micro-computed tomography – current status and developments, Annu. Rev. Biomed. Eng. 2004; 6:185–208.

[C3.28] Strengell S, Keyriläinen J, Suortti P, Bayat S, Sovijärvi AR, Porra L. Radiation dose and image quality in K-edge subtraction computed tomography of lung in vivo. J Synchrotron Radiat. 2014; 21(6):1305-13

[C3.29] Wang ZT, Zhang L, Huang ZF, Kang KJ, Chen ZQ, Fang QG, Zhu PP. An ART iterative reconstruction algorithm for computed tomography of diffraction enhanced imaging, Chinese Physics C. 2009; 33(11), 975-980.

[C3.30] Wolkowski, B., Snead, E., Wesolowski, M., Singh, J., Pettitt, M., Chibbar, R., Melli, S., Montgomery, J. Assessment of freeware programs for the reconstruction of tomography datasets obtained with a monochromatic synchrotron-based X-ray source. J Synchrotron Radiat. 2015; 22(4): 1130-1138.

[C3.31] http://bruker-microct.com/next/NReconUserGuide.pdf

[C3.32] Chen RC, Dreossi D., Mancini L., Menk R., Rigon L., Xiao TQ, Longo R. PITRE: software for phase-sensitive X-ray image processing and tomography reconstruction. J. Synchrotron Radiat 2012; 19(5):836–845.

[C3.33] http://imagej.nih.gov/ij/

[C3.34] Hegerl R., Hoppe W. Influence of electron noise on three-dimensional image reconstruction. Z. Naturforsch. 1976; 31a:1717‑1721.

[C3.35] Grimm R., Singh H. Rachel R., Typke D., Zillig W., Baumeister W. Electron tomography of ice-embedded prokaryotic cells. Biophys. J. 1998; 74:1031‑1042.

[C3.36] Engeler CE. Preoperative assessment of prostatic carcinoma by computerized tomography. Weaknessess and new perspectives. Urology 1992; 40(4):346-50.

[C3.37] Lustig M., Donoho D., Santos J., Pauly J. Compressed sensing MRI. IEEE Signal Process. Mag. 2008; 25(2):72–82.

[C3.38] Bouhamidi A., Jbilou K. Sylvester Tikhonov-regularization methods in image restoration. J. Comput. Math. 2007; 206:86–98.

[C3.39] Rudin LI, Osher S, Fatemi E. Nonlinear total variation based noise removal algorithms. Physica D 1992; 60:259–68.

[C3.40] Chan TF., Esedoglu S., Park F., Yip MH. Recent developments in total variation image restoration. Handbook of Mathematical Models in Computer Vision. Springer Verlag, 2005.

[C3.41] Blomgren P., Chan TF., Mulet P. and CK. Wong. Total variation image restoration: numerical methods and extensions, Proceedings of the International Conference on Image Processing, 1997; 3: 384–387.

[C3.42] Tibshirani R. Regression shrinkage and selection via the lasso. Journal of the Royal Statistical Society, Series B 1996; 58:267–288.

[C3.43] Bertsekas Dimitri P. Constrained optimization and Lagrange multiplier methods. Athena Scientific, 1996.

[C3.44] Eckstein J, Bertsekas D. On the Douglas Rachford splitting method and the proximal point algorithm for maximal monotone operators. Mathematical Programming 1992; 5: 293-318.

[C3.45] Michailovich O. An iterative shrinkage approach to total-variation image restoration. IEEE Trans. Image Process. 2011; 20-5:1281–1299.

[C3.46] Nocedal, J. and Stephen J. W. Least-Squares Problems. Springer New York, 2006.

[C3.47] Boyd S, Parikh N, Chu E, Peleato B, Eckstein J. Distributed optimization and statistical learning via the alternating direction method of multipliers. Foundations and Trends in Machine Learning 2011; 3:1-122.

[C3.48] Hansen PC., Saxild-Hansen M., AIR Tools - A MATLAB Package of Algebraic Iterative Reconstruction Methods, Journal of Computational and Applied Mathematics. 2012; 236(8):2167-2178.

[C3.49] Wang Z, Bovik AC, Sheikh HR, Simoncelli EP. Image quality assessment: from error visibility to structural similarity. IEEE Transactions on Image Processing 2004; 13: 600–612.

[C3.50] http://www.imp.uni-erlangen.de/phantoms/

4. A Compressed Sensing Algorithm for Reduced-view Image Reconstruction from Real Ex-vivo Synchrotron Absorption Contrast Micro-CT Bone Data

Published as: Melli, S. Ali, Khan A. Wahid, Paul Babyn, David ML Cooper, and Varun P. Gopi. "A sparsity-based iterative algorithm for reconstruction of Micro-CT images from highly undersampled projection datasets obtained with a synchrotron X-ray source." Review of Scientific Instruments 87, no. 12 (2016): 123701.

In the previous chapter, a compressed sensing based reduced-view image reconstruction algorithm was proposed to reconstruct the tomographic image from simulated synchrotron CT data.

The manuscript included in this chapter proposes a compressed sensing algorithm for reduced-view image reconstruction from real ex-vivo synchrotron absorption contrast micro-CT bone data. The goal is to reduce the scan time by reducing the number of projections. In contrast with the previous chapter, where consistent simulated projection data are generated and used for the image reconstruction, data inconsistency caused by noisy and reduced-view projection data is addressed in this chapter. In addition, staircase artifact and long reconstruction time are other image reconstruction challenges. The gradient-based compressed sensing algorithm enforces consistency with the noisy and reduced-view projection data, attenuates the aliasing artifact and recover the spatial resolution. The post-processing 2D wavelet-based image denoising algorithm is used to attenuate the unwanted staircase artifact generated by the gradient-based compressed sensing algorithm while preserving the recovered spatial resolution. The conjugate gradient method and a modified back-projection operator are used to decrease the reconstruction time. Visual and quantitative performance assessments of a reconstructed slice of a femoral cortical bone sample demonstrate the superiority of the proposed algorithm compared to other existing algorithms.

The student (first author) designed the algorithm, processed the raw data, performed the numerical simulation, interpreted the results, designed the figures and wrote the manuscript. K. A. Wahid and, P. Babyn provided equal supervision effort. David ML Cooper was involved in collection of synchrotron data at the Canadian Light Source, including the methods used to collect the data and the technical analyses supporting the quality of the measurements.

A sparsity-based iterative algorithm for reconstruction of Micro-CT images from highly undersampled projection datasets obtained with a synchrotron X-ray source

S. Ali Melli, Khan A. Wahid, Paul Babyn, David M.L. Cooper, Varun P. Gopi

Abstract

Synchrotron X-ray Micro Computed Tomography (Micro-CT) is an imaging technique which is increasingly used for non-invasive in-vivo preclinical imaging. However, it often requires a large number of projections from many different angles to reconstruct high-quality images leading to significantly high radiation doses and long scan times. To utilize this imaging technique further for in-vivo imaging, we need to design reconstruction algorithms that reduce the radiation dose and scan time without reduction of reconstructed image quality. This research is focused on using a combination of gradient-based Douglas-Rachford Splitting and discrete wavelet packet shrinkage image denoising methods to design an algorithm for reconstruction of large-scale reduced-view synchrotron Micro-CT images with acceptable quality metrics. These quality metrics are computed by comparing the reconstructed images with a high-dose reference image reconstructed from 1800 equally spaced projections spanning 180 degrees. Visual and quantitative-based performance assessment of a synthetic head phantom and a femoral cortical bone sample imaged in the Biomedical Imaging and Therapy Bending Magnet (BMIT-BM) beamline at the Canadian Light Source demonstrate that the proposed algorithm is superior to the existing reconstruction algorithms. Using the proposed reconstruction algorithm to reduce the number of projections in synchrotron Micro-CT is an effective way to reduce overall radiation dose and scan time which improves in-vivo imaging protocols.

Index terms

medical imaging; synchrotron imaging; low-dose Micro-CT; image reconstruction; compressed sensing;

4.1 Introduction

X-ray Computed Tomography (CT) is a non-invasive imaging technique where projections (radiographs) taken from different viewing angles are processed by a computer to reconstruct the cross-sectional (tomographic) image of the scanned object. After the development of the digital computer, the first commercial CT scanner was introduced early in the 1970s [C4.1]. Since then, there has been competing trends to increase scanner resolution and decrease the needed x-ray dose. Micro Computed Tomography (Micro-CT) scanners can provide high spatial resolution [C4.2]. Micro-CT using synchrotron x-ray radiation sources can provide spatial resolution between 1 and 10 µm [C4.3]. Synchrotron beamlines generate parallel beam monochromatic x-rays in a pre-selectable energy to eliminate cone beam and beam-hardening artifacts. Synchrotron x-rays are also highly intense which boosts the signal to noise ratio allowing faster scan time [C4.4, C4.5]. Thus, these advantages of synchrotron Micro-CT make this imaging method an important tool for biological research and an excellent platform for testing reconstruction algorithm improvements which can be ported to conventional systems.

Traditionally, tomographic reconstruction techniques require a large number of projection views to reconstruct synchrotron Micro tomographic images with the fine spatial resolution necessary to view as much detail as possible in the sample field of view [C4.6]. This exposes the specimen to a large amount of x-ray radiation which can damage living specimens. This also increases scan time and consequently the likelihood of involuntary specimen movements so motion artifact in the reconstructed images will be more likely. One way to reduce overall scan time and radiation dose is to reduce the acquisition time for each projection, in fact, this is the only parameter that can be used to control the amount of synchrotron radiation at each angle as the radiation intensity is almost constant per projection [C4.7]. However, detector sensitivity and readout speed may not allow the exposure time per projection to be less than a certain value. Also, a very noisy tomographic image will be reconstructed in a low exposure time per projection because of the low projection signal to noise ratio [C4.8]. Another approach for decreasing the total scan time and radiation dose is to reduce the number of projections needed to reconstruct the tomographic images. Analytical reconstruction methods such as Filtered Back Projection (FBP) which is often used in medical CT scanners has acceptable performance when there are a large number of closely sampled projections over the scanning angular range, otherwise, aliasing artifacts will occur in the reconstructed image

[C4.9]. On the other hand, iterative reconstruction methods such as Projection onto Convex Sets (POCS) [C4.10, C4.11] can be utilized to reconstruct high-quality tomographic images when noisy and/or slightly reduced projection data are available. Methods based on iteratively solving linear tomographic equations may also fail to maintain image quality with a highly reduced number of projections. The reason is that when the number of projections is severely reduced, the linear tomographic equations will be highly ill-conditioned, and the subsequently reconstructed image will be highly sensitive to data noise and modeling error [C4.12].

Lately, Compressed Sensing (CS) theory has spurred great interest in the signal-processing research community. Although, there is no equations that show the relationship between image sparsity and sufficient number of projections for tomographic image recovery in CS theory, the results in [C4.13, C4.14] demonstrate that a phase transition from non-recovery to recovery as happened in compressed sensing can also take place in sparse-view tomographic reconstruction. For practical large-scale tomographic reconstruction, a compressed sensing algorithm called ASD-POCS was proposed in [C4.15, C4.16] to minimize the total variation (TV) of the image subject to the constraint that the estimated projection data is within a specified tolerance of the available data and that the values of the volume image are non-negative. In [C4.17], the application of this algorithm to low-dose Micro-CT of real animal organs was investigated. The problem of this heuristic algorithm is that the reconstructed image depends on the parameters of the optimization problem, which the algorithm aims to solve, and all the parameters of the algorithm itself [C4.18]. More parameters make characterization of the algorithm more difficult. Moreover, the nonsmooth regularizers such as sparsity-promoting ones based on the $l1$-norm are not differentiable everywhere, so, conventional methods (e.g., ASD-POCS) employs differentiable approximation (e.g., using “corner-rounding”) which leads to slow convergence [C4.19]. For solving this problem, in the past few years, state-of-the-arts first-order splitting based algorithms such as (M)FISTA [C4.20, C4.21], Split-Bregman-type (SB) [C4.22], ADMM [C4.23] and Chambolle-Pock [C4.24, C4.25] which can handle nonsmooth regularizers without corner rounding were proposed. These algorithms are inter-related [C4.26], but there are differences in parameterization which can have significant impact on convergence in practice. Split-Bregman (SB) method converges to a reasonable practically useful precision quickly and was used in the reduced-view CT reconstruction algorithm (SpBR-TV) [C4.27]. However, total variation (TV)-based reconstruction algorithms such as SpBR-TV have been shown to work well when dealing with piecewise smooth images, but it may lead to unwanted staircase artifact when applied to images that contain textures and shading [C4.28, C4.29].

Our proposed algorithm combines gradient-based Douglas-Rachford Splitting (DRS) and discrete wavelet packet shrinkage image denoising methods to design an algorithm for reconstruction of large-scale synchrotron Micro-CT images from a reduced number of projections. The DRS method is a simple but powerful method for distributed convex programming first proposed in [C4.30] for solutions of small-scale and easy-to-solve sub-problems which can be coordinated to find the solution of large-scale optimization problems. This method was used to solve the gradient-based large-scale compressed sensing optimization problem to reconstruct uniform regions within organs while preserving strong edges at organ boundaries. The discrete wavelet packet shrinkage image denoising was used to mitigate the effect of any potential noise in the final reconstructed image [C4.31]. The wavelet packet transform compacts the energy of prominent features (e.g., edges) which are dominant and global into a small number of coefficients with large magnitude and spreads the energy of noise which is sub-dominant and local into a large number of coefficients with small magnitude. Typically, keeping large coefficients and removing small ones reduces the energy of the noise [C4.32, C4.33].

4.2 Material and Methods

4.2.1 Synchrotron Micro-CT data acquisition

Micro-CT data were obtained from at the Biomedical Imaging and Therapy Bending Magnet (BMIT-BM) Beamline at the Canadian Light Source (CLS). This is a bend magnet beamline with a field strength of 1.354 T. The ring energy is 2.9 GeV and the storage ring current is a maximum of 250 mA operating in decay mode. The critical energy of the bend magnet source is 7.57 keV. The beamline uses a Si (2,2,0) Bragg double crystal monochromator at a distance of 13.2 m from the source. A block of femoral cortical bone was placed on a rotating mechanical stage that was 26 m away from the synchrotron source so that the x-ray beam can be assumed to be parallel. Projection data were collected with a Hamamatsu C9300 (Hamamatsu Photonics, Hamamatsu, Japan) CCD camera fitted with a beam monitor with a 10 μm thick gadolinium oxysulfide scintillator. The white beam filtered with aluminum (6 mm) and tin (0.5 mm) was used to generate a spike of x-rays in the 25–29 keV energy range. The sample was rotated through 180° in 0.1° steps, generating 1800 projections. An exposure time of 1 sec per frame and two-frame averaging was employed for each of the 1800 projections. The optical configuration provided an effective pixel size of 5 μm. Dark and flat projections were taken before and after the sequential angular projections. The acquisition system used 12-bit TIFF greyscale digital format to save the calibration and tomographic data.

4.2.2 Synchrotron Micro-CT data preprocessing

Projection data required preprocessing before sinogram formation, including dark and flat field correction, projection alignment, beam power normalization and logarithm transformation. Dark and flat field correction compensates spatial variation in beam intensity caused by different detector pixel sensitivities and/or distortions in optical path and it also compensates different dark currents in detector pixels so that a uniform signal creates a uniform output. Projection alignment was needed because it is practically difficult to exactly match specimen rotation center with the center of the projection images and finally beam power normalization was used to compensate the slight variations in the beam intensity happening over time. After logarithm transformation, the full sinogram dataset (1800 projections) was formed by collecting the preprocessed signal along a specific detector row in the 2D projection plane for all angular views along the 180° angular range and arranging them side by side to reconstruct the reference image. Also, the projection data was sampled uniformly along angular views and preprocessed to produce undersampled sinogram datasets which were used in the reconstruction algorithms. Ring artifact created by defective pixels on the detector or a small variation in filtered beam can be removed from full and undersampled sinogram datasets before the application of the reconstruction algorithms [C4.34]. 121 by 2791 pixel preprocessed projection datasets which were acquired at angles 0°and 180° (initial and final angles) and a 270 by 2791 pixel sinogram dataset which was created by putting together the middle rows of the preprocessed projection data of 270 angular views along the 180° angular range, were shown in Fig. 1.

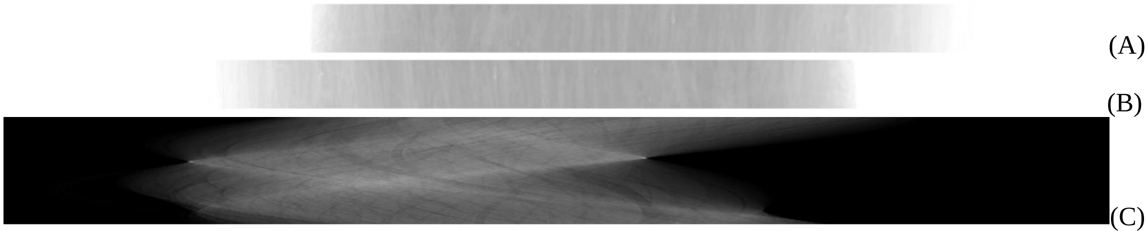

Figure 4.1 (A) Projection dataset at angle 0°, (B) projection dataset at angle180°, (C) sinogram dataset (270 views)

4.2.3 Imaging model and optimization formulation

The basic algebraic imaging model for a 2D synchrotron X-ray Micro-CT is:

$$y = Au \tag{4.1}$$

Where $u \in R^n$ is a vector of image pixel values modeling spatially varying linear attenuation coefficient, $A \in R^{m\times n}$ is the discrete radon transform [C4.11] modeling the parallel forward projection operator which yields noisy undersampled ($m < n$) sinogram dataset $y \in R^m$. As discussed in [C4.35, C4.36, C4.37, C4.39], both sides of Eq. (4.1) can be multiplied by the FBP operator to form an equivalent preconditioned Eq. (4.2). The eigenvalues of square matrix FA which is diagonally dominant with positive diagonal elements are positive and clustered closer together than the eigenvalues of square matrix A^TA [C4.37].

$$Fy = FAu, \quad F = A^TR \tag{4.2}$$

The superscript T represents the transpose operation, A^T is the discrete counterpart of the adjoint of the radon transform modeling the parallel back-projection operator and R is the discrete counterpart of 1D convolution operator (band-limited ramp filter kernel) which is defined in the discrete inverse radon transform [C4.38]. To view this as an optimization problem, we must find a generalized squared-error function that is minimized by the solution u given by Eq. (4.3) [C4.39]:

$$f_1(u) \equiv \frac{1}{2}\|Au - y\|_R^2 = \frac{1}{2}(Au - y)^T R(Au - y) \tag{4.3}$$

Taking the derivative of Eq. (4.3) with respect to u and putting it equal to zero yields Eq. (4.2). On the other hand, the medical tomographic images are almost uniform within the organs with small number of abrupt variations at the organ boundaries [C4.18], so the 2D gradient transform is used as the sparsifying transformation.

According to the CS theory, an optimization problem called generalized Lasso [C4.40, C4.41] is formed to search a sparse gradient image while minimizing the generalized squared-error function in Eq. (4.3):

$$\min_{u \in R^n} \quad \frac{1}{2}\|Au - y\|_R^2 + \lambda\|Gu\|_{l_1} \quad , \quad \lambda > 0 \tag{4.4}$$

Where $G \in R^{n\times 2n}$ is 2D gradient operator defined in Eq. (4.5), $\|x\|_{l_1}$is $\ell 1$-norm which is defined as sum of the absolute pixel values and λ is the parameter which controls the trade-off between spatial resolution and the suppression of artifacts/noise.

$$GH_{ij}(u) := \begin{cases} u_{i+1,j} - u_{i,j} : i < \sqrt{n} \\ \quad 0 \quad\quad : i = \sqrt{n} \end{cases} \qquad\qquad Gv_{ij}(u) := \begin{cases} u_{i,j+1} - u_{i,j} : j < \sqrt{n} \\ \quad 0 \quad\quad : j = \sqrt{n} \end{cases}$$

$$G(u) := \begin{pmatrix} GH_{ij}(u) \\ Gv_{ij}(u) \end{pmatrix} \tag{4.5}$$

4.2.4 Proposed Reconstruction algorithm

Consider a generalization of problem (4.4) where a regularizing function is added to a data fidelity function, i.e.:

$$\min_{u \in R^n} \quad f_1(u) + f_2(Gu) \tag{4.6}$$

Where $f_1 : R^n \to R$ is a data fidelity function and $f_2 : R^p \to R$ is a regularizing function which is a closed, proper and convex function and $G \in R^{n\times p}$ is an arbitrary linear operator.

Our approach to solve the optimization problem (4.6) is to convert it into an equivalent constrained optimization problem by using variable splitting method as shown in Eq. (4.7):

$$\min_{u,v} \quad f_1(u) + f_2(v) \quad S.T. \quad v = Gu \tag{4.7}$$

The global minima of a convex function subject to equality constraint can be found by forming an unconstrained optimization problem followed by a dual variable update as follows [C4.42]:

Loop

$$\min_{u,v} \quad f_1(u) + f_2(v) + b^T(Gu - v) + \frac{1}{2\mu}\|Gu - v\|_{l_2}^2 \tag{4.8}$$

$$b := b + \frac{1}{\mu}(Gu - v) \quad (4.9)$$

Until stop condition is satisfied

Where, $b \in R^p$ is the vector of dual variables, $\|x\|_{l_2}$ is Euclidean norm which is defined as square root of sum of the squared pixel values and $\mu > 0$ is called the penalty parameter. The advantage of adding the penalty term $\frac{1}{2\mu}\|Gu - v\|_{l_2}^2$ to the unconstrained formula is to guarantee the global algorithm convergence.

The optimization problem (4.8) and dual variables update formula (4.9) are rewritten in a new form by merging the linear function $b^T(Gu - v)$ and quadratic function $\frac{1}{2\mu}\|Gu - v\|_{l_2}^2$, and also scaling the dual variables:

Loop

$$\min_{u,v} \quad f_1(u) + f_2(v) + \frac{1}{2\mu}\|Gu - v + d\|_{l_2}^2 \quad , \quad d = \mu b \quad (4.10)$$

$$d := d + (Gu - v) \quad (4.11)$$

Until stop condition is satisfied

The optimization problem in Eq. (4.10) is solved by applying Douglas-Rachford Splitting (DRS) algorithm. This algorithm is helpful when the optimization problem with respect to u and v (Eq. (4.12) and Eq. (4.13)) is efficiently solved while the joint minimization of Eq. (4.10) is difficult to evaluate. For that reason, Eq. (4.10) is decomposed into sub-optimization problems by separately minimizing with respect to u and v. These operations are followed by a dual variable update formula as below:

Loop

$$u_{k+1} := \quad \min_{u} \quad f_1(u) + \frac{1}{2\mu}\|Gu - (v_k - d_k)\|_{l_2}^2 \quad (4.12)$$

$$v_{k+1} := \quad \min_{v} \quad f_2(v) + \frac{1}{2\mu}\|v - (Gu_{k+1} + d_k)\|_{l_2}^2 \quad (4.13)$$

$$d_{k+1} := \quad d_k + (Gu_{k+1} - v_{k+1}) \quad (4.14)$$

Until stop condition is satisfied

Where, k is a loop counter. The convergence analysis of the DRS algorithm was discussed in [C4.43]. It shows that it is not necessary to exactly solve the minimization problem in Eq. (C4.12) and Eq. (C4.13); if the sequence of errors is absolutely summable, global convergence will be guaranteed. Depending on the functions used in Eq. (C4.12) and Eq. (C4.13), closed form or iterative formulations are used to update u and v efficiently. If the data fidelity function $f_1(u)$ is smooth, which is normally the case, the gradient method can be used to solve Eq. (4.12). Moreover, the regularizing function $f_2(v)$ which is normally used in the compressed sensing reconstruction is a non-smooth ℓ1-norm function. In this case, sub differential calculus and proximal operator [C4.44] defined in Eq. (4.15) can be used to evaluate Eq. (4.13). The proximal operator $\mathbf{prox}_f : R^n \rightarrow R^n$ of f with parameter μ is defined by:

$$\mathbf{prox}_{\mu f}(w) := \min_{s} \quad f(s) + \frac{1}{2\mu}\|s - w\|_{l_2}^2 \tag{4.15}$$

Using this operator and smoothness of data fidelity function, the DRS algorithm equations are recast as follows:

Loop

$$u_{k+1} := \quad \mathbf{Root}\left(\frac{\partial f_1}{\partial u} + \frac{1}{\mu} G^T(Gu - (v_k - d_k))\right) \tag{4.16}$$

$$v_{k+1} := \mathbf{prox}_{\mu f_2}(Gu_{k+1} + d_k) \tag{4.17}$$

$$d_{k+1} := \quad d_k + (Gu_{k+1} - v_{k+1}) \tag{4.18}$$

Until stop condition is satisfied

The described algorithmic framework is applied to Eq. (4.4). This problem has the form (4.6) with:

$$f_1(u) \equiv \frac{1}{2}\|Au - y\|_R^2 = \frac{1}{2}(Au - y)^T R(Au - y), f_2(v) \equiv \lambda\|v\|_{l_1} \tag{4.19}$$

Derivative of quadratic data fidelity function $f_1(u)$ is $\frac{\partial f_1}{\partial u} = A^T R(Au - y)$ which is used to instantiate Eq. (4.16). After doing some basic mathematical operations, Eq. (4.20) is derived:

$$u_{k+1} := (A^T RA + \frac{1}{\mu} G^T G)^{-1}(A^T Ry + \frac{1}{\mu} G^T(v_k - d_k)) \tag{4.20}$$

The linear conjugate gradient (CG) method [C4.45] is used to approximately solve this equation. The advantage of this method is that it can solve large-scale linear equations without a need to explicitly inverse the coefficient matrix.

Definition of proximal operator, element-wise sub differential calculus and derivative of absolute value [C4.46] are used to instantiate Eq. (4.17). After doing some basic mathematical operations, Eq. (4.21) is derived:

$$v_{k+1} := ST_{\mu\lambda}(Gu_{k+1} + d_k), ST_{\kappa}(a) = \begin{cases} a - \kappa & a > \kappa \\ 0 & |a| \leq k \\ a + \kappa & a < -k \end{cases} \tag{4.21}$$

This shrinkage operator which is called soft threshold operator is extremely fast and requires only a few operations per element of operand.

Additionally, the discrete wavelet packet shrinkage image denoising technique was used to suppress the remaining noise. Therefore, the Symlet' 4-tap orthonormal wavelet filter bank, universal threshold selection rule [C4.47] and soft thresholding method were selected to be used in a 5-level wavelet packet decomposition and reconstruction.

Finally, the proposed algorithm is summarized as follows:

Initialize $\lambda > 0, \mu > 0, u = 0, v = 0, d = 0, k = 0$

Loop ($k := k + 1$)

$$u_{k+1} := \quad (A^T RA + \frac{1}{\mu} G^T G)^{-1} (A^T Ry + \frac{1}{\mu} G^T (v_k - d_k)) \tag{4.22}$$

$$v_{k+1} := \quad ST_{\mu\lambda}(Gu_{k+1} + d_k) \tag{4.23}$$

$$d_{k+1} := \quad d_k + (Gu_{k+1} - v_{k+1}) \tag{4.24}$$

Until $\frac{\|u_{k+1} - u_k\|_{l2}}{\|u_k\|_{l2}} < \varepsilon$

$$u := \quad WP^{-1} \Gamma_G WP(u) \tag{4.25}$$

Where the operators WP and WP^{-1} stand for the forward and inverse discrete wavelet packet transformations, respectively, and Γ_G is a wavelet-domain point-wise threshold operator with a global threshold.

To decrease the convergence time, the linear conjugate gradient method should be initialized by solution u_k obtained in the previous DRS iteration. With this initialization procedure, the number of iterations in CG method (inner iterations) reduces to a few numbers while the global DRS method (outer iterations) converges [C4.48].

4.2.5 Assessment of image quality

Both reference-based quantitative and visual assessments were used to compare the performance of the proposed algorithm with other existing reconstruction methods. It is assumed that a high x-ray dose image is available to be used as a reference image against which the reconstructed image is to be compared.

4.2.5.1 Quantitative assessment

Structural SIMilarity (SSIM) index is a metric for measuring the structural similarity between two images. If ρ and t are two local image windows selected from the same position of two input images, SSIM is defined as follows [C4.49]:

$$SSIM(\rho, t) = \frac{2\mu_\rho\mu_t+C1}{\mu_\rho^2+\mu_t^2+C1} \cdot \frac{2\sigma_\rho\sigma_t+C2}{\sigma_\rho^2+\sigma_t^2+C2} \cdot \frac{\sigma_{\rho t}+C3}{\sigma_\rho\sigma_t+C3} \tag{4.26}$$

Where, μ_ρ and μ_t are the averages, σ_ρ and σ_t are the standard deviations and $\sigma_{\rho t}$ is the covariance of the local windows. 2C3 = C2 and C1 are constants to stabilize division. The overall SSIM index is calculated by averaging the SSIM map along the entire image. A higher SSIM index indicates superior image quality.

Peak Signal to Noise Ratio (PSNR) and Relative error (RE) are error sensitive quality metrics defined as follows:

$$PSNR(db) = 10\, log_{10}\left(\frac{Peak^2}{MSE}\right) \tag{4.27}$$

Where, Peak is the highest pixel value, e.g. in the case of 12-bit pixel representation, it is 1023; MSE is the mean square error between the reconstructed and reference images.

$$RE(\%) = \frac{\|u_{ref}-u_{rec}\|_2}{\|u_{ref}\|_2} \times 100 \tag{4.28}$$

Where, u_{rec} and u_{ref} are the reconstructed and reference images which are converted into the column vectors.

The SSIM index considers image degradations as perceived changes in structural information. Therefore, it is more consistent then PSNR and RE with human visual system because human visual perception is highly adapted for extracting structural information from a scene [C4.49].

4.2.5.2 Visual Assessment

The images which were reconstructed by the different reconstruction algorithms i.e. FBP, POCS, ASD-POCS, SpBR-TV and the proposed algorithm at different numbers of projections were visually compared with the reference image to assess the reconstruction process.

4.3 Experimental Result and Discussion

The proposed algorithm along with four existing reconstruction methods was used to reconstruct a synthetic FORBILD head phantom and a single transverse slice of a femoral cortical bone. In both cases, the reconstruction algorithms were implemented at different numbers of projections that were uniformly sampled from the full projection dataset. MATLAB R2014b software was used to implement the algorithms on a Desktop PC with six Intel® Xeon® CPU 2GHz processors and 32GB memory.

4.3.1 Simulation - reconstructed images of a synthetic head phantom

A synthetic FORBILD head phantom [C4.50] was used as the ground truth image in the first experiment because it has features with different sizes. The size of this phantom image is 256×256 pixels. Five images were reconstructed by the FBP, POCS, ASD-POCS, SpBR-TV methods and the proposed algorithm using 15, 25, 45 and 90 projections. Table 4.1 shows the quality assessment metrics of reconstructed images with different numbers of projections. The proposed algorithm has the highest PSNR, SSIM and lowest RE with respect to other methods even when the number of projections is only 15. The difference in results between the proposed algorithm and the other methods is from the fact that FORBILD head phantom is uniform within organs and has a limited number of abrupt variations at the organ boundaries. This structure completely corresponds with the prior assumption in the proposed algorithm i.e. gradient domain sparseness. To better illustrate the effectiveness of the proposed algorithm, the quality metrics were plotted individually in Fig. 4.2. In addition, a visual comparison of the reference image with the other reconstructed images using 45 projections was shown in Fig. 4.3. As shown in Fig 4.3E, the aliasing artifact generated by incomplete projected data is obviously apparent in the image reconstructed by FBP method. Although the aliasing artifact is somewhat suppressed in the image reconstructed by POCS method (Fig. 4.3F), the blurring artifact is generated which reduced the image spatial resolution. The ASD-POCS method recovers smooth (low spatial frequency) regions and reduces or completely removes aliasing artifacts in these areas but as shown in the enlarged area (Fig. 4.3C), the small (high spatial frequency) structures are over-smoothed. The image reconstructed by the SpBR-TV method in Fig. 4.3D shows that the method is successful in preserving prominent edges and at the same time suppressing aliasing artifact without generation of blurring artifact or over-smoothed image. However, this method suffers from staircase effect. On the other hand, as shown in Fig. 4.3B, the proposed algorithm suppresses the aliasing artifact and simultaneously almost preserve all image features. The enlarged image areas are shown in Fig. 4.3 to better visualize the quality of the reconstructed images. According to the result shown, we can conclude that the proposed algorithm is more successful in forming artifact suppression – spatial resolution trade-off than the other methods.

Table 4.2 Quality metrics of reconstructed synthetic FORBILD head phantom Images

Number of Projections	15			25			45			90		
Method	SSIM	RE%	PSNR	SSIM	RE%	PSNR	SSIM	RE%	PSNR	SSIM	RE%	PSNR
Proposed	0.77	21.78	26.31	0.99	8.64	33.58	0.99	3.82	38.96	1	2.93	40.09
SpBR-TV	0.66	32.88	24.35	0.90	13.11	29.77	0.92	8.96	31.57	0.99	3.28	39.12
FBP	0.19	69.93	16.18	0.22	48.80	18.36	0.29	29.69	21.17	0.47	19.45	23.66
POCS	0.40	44.26	20.15	0.45	36.94	20.78	0.50	27.51	21.85	0.62	19.98	23.43
ASD-POCS	0.58	35.78	22.00	0.78	22.85	24.95	0.91	18.16	25.44	0.96	12.26	27.67

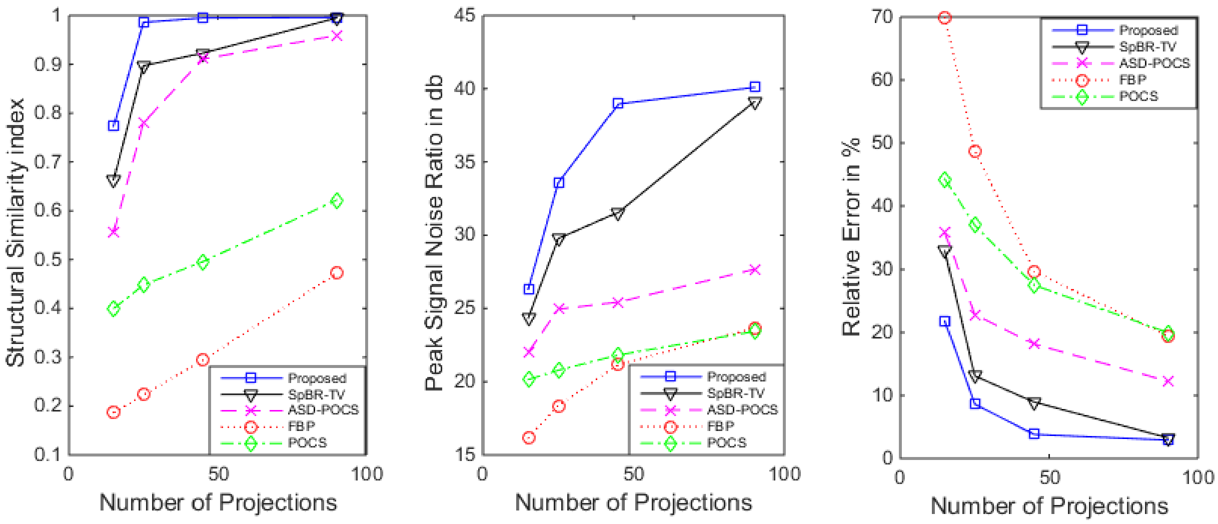

Figure 4.2 Synthetic FORBILD head phantom image quality metrics vs Number of projections

4.3.2 Real data - reconstructed images of a femoral cortical bone

The proposed algorithm was used to reconstruct a single 2D slice of a block of femoral cortical bone. A reference image with the size of 2791×2791 pixels was reconstructed by the FBP method using the full sinogram dataset derived from all 1800 equally spaced projections spanning 180 degrees. Five images were reconstructed by FBP, POCS, ASD-POCS, SpBR-TV and the proposed algorithm using three different collections of undersampled sinogram data i.e. 5% (90 views), 10% (180 views) and 15% (270 views) that were uniformly sampled from the full projection dataset. The features of interest in these bone sections are holes (vascular canals) with different sizes.

The images reconstructed by the FBP method in Figs. 4.5E, 4.6E and the line profiles in Figs. 4.7, 4.8A show a pervasive aliasing artifact which is created because of insufficient numbers of projection. Therefore, the image quality is considerably reduced and there is a high chance that false features that are created by this severe artifact incorrectly identified as true holes. The image reconstructed by the POCS method in Figs. 4.5F, 4.6F and the line profiles in Figs. 4.7 and 4.8B show that the aliasing artifact is decreased but blurring artifact that is created by this method reduces the spatial resolution. Thus, image details such as small holes that are visible in the FBP reconstructed image have been hidden by the blurring artifact. However, as illustrated in Table. 4.2 and Fig. 4.4, the POCS method is far superior to the FBP method in terms of existing quality metrics especially at highly incomplete projected data.

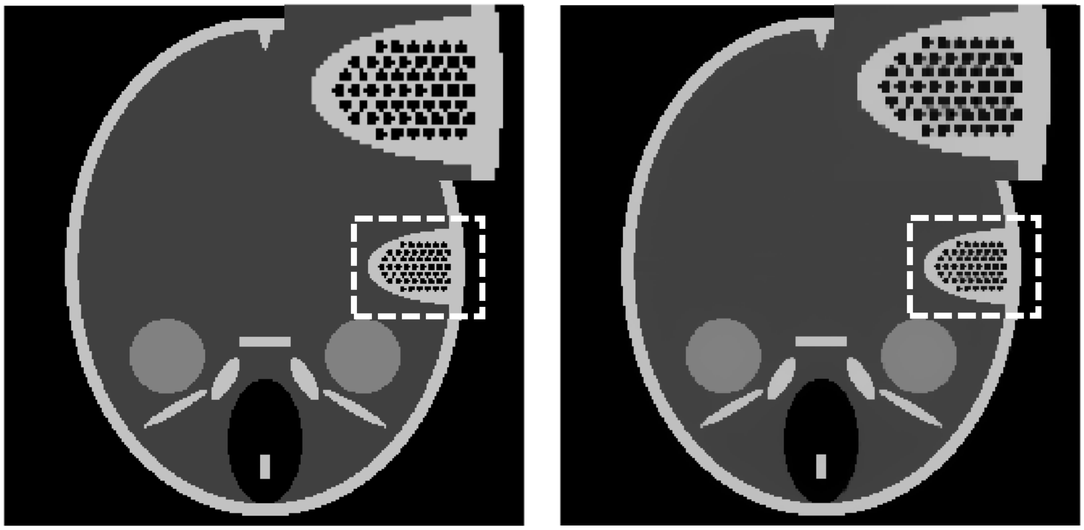

A) Ground Truth (256 × 256) B) Proposed (45 views)

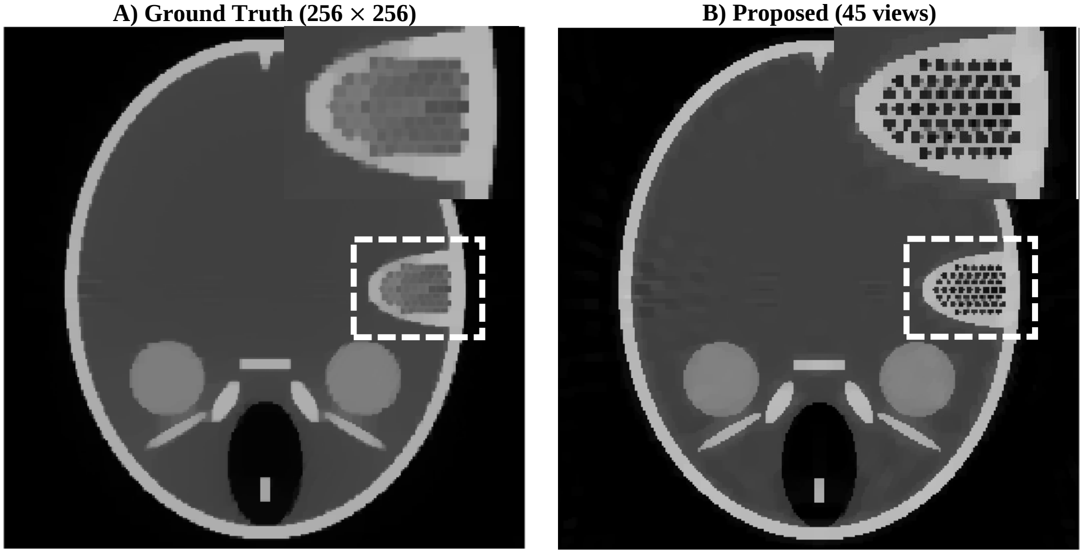

C) ASD-POCS (45 views) D) SpBR-TV (45 views)

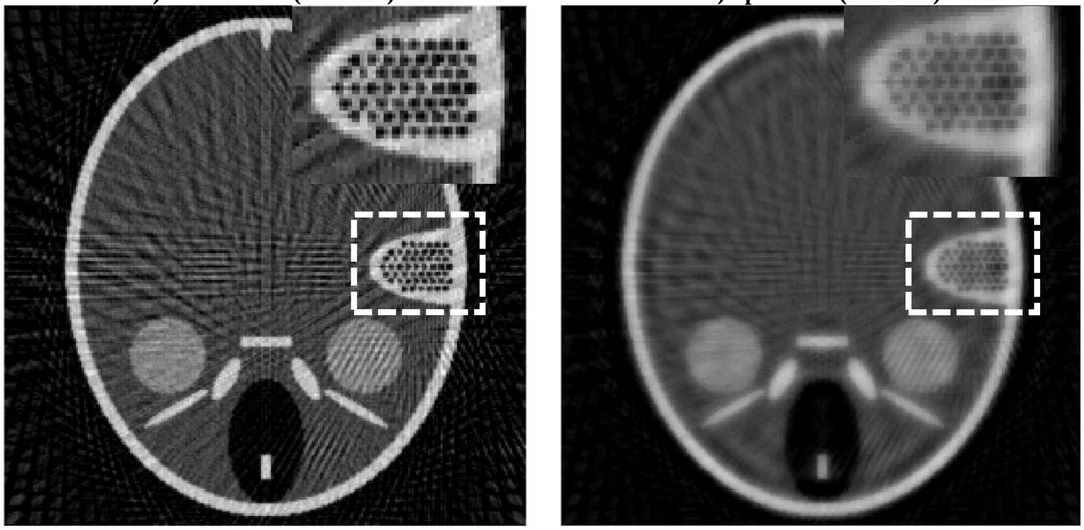

E) FBP (45 views) F) POCS (45 views)

Figure 4.3 Reconstructed Synthetic FORBILD head phantom Images using 45 views

The ASD-POCS method applies total-variation operator to preserve sharp edges and simultaneously remove aliasing artifacts without generation of undesirable effects. As illustrated in Figs. 4.5C, 4.6C and the line profiles in Figs. 4.7 and 4.8C, although, this method is successful in suppression of aliasing artifact in the smooth regions (low-resolution features), the small structures (high-resolution features) of the image such as small holes are over-smoothed which reduces the spatial resolution. The image reconstructed by the SpBR-TV method in Figs. 4.5D, 4.6D and the line profiles in Figs. 4.7 and 4.8D show that the method is successful in preserving prominent edges and at the same time suppressing aliasing artifact without generation of blurring artifact or over-smoothed image. However, this method leads to pervasive staircase effect which manifests itself as perceptually annoying artifact.

Table 4.2 Quality metrics of reconstructed femoral cortical bone image

Number of Projections	90			180			270		
Method	SSIM	PSNR (dB)	RE (%)	SSIM	PSNR (dB)	RE (%)	SSIM	PSNR (dB)	RE (%)
Proposed	0.6595	29.29	18.77	0.6739	30.74	14.69	0.7160	32.45	12.28
SpBR-TV	0.6119	27.91	21.99	0.6522	29.56	16.83	0.6929	31.32	13.99
ASD-POCS	0.5537	26.03	27.29	0.6346	28.67	18.64	0.6886	30.35	15.64
POCS	0.4979	24.76	31.6	0.5276	26.53	23.85	0.6006	28.79	18.71
FBP	0.1386	18.36	66.02	0.2533	22.11	39.67	0.3700	25.27	28.06

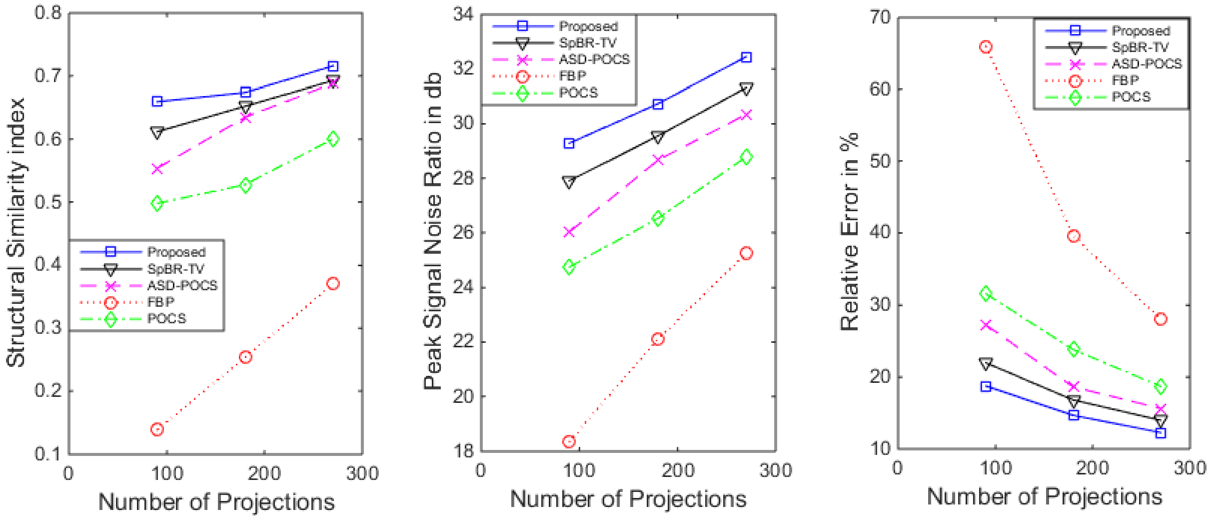

Figure 4.4 Femoral cortical bone image quality metrics vs Number of projections

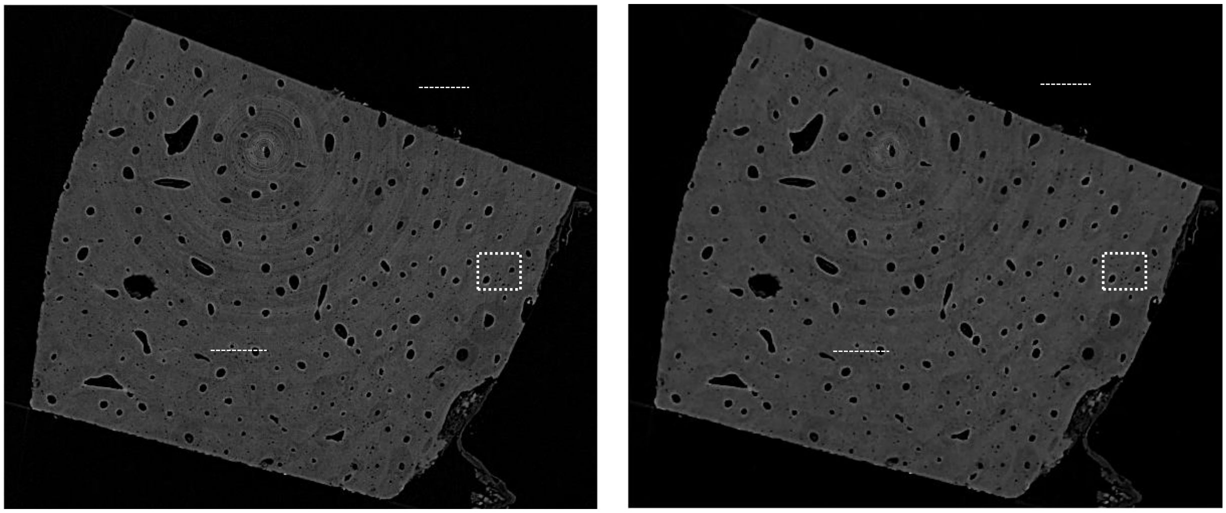

A) Reference (1800 views) **B) Proposed (270 views)**

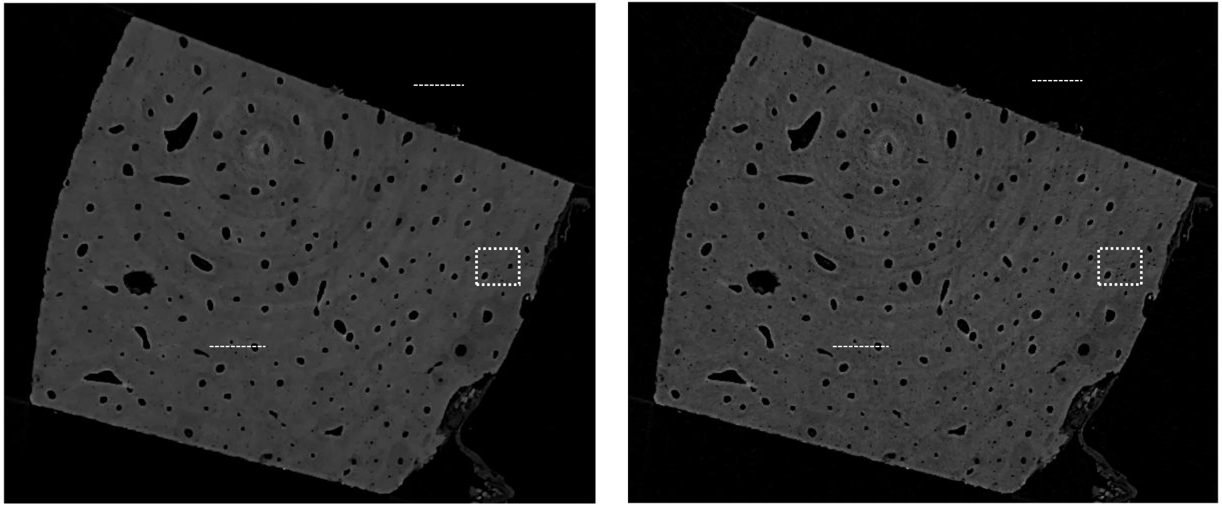

C) ASD-POCS (270 views) **D) SpBR-TV (270 views)**

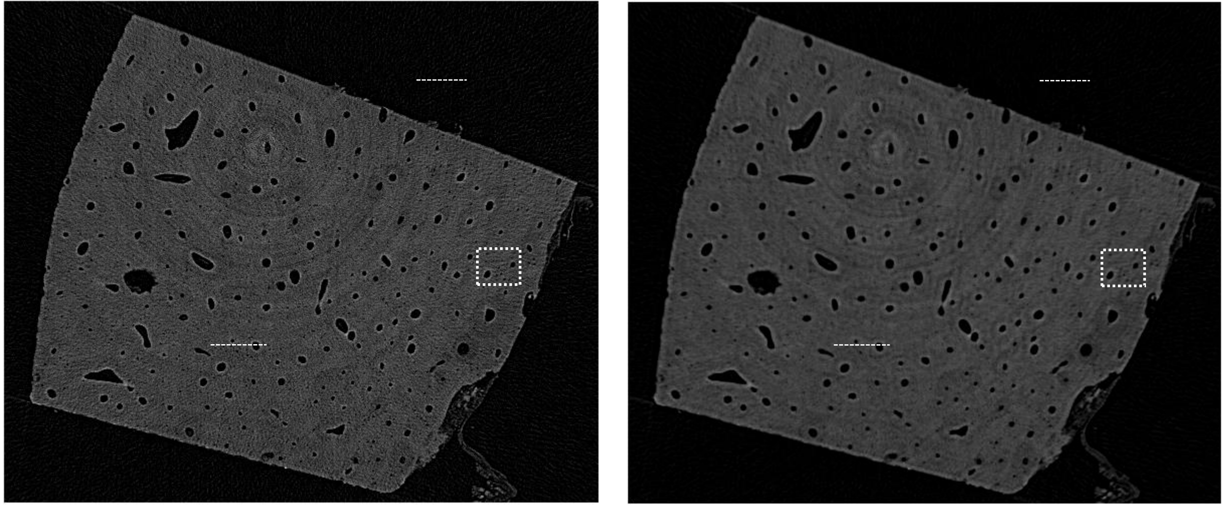

E) FBP (270 views) **F) POCS (270 views)**

Figure 4.5 The femoral cortical bone reconstructed by the different algorithms using 15% of full projection data (270 views)

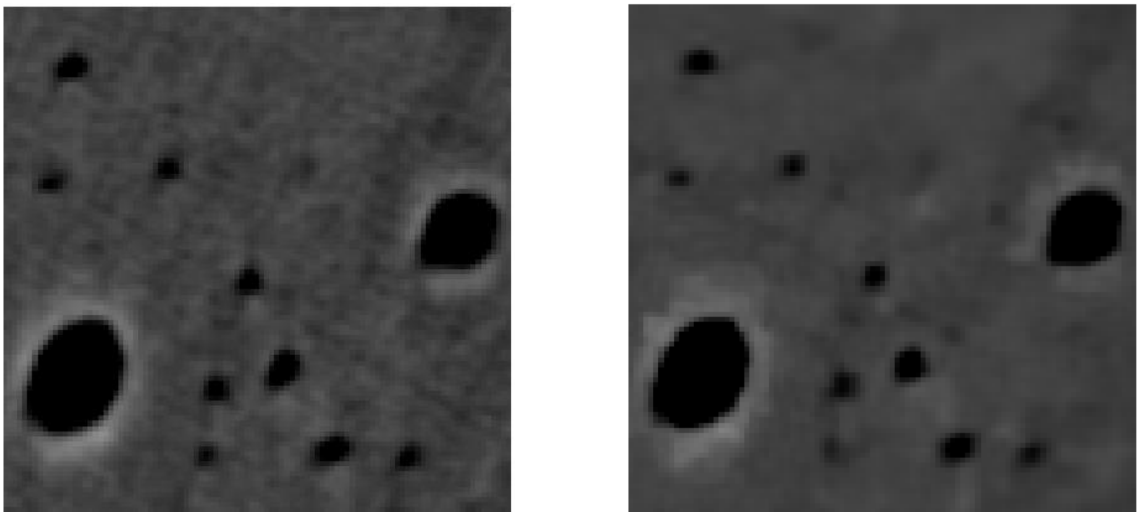

A) Reference (1800 views) B) Proposed (270 views)

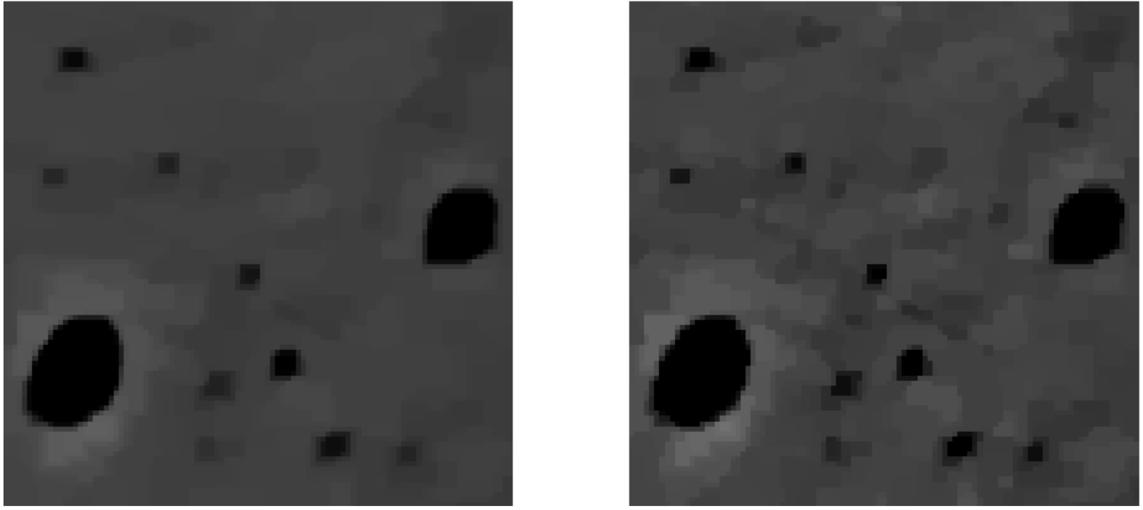

C) ASD-POCS (270 views) D) SpBR-TV (270 views)

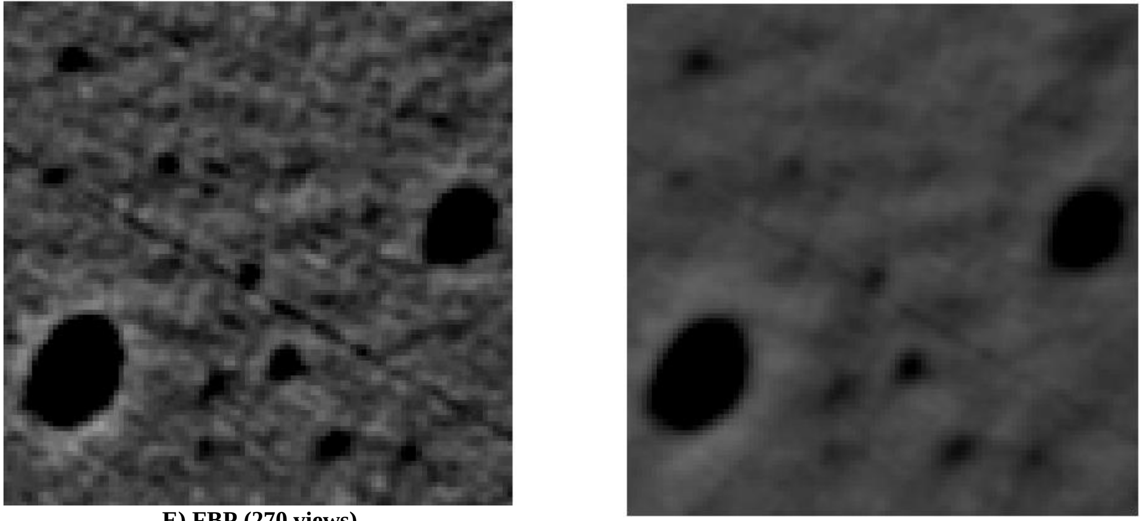

E) FBP (270 views) F) POCS (270 views)

Figure 4.6 The zoomed regions (the white dotted boxes in Fig. 4.5) in the femoral cortical bone reconstructed by the different algorithms using 15% of full projection data (270 views). The features of interest are holes (vascular canals) with different sizes

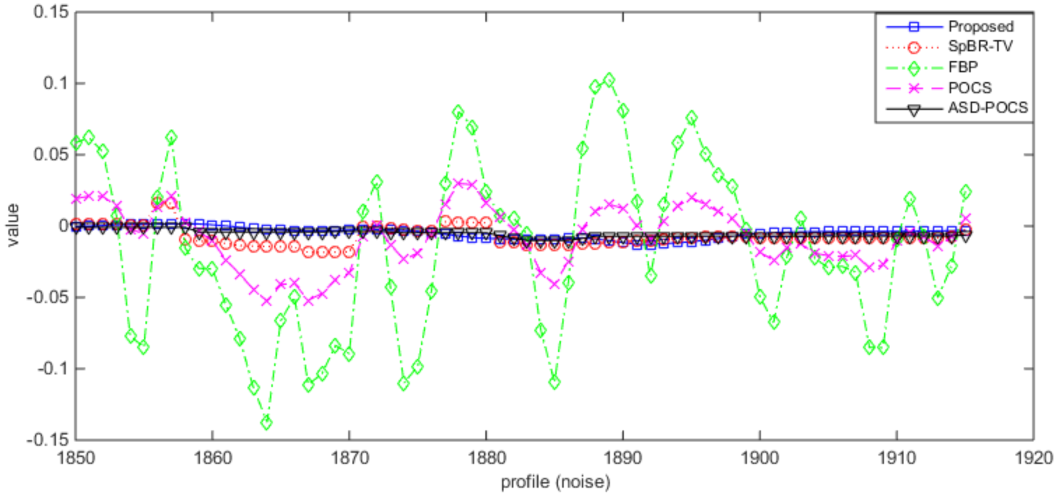

Figure 4.7 Noise profiles (the white dotted lines in Fig. 4.5) in the air that surrounds the femoral cortical bone reconstructed by different algorithms using 15% of full projection data (270 views)

Finally, as demonstrated in Figs. 4.5B, 4.6B and the line profiles in Figs. 4.7 and 4.8, the proposed algorithm is the most successful method in controlling the trade-off between aliasing artifact suppression and keeping spatial resolution. As shown in the zoomed area in Fig 4.6, the proposed algorithm reconstructed almost all the holes which are present in the reference image while suppressing the aliasing artifact without generation of any annoying distortion. As shown in Table 4.2 and Fig. 4.4, the proposed algorithm has the highest PSNR and SSIM and lowest RE with respect to the other methods even when the number of projections is only 90. From the SSIM values, one can conclude that the proposed algorithm is the best algorithm in suppressing aliasing artifacts and the PSNR and RE values indicate that the highest reconstruction accuracy can be achieved using the proposed algorithm. Moreover, Fig. 4.7 shows that the noise profiles (white dotted line in the surrounding air shown in Fig. 4.5) of the proposed algorithm and ASD-POCS method are closer to the linear attenuation coefficient of air which is zero than the other methods noise profiles. Also, Fig. 4.8 shows that the feature profile (white dotted line in the bone section shown in Fig. 4.5) of the proposed algorithm is the closest profile to the reference image feature profile. As shown in Fig. 4.6, the vascular canal (black holes) boundaries (relatively sharp contour edges) inside the rather uniform bone background which are the features of interest were accurately recovered. However, the image reconstructed by the proposed algorithm shown in Fig. 4.6B, suffer from loss of structures with low contrast boundaries. To resolve this problem, number of projections should be increased and/or the properties of the sparse regularization should be matched with the characteristics of specific samples, i.e. specific structures.

4.3.3 Parameters selection

The proposed algorithm will be successful in controlling the trade-off between artifact-suppression and spatial resolution, if the parameter λ set to a proper value. If λ is selected too low, the problem remains inconsistent, and if it is selected too high, the final image will be over smoothed. Based on our experience, the lowest reconstruction error for our datasets was obtained when approximately $\lambda = 0.1\lambda_{max}$ where λ_{max} is the critical value above which the solution of the problem is u = 0. The values of λ for bone data were chosen to be 0.1, 0.075 and 0.033 for 90, 180 and 270-view, respectively. Also, the values of λ for synthetic phantom data were chosen to be 0.021, 0.019, 0.016 and 0.012 for 15, 25, 45 and 90-view, respectively. The regularization parameter in SpBR-TV method was empirically chosen to ensure the lowest reconstruction error. The values of this parameter for bone data were chosen to be 6, 8 and 17 for 90, 180 and 270-view, respectively. Also, these values for synthetic phantom data were chosen to be 22, 27, 30 and 42 for 15, 25, 45 and 90-view, respectively. For any regularization parameter used in the SpBR-TV method, there is a corresponding ε which was used in the ASD-POCS method to ensure fair comparison between algorithms [C4.51, C4.52]. For the ASD-POCS method, the values of ε per ray measurement for bone data were chosen to be 5.25×10^{-4}, 2.18×10^{-4} and 8.49×10^{-5} for 90, 180 and 270-view, respectively. Also, the values of ε per ray measurement for synthetic phantom data were chosen to be 1.40×10^{-3}, 9.05×10^{-4}, 4.47×10^{-4} and 1.06×10^{-4} for 15, 25, 45 and 90-view, respectively.

4.3.4 Convergence Curve

The objective function of the unconstrained problem (4.4) and the objective function of the SpBR-TV method [C4.22] along with the number of iterations for the bone dataset (270 projections) were plotted in Fig. 4.9. It shows that the proposed algorithm is faster than SpBR-TV method to converge to practically acceptable accuracy that is needed for the kinds of real large-scale practical problems we consider. The value of the penalty parameter μ can change the path taken in getting to the final reconstructed image, so it is involved in determining the convergence speed.

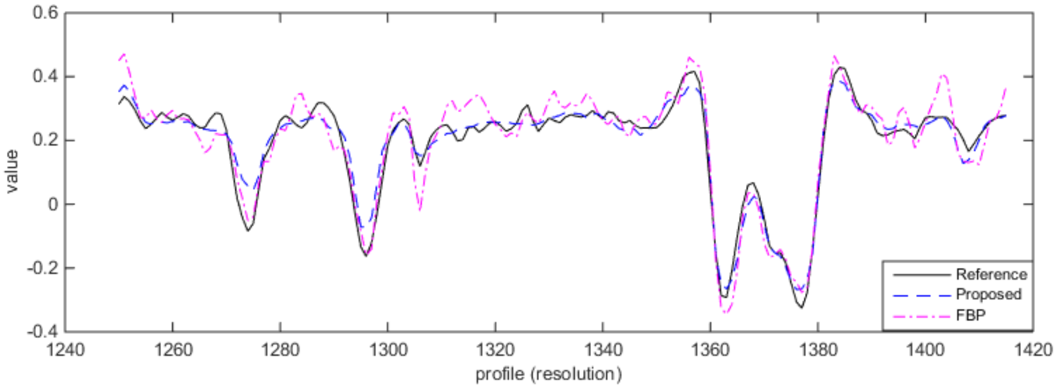

A) FBP

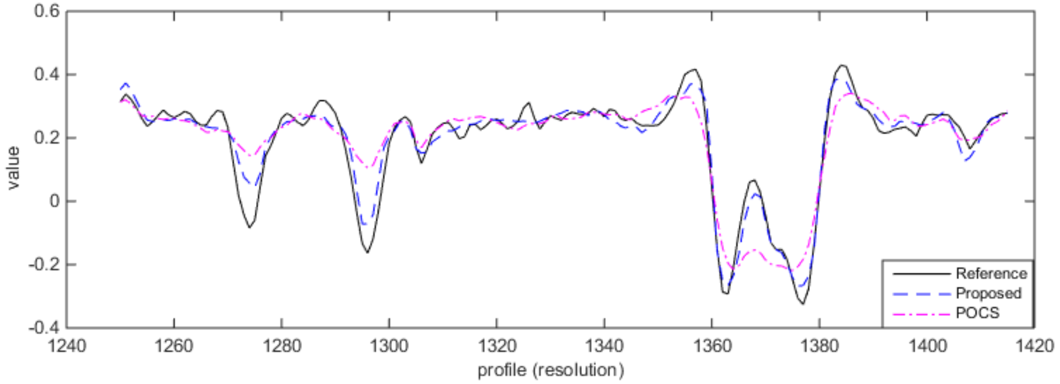

B) POCS

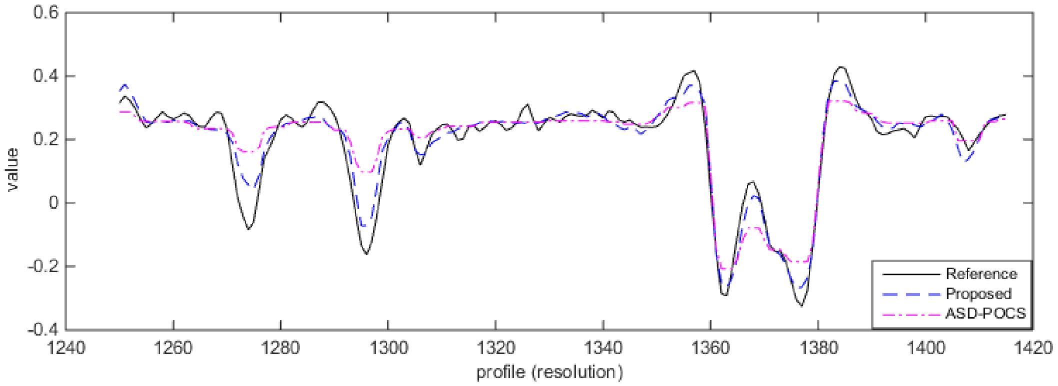

C) ASD-POCS

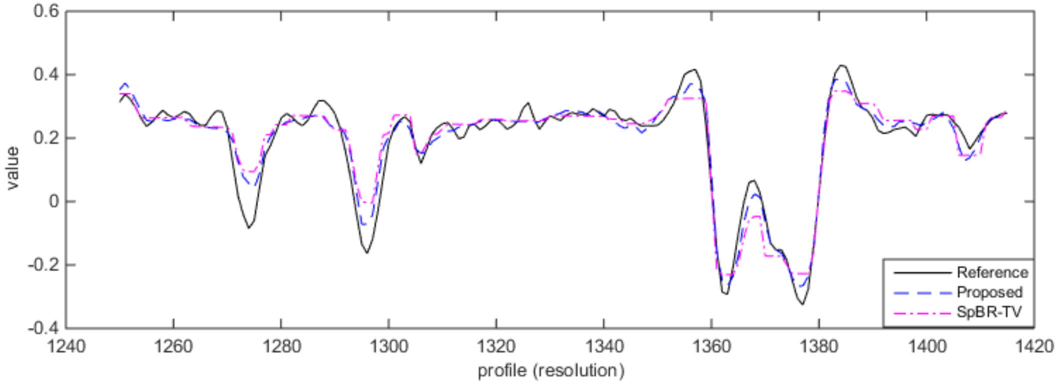

D) SpBR-TV

Figure 4.8 Feature profiles (the white dotted lines in Fig. 4.5) in the femoral cortical bone reconstructed by different algorithms using 15% of full projection data (270 views)

Based on our experience, the initial value of this parameter was set to $\mu = 0.1\lambda^{-1}$ and then we used a varying penalty parameter scheme discussed in [C4.53] to increase the convergence speed and making the performance less dependent on the initial value. The convergence speed is also affected by the number of linear CG method iterations. We suggest selecting it as small as possible, e.g., less than 10.

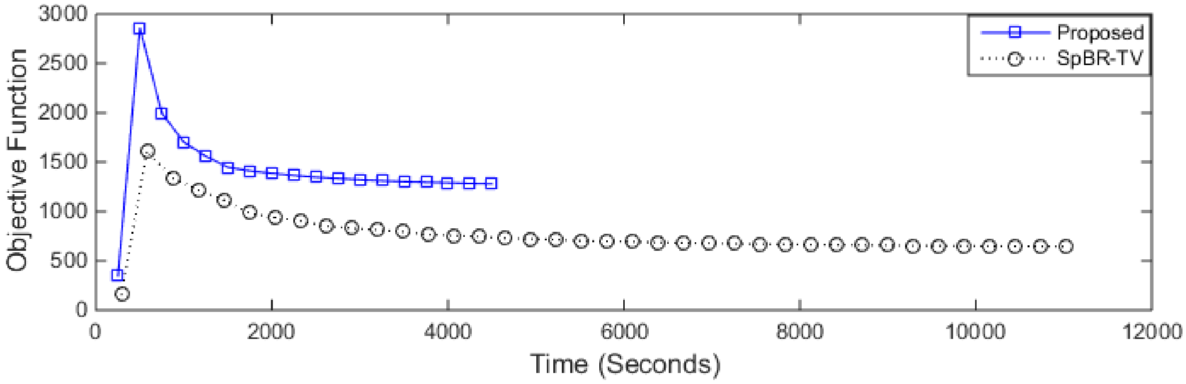

Figure 4.9 Convergence curve of the proposed and SpBR-TV algorithms for bone slice with 270 views (For better comparison, SpBR-TV objective function was multiplied by 1.5×10^{-2})

Table 4.3 Reconstruction time of the reconstruction algorithms for bone slice with 270 views

	ASD-POCS	POCS	SpBR-TV	Proposed Algorithm	FBP
Total reconstruction time (seconds)	15435	13780	11020	4560	3.75
Iteration time (seconds)	735	530	290	250	-

The proposed algorithm reconstruction time is directly proportional to the number of projections. The absolute run time of wavelet denoising algorithm for a 270-projection bone dataset is 1 minute which can be ignored because the total absolute run time of the proposed algorithm for this dataset is approximately 75 minutes. The reconstruction times of the proposed and competitive algorithms for bone slice with 270 views are shown in Table. 4.3. The reconstruction time of the proposed algorithm is almost 1200 times longer than the traditional FBP method reconstruction time. However, the proposed algorithm reconstruction time is less than the other iterative algorithms reconstruction time. As shown in Table. 4.3, the proposed algorithm needs fewer number of iterations than SpBR-TV to converge. Thus, the total reconstruction time of the proposed algorithm is less than the total reconstruction time of SpBR-TV method. Each algorithm was run until the stopping criteria i.e. relatively small change in the final image was met ($\varepsilon = 10^{-4}$).

4.4 Conclusions

In this article, we have developed and investigated a compressed sensing-based reconstruction algorithm which aims to reconstruct high-quality images from synchrotron Micro-CT datasets with potential for a significant reduction in the number of projections. The proposed algorithm which is a combination of gradient-based Douglas-Rachford Splitting and discrete wavelet packet shrinkage image denoising was applied to Micro-CT dataset collected in the Biomedical Imaging and Therapy Bending Magnet beamline at the Canadian Light Source. The algorithm solved a large-scale compressed sensing-based optimization problem to achieve an optimal balance between artifact suppression and spatial resolution. Visual and quantitative performance assessment metrics were used to show the potential advantage of the proposed algorithm to the other existing reconstruction algorithms. The results illustrated that radiation dose and scan time were reduced without reduction of image quality which is an important step towards improving in-vivo imaging protocols.

References

[C4.1] G. N. Hounsfield, "Computerized transverse axial scanning (tomography): Part 1. Description of system." The British journal of radiology 46 (552), 1016-1022 (1973).

[C4.2] L. A. Feldkamp, S. A. Goldstein, M. A. Parfitt, G. Jesion, and M. Kleerekoper, "The direct examination of three-dimensional bone architecture in vitro by computed tomography." Journal of bone and mineral research, 4 (1), 3-11 (1989).

[C4.3] L. Grodzins, "Critical absorption tomography of small samples: proposed applications of synchrotron radiation to computerized tomography II." Nuclear Instruments and Methods in Physics Research, 206 (3), 547-552 (1983).

[C4.4] P. Spanne, and M. L. Rivers, "Computerized microtomography using synchrotron radiation from the NSLS." Nuclear Instruments and Methods in Physics Research Section B: Beam Interactions with Materials and Atoms, 24, 1063-1067 (1987).

[C4.5] K. Sakamoto, Y. Suzuki, T. Hirano, and K. Usami, "Improvement of spatial resolution of monochromatic X-ray CT using synchrotron radiation." Japanese journal of applied physics. 27 (1R), 127 (1988).

[C4.6] B. F. McEwen, K. H. Downing, and R. M. Glaeser, "The relevance of dose-fractionation in tomography of radiation-sensitive specimens." Ultramicroscopy, 60 (3), 357-373 (1995).

[C4.7] T. Wysokinski, D. Chapman, G. Adams, M. Renier, P. Suortti , W. Thomlinson, "Beamlines of the biomedical imaging and therapy facility at the Canadian light source—Part 1." Nuclear Instruments and Methods in Physics Research Section A: Accelerators, Spectrometers, Detectors and Associated Equipment, 582 (1), 73-76 (2007).

[C4.8] J. Hsieh, "Computed tomography: principles, design, artifacts, and recent advances." Bellingham, WA: SPIE, 2009.

[C4.9] J. F. Barrett, and N. Keat. "Artifacts in CT: recognition and avoidance 1." Radiographics, 24 (6) 1679-1691 (2004).

[C4.10] R. Gordon, R. Bender, and G. T. Herman. "Algebraic reconstruction techniques (ART) for three-dimensional electron microscopy and X-ray photography." Journal of theoretical Biology, 29 (3), 471-481 (1970).

[C4.11] C. K. Avinash, and M. Slaney. Principles of computerized tomographic imaging. IEEE press, 1988.

[C4.12] M. Beister, D. Kolditz, and W. A. Kalender. "Iterative reconstruction methods in X-ray CT." Physica medica, 28 (2), 94-108 (2012).

[C4.13] J.S. Jørgensen, E.Y. Sidky, P.C. Hansen, X. Pan, "Empirical average-case relation between undersampling and sparsity in x-ray CT.", Inverse problems and imaging (Springfield, Mo.), 9 (2), 431 (2015).

[C4.14] J.S. Jørgensen, C Kruschel, D.A. Lorenz, "Testable uniqueness conditions for empirical assessment of undersampling levels in total variation-regularized X-ray CT". Inverse Problems in Science and Engineering, 23 (8), 1283-1305 (2015).

[C4.15] E. Y. Sidky, C. Kao, and X. Pan. "Accurate image reconstruction from few-views and limited-angle data in divergent-beam CT." Journal of X-ray Science and Technology, 14 (2), 119-139 (2006).

[C4.16] E. Y. Sidky, and X. Pan. "Image reconstruction in circular cone-beam computed tomography by constrained, total-variation minimization." Physics in medicine and biology, 53 (17), 4777 (2008).

[C4.17] X. Han, J. Bian, D. R. Eaker, T. L. Kline, E. Y. Sidky, E. L. Ritman, and X. Pan. "Algorithm-enabled low-dose micro-CT imaging." Medical Imaging, IEEE Transactions, 30 (3), 606-620 (2011).

[C4.18] C. G. Graff, and E. Y. Sidky. "Compressive sensing in medical imaging." Applied optics, 54 (8), 23-44 (2015).

[C4.19] S. Ramani, and J. A. Fessler. "An accelerated iterative reweighted least squares algorithm for compressed sensing MRI." In Biomedical Imaging: From Nano to Macro, IEEE International Symposium, 257-260 (2010).

[C4.20] A. Beck, and M. Teboulle. "A fast iterative shrinkage-thresholding algorithm for linear inverse problems." SIAM journal on imaging sciences, 2 (1), 183-202 (2009).

[C4.21] A. Beck, and M. Teboulle. "Fast gradient-based algorithms for constrained total variation image denoising and deblurring problems." Image Processing, IEEE Transactions, 18 (11), 2419-2434 (2009).

[C4.22] T. Goldstein, and S. Osher. "The split Bregman method for L1-regularized problems." SIAM Journal on Imaging Sciences, 2 (2), 323-343 (2009).

[C4.23] S. Ramani, and J. A. Fessler. "A splitting-based iterative algorithm for accelerated statistical X-ray CT reconstruction." Medical Imaging, IEEE Transactions, 31 (3), 677-688 (2012).

[C4.24] A. Chambolle, and T. Pock. "A first-order primal-dual algorithm for convex problems with applications to imaging." Journal of Mathematical Imaging and Vision, 40 (1), 120-145 (2011).

[C4.25] E. Y. Sidky, H. J. Jakob, and Xiaochuan Pan. "Convex optimization problem prototyping for image reconstruction in computed tomography with the Chambolle-Pock algorithm." Physics in medicine and biology, 57 (10), 3065 (2012).

[C4.26] E. Esser, X. Zhang, and T. F. Chan. "A general framework for a class of first order primal-dual algorithms for convex optimization in imaging science." SIAM Journal on Imaging Sciences, 3 (4), 1015-1046 (2010).

[C4.27] B. Vandeghinste, B. Goossens, J. D. Beenhouwer, A. Pizurica, W. Philips, S. Vandenberghe, and S. Staelens. "Split-Bregman-based sparse-view CT reconstruction." In 11th International meeting on Fully Three-Dimensional Image Reconstruction in Radiology and Nuclear Medicine (Fully 3D 11), 431-434. 2011.

[C4.28] L. Ritschl, F. Bergner, C. Fleischmann, and M. Kachelrieß. "Improved total variation-based CT image reconstruction applied to clinical data." Physics in medicine and biology, 56 (6), 1545 (2011).

[C4.29] J. Song, Q. H. Liu, G. A. Johnson, and C. T. Badea. "Sparseness prior based iterative image reconstruction for retrospectively gated cardiac micro-CT." Medical physics, 34 (11), 4476-4483 (2007).

[C4.30] J. Douglas, and H. H. Rachford. "On the numerical solution of heat conduction problems in two and three space variables." Transactions of the American mathematical Society, 82 (2), 421-439 (1956).

[C4.31] D. L. Donoho, I. M. Johnstone, G. Kerkyacharian, and D. Picard. "Wavelet shrinkage: asymptopia?." Journal of the Royal Statistical Society. Series B (Methodological), 301-369 (1995).

[C4.32] J. Zhong, R. Ning, and D. Conover. "Image denoising based on multiscale singularity detection for cone beam CT breast imaging." Medical Imaging, IEEE Transactions, 23 (6), 696-703 (2004).

[C4.33] A. Fathi, and A. R. Naghsh-Nilchi. "Efficient image denoising method based on a new adaptive wavelet packet thresholding function." Image Processing, IEEE Transactions, 21 (9), 3981-3990 (2012).

[C4.34] B. Wolkowski, E. Snead, M. Wesolowski, J. Singh, M. Pettitt, R. Chibbar, S. A. Melli, and J. Montgomery. "Assessment of freeware programs for the reconstruction of tomography datasets obtained with a monochromatic synchrotron-based X-ray source." Journal of synchrotron radiation, 22 (4), 1130-1138 (2015).

[C4.35] E. Walters, W. Simon, D. A. Chesler, and J. A. Correia, "Attenuation correction in gamma emission computed tomography," J. Comp. Assist. Tomogr. 5, 89-94 (1981).

[C4.36] X.L. Xu, J.S. Liaw, and S. C. Strother, "Iterative algebraic reconstruction algorithms for emission computed tomography," Med. Phys. 20, 1675-1684 (1993).

[C4.37] G. L. Zeng, and G. T. Gullberg. "Unmatched projector/backprojector pairs in an iterative reconstruction algorithm." Medical Imaging, IEEE Transactions, 19 (5), 548-555 (2000).

[C4.38] C. L. Epstein. "Introduction to the Mathematics of Medical Imaging.", Prentice Hall, Upper Saddle River, N.J., 2003.

[C4.39] D. S. Lalush and B. M.W. Tsui, “Improving the convergence of iterative filtered backprojection algorithm,” Med. Phys., 21, 1283-1286 (1994).

[C4.40] S. S. Chen, D. L. Donoho, and M. A. Saunders. "Atomic decomposition by basis pursuit." SIAM review 43 (1), 129-159 (2001).

[C4.41] R. Tibshirani, "Regression shrinkage and selection via the lasso", Journal of the Royal Statistical Society, Series B, 58, 267–288 (1996).

[C4.42] D. P. Bertsekas, Constrained optimization and Lagrange multiplier methods. Academic press, 2014.

[C4.43] J. Eckstein and D. P. Bertsekas. "On the Douglas—Rachford splitting method and the proximal point algorithm for maximal monotone operators." Mathematical Programming, 55 (1-3), 293-318 (1992).

[C4.44] N. Parikh, and S. P. Boyd. "Proximal Algorithms." Foundations and Trends in optimization, 1 (3), 127-239 (2014).

[C4.45] M. R. Hestenes and E Stiefel. Methods of conjugate gradients for solving linear systems. 49, 1952.

[C4.46] M. Lustig, D. Donoho, and J. M. Pauly. "Sparse MRI: The application of compressed sensing for rapid MR imaging." Magnetic resonance in medicine, 58 (6), 1182-1195 (2007).

[C4.47] A. M. Altaher, and M. T. Ismail. "A comparison of some thresholding selection methods for wavelet regression." World Academy of Science, Engineering and Technology, 62 (1), 119-125 (2010).

[C4.48] S. Boyd, N. Parikh, E. Chu, B. Peleato, and J. Eckstein. "Distributed optimization and statistical learning via the alternating direction method of multipliers." Foundations and Trends® in Machine Learning, 3 (1), 1-122 (2011).

[C4.49] Z. Wang, A. C. Bovik, H. R. Sheikh, and E. P. Simoncelli. "Image quality assessment: from error visibility to structural similarity." Image Processing, IEEE Transactions, 13 (4), 600-612 (2004).

[C4.50] http://www.imp.uni-erlangen.de/phantoms.

[C4.51] R. T. Rockafellar, Convex analysis. Princeton university press, 2015.

[C4.52] J. Bian, J.H. Siewerdsen, X. Han, E.Y. Sidky, J.L. Prince, C.A. Pelizzari, X. Pan. “Evaluation of sparse-view reconstruction from flat-panel-detector cone-beam CT”, Physics in medicine and biology, 55(22), 6575 (2010).

[C4.53] S. L. Wang and L. Z. Liao, "Decomposition method with a variable parameter for a class of monotone variational inequality problems," Journal of Optimization Theory and Applications, 109 (2), 415-429 (2001).

5. A Compressed Sensing Algorithm for Reduced-view Image Reconstruction from Real In-vivo Synchrotron Phase Contrast CT Bone Data

Published as: Melli, S. Ali, Khan A. Wahid, Paul Babyn, David ML Cooper, and Ahmed M. Hasan. "A wavelet gradient sparsity-based algorithm for reconstruction of reduced-view tomography datasets obtained with a monochromatic synchrotron-based X-ray source." Computerized Medical Imaging and Graphics 69 (2018): 69-81.

In the previous chapter, a compressed sensing algorithm was proposed for reduced-view image reconstruction from real ex-vivo synchrotron absorption contrast micro-CT bone data.

The manuscript included in this chapter proposes a compressed sensing algorithm for reduced-view image reconstruction from real in-vivo synchrotron phase contrast CT bone data. The goal is to reduce the radiation dose and scan time by reducing the number of projections. The in-vivo phase contrast projection dataset used in this chapter is noisier than the absorption contrast micro-CT projection dataset used for the ex-vivo study proposed in the previous chapter. Furthermore, the number of acquired projections and the radiation exposure time per projection are less than the values set for the ex-vivo study. A multi-regularization constraint compressed sensing algorithm is proposed in this chapter to enforce consistency with the highly reduced-view and noisy projection data and at the same time attenuating the aliasing, staircase and ringing artifacts while preserving piecewise smooth regions with sharp edges, point singularities, and textures. Visual and quantitative-based performance assessments of reconstructed slices of a rat forelimb sample demonstrate the advantage of the proposed algorithm compared to other existing algorithms.

The student (first author) designed the algorithm, processed the raw data, performed the numerical simulation, interpreted the results, designed the figures and wrote the manuscript. K. A. Wahid and, P. Babyn provided equal supervision effort. David ML Cooper was involved in collection of synchrotron data at the Canadian Light Source, including the methods used to collect the data and the technical analyses supporting the quality of the measurements.

A wavelet gradient sparsity-based algorithm for reconstruction of reduced-view tomography datasets obtained with a monochromatic synchrotron-based X-ray source

S. Ali Melli, Khan A. Wahid, Paul Babyn, David M.L. Cooper, Ahmed M. Hasan

Abstract

High-resolution synchrotron computed tomography (CT) is very helpful in the diagnosis and monitor of chronic diseases including osteoporosis. Osteoporosis is characterized by low bone mass and cortical bone porosity best imaged with CT. Synchrotron CT requires a large number of angular projections to reconstruct images with high resolution for detailed and accurate diagnosis. However, this poses great risks and challenges for serial in-vivo human and animal imaging due to a large amount of x-ray radiation dose required that can damage living specimens. Also, longer scan times are associated with increased risk of specimen movement and motion artifact in the reconstructed images. We developed a wavelet-gradient sparsity-based algorithm to be utilized as a synchrotron tomography reconstruction technique allowing accurate reconstruction of cortical bone porosity assessed for in-vivo preclinical study which significantly reduces the radiation dose and scan time required while maintaining satisfactory image resolution for diagnosis. The results of our study on a rat forelimb sample imaged in the Biomedical Imaging and Therapy Bending Magnet (BMIT-BM) beamline at the Canadian Light Source show that the proposed algorithm can produce satisfactory image quality with more than 50 percent x-ray dose reduction as indicated by both visual and quantitative-based performance.

Index terms

reduced-view computed tomography reconstruction; x-ray dose reduction in high-resolution imaging of bone microstructure; reduction of in-vivo synchrotron-based x-ray source computed tomography scan time

5.1 Introduction

Synchrotron X-ray Computed Tomography (CT) is an imaging technique which is progressively used for non-invasive in-vivo preclinical imaging [C5.1]. The benefit of synchrotron CT over conventional CT scanner is that x-rays generated at synchrotron beamline are almost parallel and monochromatic in a pre-selectable energy which eliminate cone beam and beam-hardening artifacts, respectively. Also, synchrotron x-rays are highly intense which boosts the signal to noise ratio in a much shorter scan time [C5.2, C5.3]. These benefits make this imaging method an important non-invasive inspection tool for the biological research.

There are several experimental setups available to generate x-ray images. Among them, propagation-based phase contrast CT has a simple setup with high spatial resolution (a few tens of microns). Some encouraging results have been reported for the application of this technique in clinical experiments [C5.4]. Propagation-based phase contrast CT techniques have been developed with synchrotrons sources as they provide spatially coherent high brilliance radiation [C5.5, C5.6, C5.7]. The experimental setup of this synchrotron-based technique is like the setup used in radiography i.e. synchrotron x-ray source, the sample and the detector are inline, without any optical element between the sample and the detector. Instead of placing the detector directly behind the sample, which is convenient in radiography, it is placed in some distance from the sample. As a result, the x-rays that are refracted by different tissues due to different refractive indices inside the sample can interfere with unaffected beam on the detector [C5.8]. The phase contrast image formed in the detector is sensitive to abrupt variations of refractive indices; so the structural boundaries between different tissues inside the sample are enhanced in this technique [C5.9].

Traditionally, synchrotron tomographic reconstruction techniques require a large number of projection views to reconstruct images with a sufficed spatial resolution to view as much detail as possible in the sample field of view [C5.10, C5.11]. This exposes the specimen to a large amount of x-ray radiation which can damage living specimens. Furthermore, this increases scan time and consequently the likelihood of involuntary specimen movements so the formation of motion artifact in the reconstructed images will be more likely.

Currently, the standard reconstruction method in synchrotron CT is the Filtered Back Projection (FBP) algorithm, which requires a large number of projections for yielding accurate reconstruction, otherwise, aliasing artifacts will occur in the reconstructed image. However, there are situations where it is not possible or undesirable to measure a large number of projections. Problems of this type may be amenable to solution by algebraic techniques [C5.12]. For the case where the data are consistent yet are not sufficient to determine a unique solution, the algebraic algorithm such as Projection Onto Convex Sets (POCS) [C5.13] finds the image that is consistent with the data and minimizes the sum-of-squares of the image pixel values. However, because of modeling errors and noise which is inevitable in real data, the inconsistency in linear CT projection equation is almost impossible to avoid [C5.14].

Compressed sensing (CS) is a nonlinear reconstruction paradigm that has been shown of value to successfully reconstruct undersampled datasets using nonlinear image-reconstruction algorithms, provided that the images have a sparse representation in one or more domains. Progress in CS theory has intensified research to develop fast-convergent solvers for the large-scale CT reconstruction problems which are required in practice. Therefore, a CS- based algorithm called ASD-POCS was proposed in [C5.15, C5.16] to minimize the Total Variation (TV) of the image subject to the constraint that the estimated projection data is within a specified tolerance of the available data and that the values of the volume image are not negative. A comprehensive study using ASD-POCS for reduced-view reconstruction of real CT data was carried out in [C5.17]. Also, in [C5.18], the application of this algorithm in low-dose micro-CT of real animal organs was investigated. The results show that the ASD-POCS algorithm using only one-sixth to one-quarter of the conventional 360-view data can reconstruct images with comparable quality to that obtained with conventional algorithms. However, the problem with this heuristic algorithm is that the final image depends on algorithm parameters [C5.14]. To solve this problem, in the past few years, state-of-the-art first-order splitting based algorithms such as FISTA [C5.19], and Split-Bregman-type (SB) schemes [C5.20] which can handle non-smooth regularizers such as $l1$-norm have been proposed to eliminate the need to study the dependence of the final image on algorithm parameters. The Split-Bregman (SB) method converges to a reasonable precision very fast [C5.21] and has been used in reduced-view CT reconstruction algorithm [C5.22]. Although TV-based reconstruction algorithms such as SpBR-TV (Split Bregman - Total Variation) have been shown to work well when dealing with piecewise smooth images [C5.22], it may lead to unwanted staircase artifact when applied to images that contain textures and shading [C5.23, C5.24]. In contrast, 2D wavelet transform is good at capturing point singularities and small patches [C5.25], thus preserving fine structures, but not as good for approximating piecewise smooth regions because it penalizes jumps and cause oscillations around edges known as Pseudo-Gibbs Phenomena [C5.26, C5.27]. Consequently, the currently proposed algorithm is based on combining gradient and wavelet transformation to remove the staircase and oscillations artifacts while preserving piecewise smooth regions with sharp edges and point singularities. Also, Prior Image Constrained Compressed Sensing (PICCS) reconstruction framework was proposed in [C5.28] to apply CS to CT imaging when we need a highly reduced-view reconstruction. PICCS aims to take advantage of a prior image to promote sparsity of target image. More recent applications of PICCS framework have focused on using it to reduce CT dose [C5.29, C5.30]. For these applications, a prior image is formed by spatially low-pass filtering of FBP image to generate a low-noise low-spatial resolution prior image.

This research is focused on proposing a wavelet-gradient sparsity based prior image constrained compressed sensing algorithm to be used as a synchrotron tomography reconstruction technique. The PICCS framework, which is based on a low noise, low-spatial resolution prior image enforces consistency with the projection data to recover spatial resolution. At the same time, it suppresses the unwanted artifacts by using the combination of gradient and wavelet transformation. The Douglas-Rachford Splitting (DRS) method [C5.31] was used to minimize the optimization problem. This method is powerful for solving non-smooth, constrained, large-scale problems as is the case here. The DRS method can coordinate the solutions of small-scale and easy-to-solve sub-problems to find the solution of a large-scale optimization problem.

5.2 Material and Methods

5.2.1 Synchrotron CT data acquisition

CT data were obtained from the Biomedical Imaging and Therapy Bending Magnet (BMIT-BM) Beamline at the Canadian Light Source (CLS). The target was a rat forelimb (including the radius and ulna bones) which was placed on a rotating mechanical stage that was 26 m away from the synchrotron source so that the X-ray beam can be assumed to be parallel. Projection data were collected with a C4742-95 – 12HR (Hamamatsu) camera which includes a C4742-56 – 12HR CCD Detector. It provides an effective pixel size of 13 μm. The sample was rotated continuously with a rotation velocity of 0.20 degree/sec through 0 to 180°, generating 750 projections (matrix of 4000×104 pixels). The total amount of measured x-ray surface dose was 2.98 Gy. Dark and flat projections were taken before and after the sequential angular projections. The acquisition system used 12-bit TIFF grey scale digital format to save the calibration and tomographic data.

5.2.2 Synchrotron CT data preprocessing

Projection data required preprocessing before sinogram formation, including dark and flat field correction, projection alignment, beam power normalization and logarithmic transformation. Dark and flat field correction compensates the spatial variation in beam intensity caused by different detector pixel sensitivities and distortions in the optical path and it also compensates different dark currents in detector pixels so that a uniform signal creates a uniform output. Projection alignment was needed because it is practically difficult to exactly match specimen rotation center with the center of the projection images and finally beam power normalization was used to compensate the slight variations in the beam intensity happening over time. After logarithmic transformation, preprocessed projections under different angles along the 180° angular range are organized side by side in 2D projection plane to form sinogram. Ring artifacts created by defective pixels on the detector or a small variation in filtered beam were removed from sinogram datasets before the application of the reconstruction algorithms [C5.1]. The flat field image, the dark field image, the projected image before pre-processing, the projected image after pre-processing and the sinogram after ring removal (750 views) were shown in Fig. 5.1.

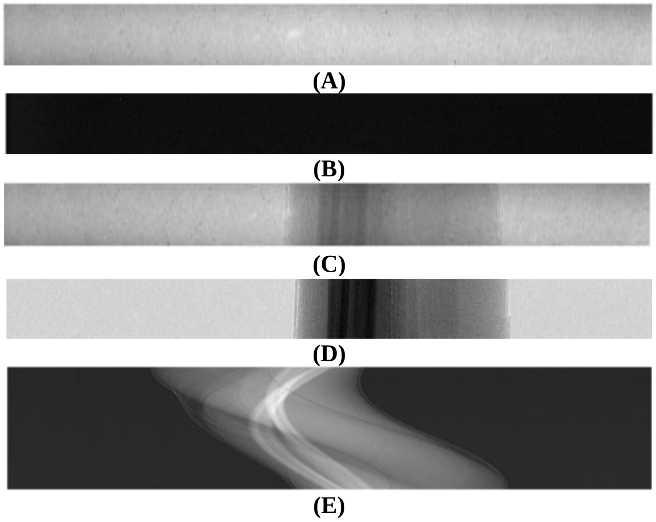

Figure 5.1 (A and B) Flat and Dark field images, (C) Projected image before pre-processing, (D) Projected image after pre-processing, (E) Sinogram after ring removal (750 views)

5.2.3 Imaging model and optimization formulation

The basic algebraic imaging model for a 2D synchrotron x-ray Micro-CT is:

$$y = Au + n \tag{5.1}$$

Where $u \in R^N$ is a vector of image pixel values modeling spatially varying linear attenuation coefficient, $A \in R^{M \times N}$is the discrete radon transform [C5.12] modeling the parallel forward projection operator which yields noisy undersampled ($M < N$) sinogram dataset $y \in R^M$ and n represents zero mean additive white Gaussian noise model. As discussed in [C5.32, C5.33], both sides of Eq. (5.1) can be multiplied by the FBP operator to form an equivalent preconditioned Eq. (5.2). The eigenvalues of square matrix FA which is diagonally dominant with positive diagonal elements are positive and clustered closer together than the eigenvalues of square matrix $A^T A$ [C5.32].

$$Fy = FAu, \quad F = A^T R \tag{5.2}$$

The superscript T represents the transpose operation, A^T is the discrete counterpart of the adjoint of the radon transform modeling the parallel back-projection operator and R is the discrete counterpart of 1D convolution operator (band-limited ramp filter kernel) which is defined in the discrete inverse radon transform [C5.34]. To view this as an optimization problem, we must find a generalized squared-error function that is minimized by the solution u given by Eq. (5.2) [C5.33]:

$$\frac{1}{2}\|Au - y\|_R^2 = \frac{1}{2}(Au - y)^T R (Au - y) \tag{5.3}$$

Taking the derivative of Eq. (5.3) with respect to u and putting it equal to zero yields Eq. (5.2).

According to the compressed sensing theory, an optimization problem called Basis Pursuit DeNoising (BPDN) is formed to search a prior image constrained wavelet - gradient sparse image, subject to a relaxed data constraint as follows [C5.35]:

$$\min_u \quad \left\|G(u - u_p)\right\|_{l_1} + \alpha_1 \|Gu\|_{l_1} + \alpha_2 \|Wu\|_{l_1} \quad S.T. \quad \frac{1}{2}\|Au - y\|_R^2 < \varepsilon \tag{5.4}$$

Where u_p is the low noise low spatial resolution prior image obtained by filtering FBP reconstructed image with a 2D rotationally symmetric Gaussian smoothing kernel of size [3, 3] with standard deviation of 1. The difference image $u - u_p$ contains two main high spatial frequency signals: edges and noise. Since noise is not inherently sparse, it is minimized preferably in the reconstructed image [C5.28, C5.29]. $\frac{1}{2}\|Au-y\|_R^2$ is used to enforce consistency with the projection data in order to recover spatial resolution. $G \in R^{N\times 2N}$ is the 2D first-order anisotropic gradient operator defined in Eq. (5.5), $W \in R^{N\times N}$consists of 2D fourth order Daubechies wavelets (db4) with four levels of decomposition which are orthogonal basis of wavelets characterized by a maximal number of vanishing moments [C5.36]. Using the combination of gradient and wavelet transformation suppresses the aliasing artifacts caused by insufficient number of the projections. $\|x\|_{l_1}$is the ℓ1-norm to encourage sparsity, α_1, α_2> 0 are parameters controlling the relative strengths of the sparsity constraints and ε is the parameter which controls the trade-off between spatial resolution and the suppression of artifacts/noise.

$$\|Gu\|_{l_1} := \sum_{i,j}\left|u_{i+1,j}-u_{i,j}\right| + \left|u_{i,j+1}-u_{i,j}\right| \tag{5.5}$$

5.2.4 Proposed Reconstruction Algorithm

The constrained BPDN problem (5.4) is changed to an equivalent unconstrained problem (5.6), by adding the ℓ1-norm of the gradient and wavelet operators to the data fidelity term.

$$\min_{u\in R^n} \; \frac{1}{2}\|Au-y\|_R^2 + \alpha_3\left(\left\|G(u-u_p)\right\|_{l_1} + \alpha_1\|Gu\|_{l_1} + \alpha_2\|Wu\|_{l_1}\right) \tag{5.6}$$

For any ε, a solution of problem (5.4) is a null vector or a minimizer of problem (5.6) for a corresponding $\alpha_3 > 0$ [C5.37]. Our approach to solve the optimization problem (5.6) is to convert it into an equivalent constrained optimization problem.

$$\min_{u,v} \; \frac{1}{2}\|Au-y\|_R^2 + \lambda_1\|v^1\|_{l_1} + \lambda_2\|v^2\|_{l_1} + \lambda_3\|v^3\|_{l_1}$$

$$S.T. \quad v^1 = G(u-u_p), \quad v^2 = Gu, \quad v^3 = Wu \tag{5.7}$$

Where $\lambda_1 = \alpha_3$, $\lambda_2 = \alpha_3\alpha_1$, $\lambda_3 = \alpha_3\alpha_2$. The global minima of a convex function subject to equality constraint can be found by forming an unconstrained optimization problem followed by a dual variable update as follows [C5.38]:

Initialize $\lambda_1, \lambda_2, \lambda_3, \mu_1 = \frac{0.1}{\lambda_1}, \mu_2 = \frac{0.1}{\lambda_2}, \mu_3 = \frac{0.1}{\lambda_3}, u = 0, v^1, v^2, v^3 = 0, b^1, b^2, b^3 = 0$

Loop

$$\min_{u,v^1,v^2,v^3} \quad \frac{1}{2}\|Au - y\|_R^2 + \lambda_1\|v^1\|_{l_1} + \lambda_2\|v^2\|_{l_1} + \lambda_3\|v^3\|_{l_1} + {b^1}^T\left(G(u - u_p) - v^1\right)$$

$$+\frac{1}{2\mu_1}\left\|G\left(u - u_p\right) - v^1\right\|_{l_2}^2 + {b^2}^T\left(Gu - v^2\right) + \frac{1}{2\mu_2}\|Gu - v^2\|_{l_2}^2 + {b^3}^T\left(Wu - v^3\right)$$

$$+\frac{1}{2\mu_3}\|Wu - v^3\|_{l_2}^2 \tag{5.8}$$

$$d^1 := d^1 + \left(G(u - u_p) - v^1\right), d^1 = \mu_1 b^1 \tag{5.9}$$

$$d^2 := d^2 + \left(Gu - v^2\right), d^2 = \mu_2 b^2 \tag{5.10}$$

$$d^3 := d^3 + \left(Wu - v^3\right), d^3 = \mu_3 b^3 \tag{5.11}$$

Until stop condition is satisfied

Where $b^1 \in R^{2N}, b^2 \in R^{2N}, b^3 \in R^N$ are the vectors of dual variables and $\mu_1, \mu_2, \mu_3 > 0$ are called the penalty parameters. The benefit of including the quadratic penalty term is to bring robustness which means better handling of ill-conditioned functions.

The optimization problem (5.8) is rewritten in a new form Eq. (5.12) by merging the linear and quadratic functions:

$$\min_{u,v^1,v^2,v^3} \quad \frac{1}{2}\|Au - y\|_R^2 + \lambda_1\|v^1\|_{l_1} + \lambda_2\|v^2\|_{l_1} + \lambda_3\|v^3\|_{l_1} + \frac{1}{2\mu_1}\left\|G(u - u_p) - v^1 + d^1\right\|_{l_2}^2 +$$

$$\frac{1}{2\mu_2}\|Gu - v^2 + d^2\|_{l_2}^2 + \frac{1}{2\mu_3}\|Wu - v^3 + d^3\|_{l_2}^2 \tag{5.12}$$

The optimization problem in Eq. (5.12) is solved by applying the Douglas-Rachford Splitting (DRS) algorithm [C5.39]. This algorithm is helpful where optimization problems with respect to u, v^1, $v^2$and v^3 (Eqs. (5.13), (5.14), (5.15) and Eq. (5.16)) are efficiently solved while the joint minimization of Eq. (5.12) is difficult to evaluate. For that reason, Eq. (5.12) is decomposed into sub-optimization problems by separately minimizing with respect to u, v^1, $v^2$and v^3.

$$u := \min_{u} \quad \frac{1}{2}\|Au - y\|_R^2 + \frac{1}{2\mu_1}\left\|G(u - u_p) - (v^1 - d^1)\right\|_{l_2}^2 + \frac{1}{2\mu_2}\|Gu - (v^2 - d^2)\|_{l_2}^2 + \frac{1}{2\mu_3}\|Wu - (v^3 - d^3)\|_{l_2}^2 \tag{5.13}$$

$$v^1 := \min_{v^1} \quad \lambda_1\|v^1\|_{l_1} + \frac{1}{2\mu_1}\left\|v^1 - (G(u - u_p) + d^1)\right\|_{l_2}^2 \tag{5.14}$$

$$v^2 := \min_{v^2} \quad \lambda_2\|v^2\|_{l_1} + \frac{1}{2\mu_2}\|v^2 - (Gu + d^2)\|_{l_2}^2 \tag{5.15}$$

$$v^3 := \min_{v^3} \quad \lambda_3\|v^3\|_{l_1} + \frac{1}{2\mu_3}\|v^3 - (Wu + d^3)\|_{l_2}^2 \tag{5.16}$$

The convergence analysis of the DRS algorithm was discussed in [C5.39]. It shows that it is not necessary to exactly solve the sub-optimization problems. Global convergence will be guaranteed, provided that the sequence of errors is absolutely summable. Depending on the functions used in the sub-optimization problems, gradient method can be used to find the iterative or closed form formulations to update u and v^1, v^2, v^3 efficiently.

The next step is to minimize the convex quadratic function in Eq. (5.13). This is a least square minimization problem and the solution is a normal equation as follows [C5.37]:

$$u := (A^TRA + \frac{1}{\mu_1}G^TG + \frac{1}{\mu_2}G^TG + \frac{1}{\mu_3}W^TW)^{-1}(A^TRy + \frac{1}{\mu_1}G^TGu_p + \frac{1}{\mu_1}G^T(v^1 - d^1) + \frac{1}{\mu_2}G^T(v^2 - d^2) + \frac{1}{\mu_3}W^T(v^3 - d^3)) \tag{5.17}$$

Eq. (5.17) is a system of linear equations with the coefficient matrix $(A^TRA + \frac{1}{\mu_1}G^TG + \frac{1}{\mu_2}G^TG + \frac{1}{\mu_3}W^TW)$ and the right hand matrix $(A^TRy + \frac{1}{\mu_1}G^TGu_p + \frac{1}{\mu_1}G^T(v^1 - d^1) + \frac{1}{\mu_2}G^T(v^2 - d^2) + \frac{1}{\mu_3}W^T(v^3 - d^3))$. The linear Conjugate Gradient (CG) method [C5.40] is used to approximately solve Eq. (5.17). The advantage of this method is that it can solve large-scale linear equations without a need to explicitly inverse the coefficient matrix.

Sub differential calculus can be used to find a closed form formula as a solution for the optimization problems in Eqs. (5.14, 5.15 and 5.16). After doing some basic mathematical operations, Eqs. (5.18, 5.19 and 5.20) are derived. These solutions are based on shrinkage soft threshold operator [C5.41]:

$$v^1 := \quad ST_{\mu_1\lambda_1}(G(u-u_p)+d^1) \tag{5.18}$$

$$v^2 := \quad ST_{\mu_2\lambda_2}(Gu+d^2) \tag{5.19}$$

$$v^3 := \quad ST_{\mu_3\lambda_3}(Wu+d^3) \tag{5.20}$$

Where the soft threshold operator is defined as below [C5.42]:

$$ST_\kappa(a) = \begin{cases} a-\kappa & a > \kappa \\ 0 & |a| \le k \\ a+\kappa & a < -k \end{cases} \tag{5.21}$$

This operator is extremely fast and requires only a few operations per element of operand. As a result, the proposed algorithm is summarized as follows:

Initialize $\lambda_1, \lambda_2, \lambda_3, \mu_1 = \frac{0.1}{\lambda_1}, \mu_2 = \frac{0.1}{\lambda_2}, \mu_3 = \frac{0.1}{\lambda_3}, u = 0, v^1, v^2, v^3 = 0, d^1, d^2, d^3 = 0, k = 0$

Loop ($k := k+1$)

$$u_{k+1} \coloneqq (A^TRA + \frac{1}{\mu_1}G^TG + \frac{1}{\mu_2}G^TG + \frac{1}{\mu_3}W^TW)^{-1}(A^TRy + \frac{1}{\mu_1}G^TGu_p + \frac{1}{\mu_1}G^T(v_k^1 - d_k^1) + \frac{1}{\mu_2}G^T(v_k^2 - d_k^2) + \frac{1}{\mu_3}W^T(v_k^3 - d_k^3)) \tag{5.22}$$

$$v_{k+1}^1 := \quad ST_{\mu_1\lambda_1}(G(u_{k+1}-u_p)+d_k^1) \tag{5.23}$$

$$d_{k+1}^1 := \quad d_k^1 + (G(u_{k+1}-u_p) - v_{k+1}^1) \tag{5.24}$$

$$v_{k+1}^2 := \quad ST_{\mu_2\lambda_2}(Gu_{k+1}+d_k^2) \tag{5.25}$$

$$d_{k+1}^2 := \quad d_k^2 + (Gu_{k+1} - v_{k+1}^2) \tag{5.26}$$

$$v_{k+1}^3 := \quad ST_{\mu_3\lambda_3}(Wu_{k+1}+d_k^3) \tag{5.27}$$

$$d_{k+1}^3 := \quad d_k^3 + (Wu_{k+1} - v_{k+1}^3) \tag{5.28}$$

Until $\|u^{k+1} - u^k\|_2 < \varepsilon$ (tolerance ε, e.g. 10^{-4})

5.2.5 Performance evaluation

5.2.5.1 Reference-based (high x-ray dose image) quantitative assessment

Structural SIMilarity (SSIM) index is a metric for measuring the structural similarity between two images. If ρ and t are two local image windows selected from the same position of two input images, SSIM is defined as follows:

$$SSIM(\rho, t) = \frac{2\mu_\rho\mu_t + C1}{\mu_\rho^2 + \mu_t^2 + C1} \cdot \frac{2\sigma_\rho\sigma_t + C2}{\sigma_\rho^2 + \sigma_t^2 + C2} \cdot \frac{\sigma_{\rho t} + C3}{\sigma_\rho\sigma_t + C3} \tag{5.29}$$

Where, μ_ρ and μ_t are the averages, $\sigma_\rho$and σ_t are the standard deviations and $\sigma_{\rho t}$ is the covariance of the local windows. 2C3 = C2 and C1 are constants to stabilize division.

Peak Signal to Noise Ratio (PSNR) and Relative Error (RE) are error sensitive quality metrics defined as follows:

$$PSNR(db) = 10\, log_{10}\left(\frac{Peak^2}{MSE}\right) \tag{5.30}$$

Where, Peak is the highest pixel value, e.g. in the case of 12-bit pixel representation, it is 1023; MSE is the mean square error between the reconstructed and reference images.

$$RE(\%) = \frac{\left\|u_{ref} - u_{rec}\right\|_2}{\left\|u_{ref}\right\|_2} \times 100 \tag{5.31}$$

Where, u_{rec} and u_{ref} are the reconstructed and reference images [C5.43].

5.2.5.2. Visual assessment

The images reconstructed by the different reconstruction algorithms at different numbers of projections were visually compared with the reference image to assess the reconstruction algorithms.

5.3 Experimental Results

MATLAB R2016b software was used to implement the algorithms on a Desktop PC with six Intel® Xeon® CPU 2GHz processors and 32GB memory.

5.3.1 Experiment Results using Simulated Data

5.3.1.1 Reconstructed images of a noise-free rat forelimb bone

A noise-free image of rat forelimb bone was used as the first experiment because it covers large and small structures. The size of this image is 512×512 pixels which is used to generate a fully sampled sinogram (512 views). Eight images were reconstructed by FBP, PICCS, Wavelet CS and the proposed algorithm using equally spaced 30 and 60 views subsampled sinograms which are uniformly extracted from the fully sampled sinogram (512 views).

The proposed algorithm is the combination of the wavelet based compressed sensing algorithm and the gradient based PICCS algorithm. The following optimization problems derived from the Eq. (5.7) were used to compare the wavelet CS and PICCS methods with the proposed method. The comparison results were shown in Fig. 5.2.

Wavelet based CS: $$\min_{u \in R^n} \quad \frac{1}{2}\|Au - y\|_R^2 + \lambda_3 \|Wu\|_{l_1} \tag{5.32}$$

Gradient based PICCS: $$\min_{u \in R^n} \quad \frac{1}{2}\|Au - y\|_R^2 + \lambda_1 \left\|G(u - u_p)\right\|_{l_1} + \lambda_2 \|Gu\|_{l_1} \tag{5.33}$$

The features of interest in these bone images are black holes (vascular canals) with different dimensions. These black holes, especially the smaller ones, are hidden because of severe aliasing artifacts in the images reconstructed by FBP in the Figs. 5.2E and 5.2F. However, as shown in the Figs. 5.2H and 5.2I, the gradient based PICCS algorithm is good in dealing with piecewise smooth regions, but it generates undesirable staircase artifact. On the other hand, as shown in the Figs. 5.2K and 5.2L, the wavelet-based CS algorithm is good at preserving fine structures, but it is not good for approximating piecewise smooth regions because of oscillations around edges. Finally, as demonstrated in Figs. 5.2B, 5.2C, the proposed algorithm is applied to remove the aliasing artifact while preserving the piecewise smooth regions and their internal fine structures. The Figs. 5.2D, 5.2G and 5.2J show three quality metrics, SSIM, PSNR, RE to clarify that the proposed algorithm is superior to the other algorithms tested. From the SSIM values, one may conclude that the proposed algorithm can suppress the artifacts, and the PSNR and RE values indicate that the highest reconstruction accuracy can be achieved using the proposed algorithm.

5.3.1.2 Reconstructed images of a noisy rat forelimb bone data

The second experiment was performed using noisy simulated data. Additive zero mean Gaussian white noise n of different relative magnitudes was purposely added to the sinograms. The reconstructed images were displayed in Fig. 5.3. To better compare the proposed algorithm with other methods, Table 5.1 and Fig.5.4 show three quality metrics, SSIM, PSNR, RE with respect to the sinogram SNR.

Compared to the conventional FBP method, the POCS method is more robust to noise and thus has greatly suppressed noise and streaking artifacts. However, as shown in Fig. 5.3E, blurring artifact is present and fine structures are not visible. As can be seen in Table 5.1 and Fig 5.4, POCS method is more successful than the FBP method with respect to the existing quality metrics at different levels of noise. The ASD-POCS and SpBR-TV methods apply gradient operator to remove noise and streak artifacts without generation of blurring effects but as illustrated in Figs. 5.3F and 5.3D, a number of blocky-shaped structures are seen in the images. Finally, as demonstrated in Figs. 5.3 and 5.4, the proposed algorithm is successful in controlling the trade-off between noise suppression and spatial resolution. From the Fig. 5.4 (25db SNR), we can see that the RE is below 25%, the PSNR is more than 28dB and the SSIM is more than 0.575 for the proposed algorithm. These results indicate that high reconstruction accuracy is achieved using the proposed algorithm and it is evident that the proposed algorithm showing robustness against noise.

5.3.1.3 Parameters selection – simulated data

The noise-free simulated rat forelimb bone dataset (60 views) described in section 5.3.1.1 was used as an example to show the procedure of determining the optimal parameters. For the proposed algorithm, there are six parameters $\lambda_1, \lambda_2, \lambda_3$ and μ_1, μ_2, μ_3 to be determined. The reconstruction relative error (RE) was alternately plotted against one parameter keeping the others fixed. We started by setting $\lambda_2 = 0.01, \lambda_1 = 0.01$. The Fig. 5.5A shows that the lowest reconstruction error is obtained when $\lambda_3 = 0.01$. Then we set $\lambda_3 = 0.01, \lambda_1 = 0.01$ and searched the optimal value for λ_2 that gives the lowest relative error, it is $\lambda_2 = 0.02$ as shown in Fig. 5.5B.

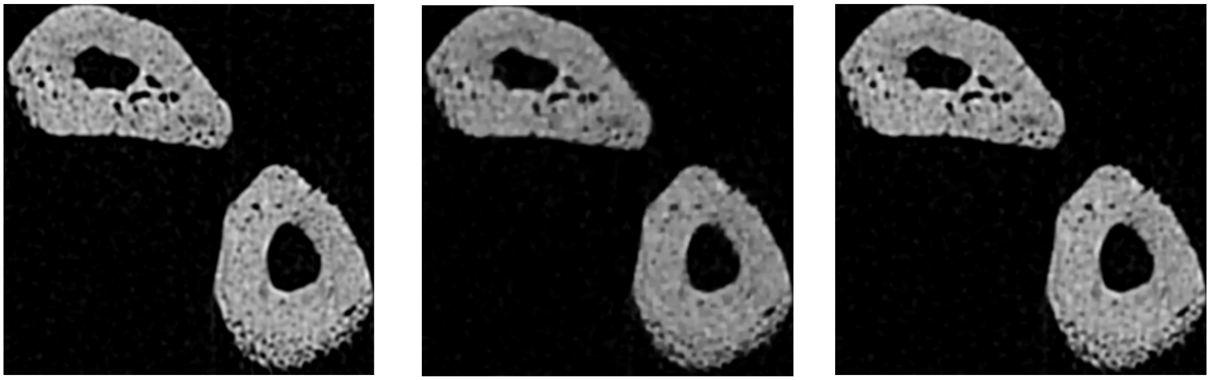

A) Reference B) Proposed (30 views) C) Proposed (60 views)

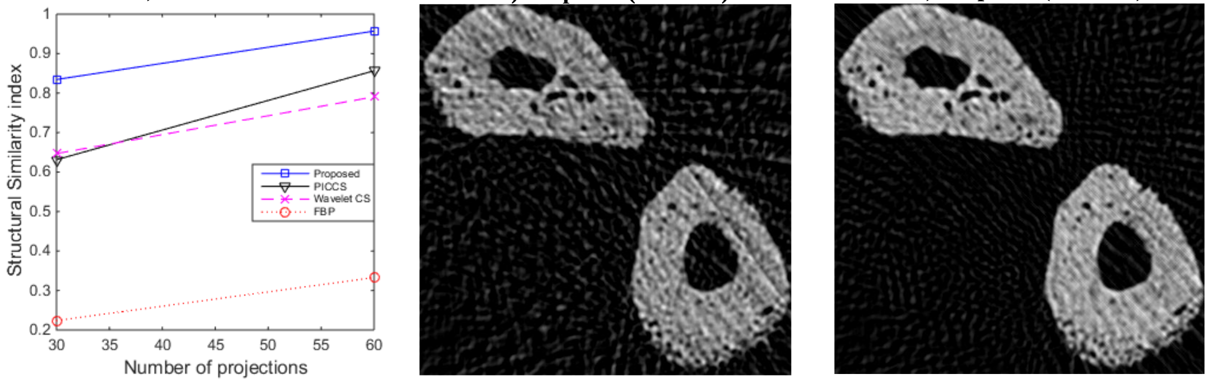

D) SSIM E) FBP (30 views) F) FBP (60 views)

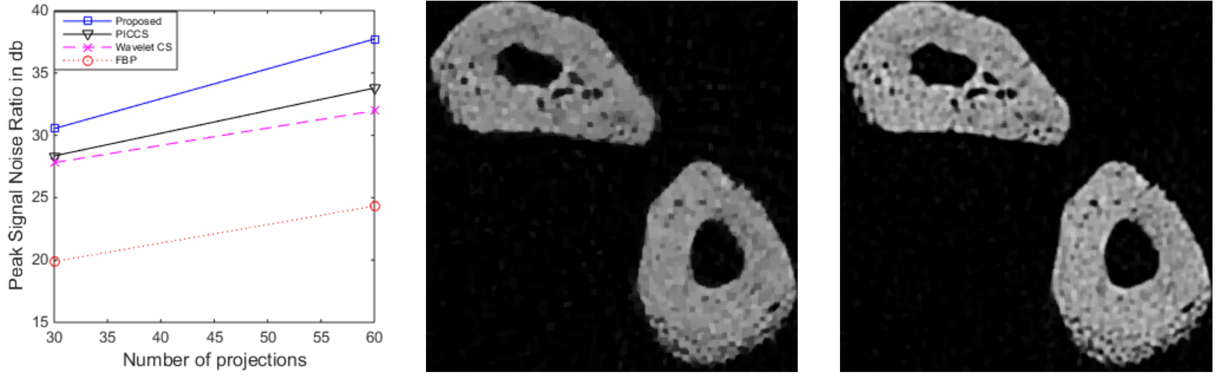

G) PSNR H) PICCS (30 views) I) PICCS (60 views)

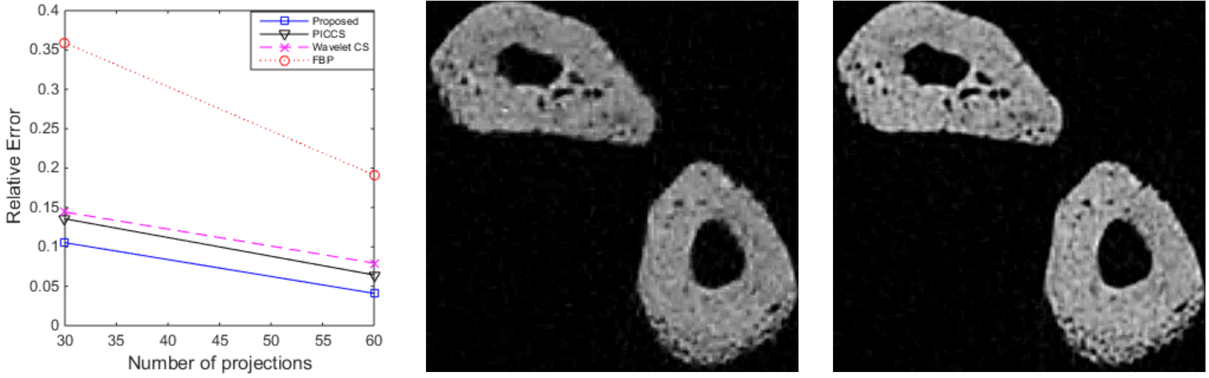

J) RE K) Wavelet CS (30 views) L) Wavelet CS (60 views)

Figure 5.2 Rat forelimb bones images reconstructed by the different algorithms using 30 and 60 views from simulated data

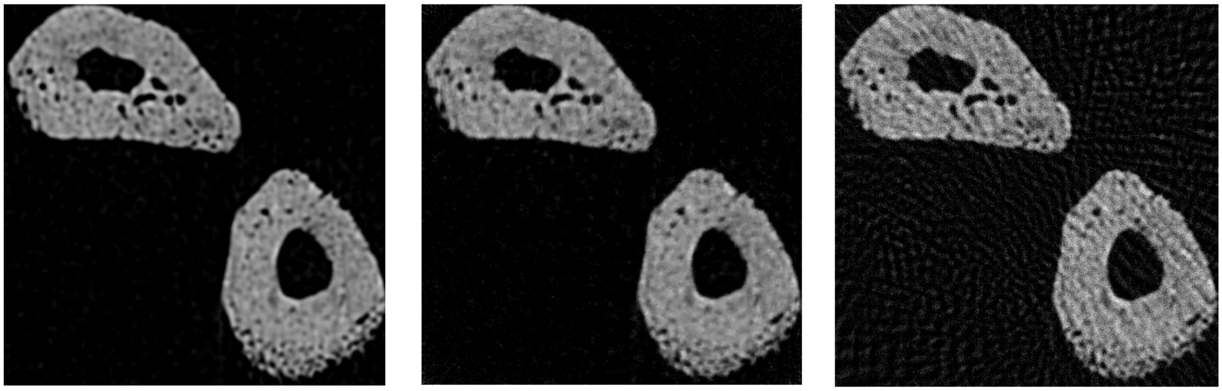

A) Reference **B) Proposed** **C) FBP**

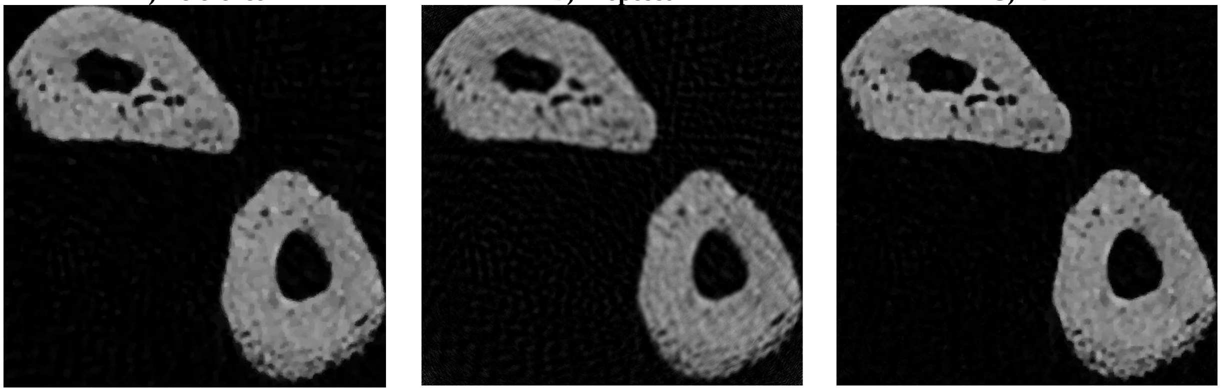

D) SpBR-TV **E) POCS** **F) ASD-POCS**

Figure 5.3 The rat forelimb bones reconstructed by the different algorithms using a noisy sinogram (60 views, 30db SNR). The features of interest are cortical bone pores (vascular canals) with different sizes

Table 5.1 Quality metrics of reconstructed rat forelimb bone image from noisy sinograms

Sinogram	25			30			35		
SNR	SSIM	PSNR (dB)	RE	SSIM	PSNR (dB)	RE	SSIM	PSNR (dB)	RE
Proposed	0.575	27.98	0.234	0.769	31.97	0.090	0.890	34.78	0.0585
SpBR-TV	0.488	27.72	0.229	0.659	29.80	0.119	0.703	29.90	0.1045
ASD-POCS	0.420	27.06	0.239	0.687	30.92	0.105	0.779	30.54	0.0933
POCS	0.274	24.24	0.333	0.405	27.03	0.173	0.432	26.74	0.1482
FBP	0.064	17.14	0.813	0.171	20.64	0.334	0.275	22.64	0.2366

Finally, we set $\lambda_2 = 0.02, \lambda_3 = 0.01$ and searched the optimal value for λ_1, the optimum value is $\lambda_1 = 0.01$ which can be verified in Fig. 5.5C. Thus, we used this repetitive process to find the optimum values of $\lambda_1, \lambda_2, \lambda_3$. As described in section 2.4, the other three parameters μ_1, μ_2, μ_3 was determined by these equations $\mu_1 = \frac{0.1}{\lambda_1}, \mu_2 = \frac{0.1}{\lambda_2}, \mu_3 = \frac{0.1}{\lambda_3}$.

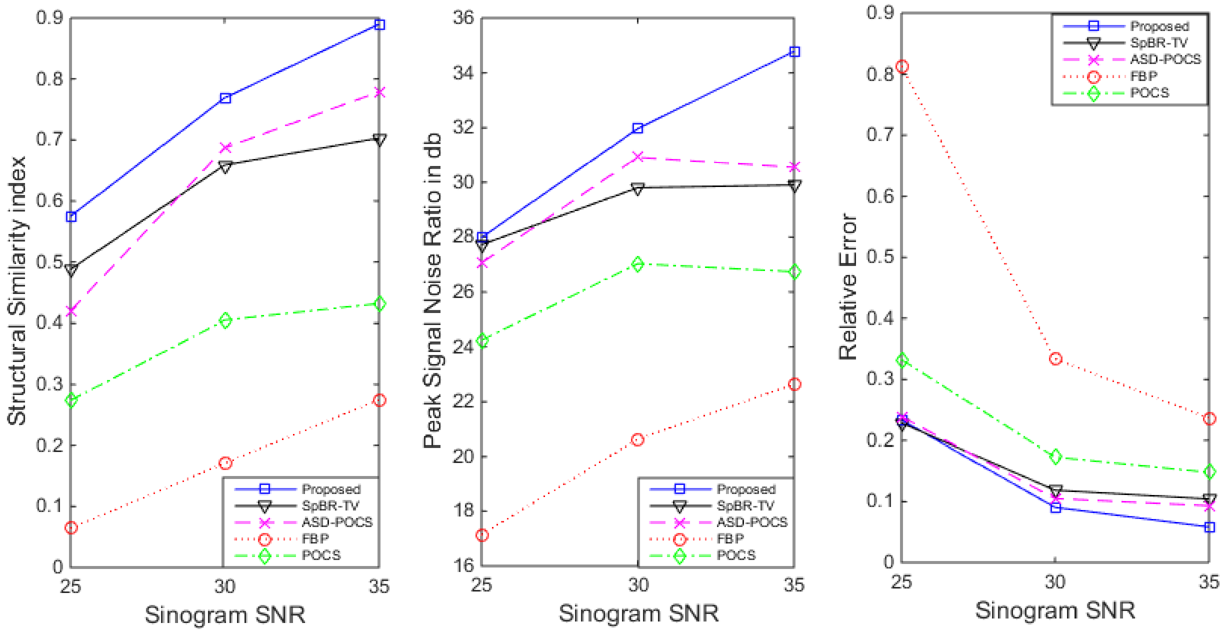

Figure 5.4 Rat forelimb bone image quality metrics vs sinogram signal noise ratio

This recurring procedure was conducted for the Wavelet CS and PICCS methods using the same dataset to find the corresponding optimal parameters (Table 5.2).

A similar searching procedure was used to find the regularization parameters for the proposed algorithm, SpBR-TV and ASD-POCS methods using the noisy dataset (60 views, 30db SNR) described in Section 5.3.1.2. The optimum parameter values for the proposed algorithm are $\lambda_1 = 0.005, \lambda_2 = 0.04, \lambda_3 = 0.015$ and $\mu_1 = 20, \mu_2 = 2.5, \mu_3 = 6.7$. The optimum regularization parameter in the SpBR-TV method is 25 and finally the optimum value of ε per ray measurement for the ASD-POCS method is 1.15×10^{-4}.

Table 5.2 Optimum parameter selections for rat forelimb bone simulated datasets

Data (60 views)	Wavelet CS		PICCS			Proposed Algorithm		
	λ_3, μ_3		λ_1, μ_1	λ_2, μ_2		λ_1, μ_1	λ_2, μ_2	λ_3, μ_3
Rat forelimb bone data without noise	0.05,2		0.02,5	0.03,3.3		0.01,10	0.02,5	0.01,10

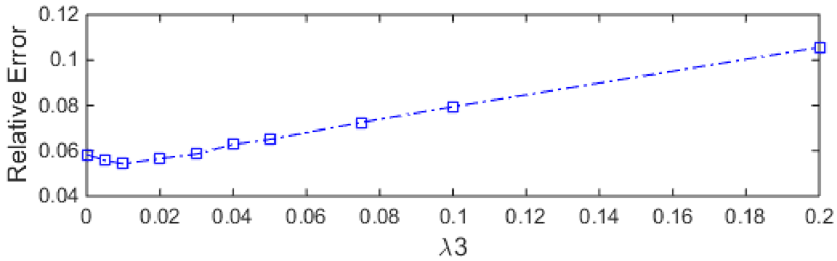

A) Searching for the optimum λ_3 **when** $\lambda_2 = 0.01, \lambda_1 = 0.01$

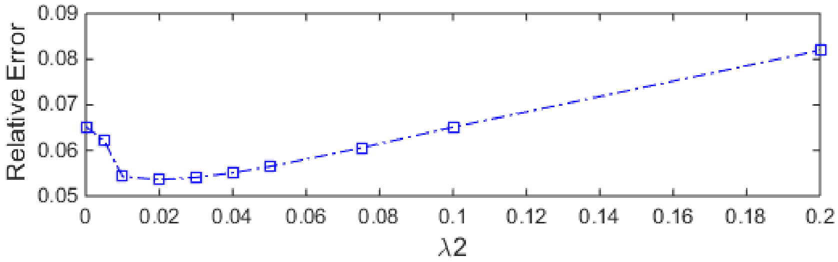

B) Searching for the optimum λ_2 **when** $\lambda_3 = 0.01, \lambda_1 = 0.01$

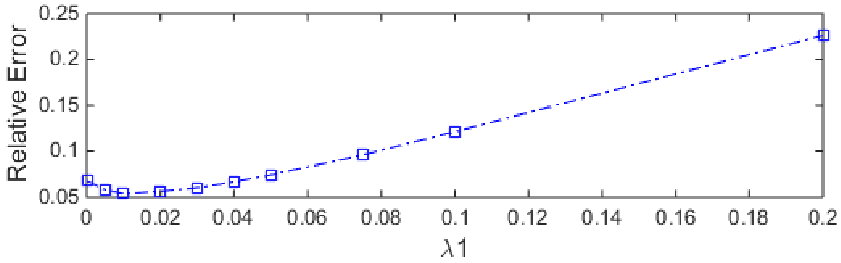

C) Searching for the optimum λ_1 **when** $\lambda_2 = 0.02, \lambda_3 = 0.01$

Figure 5.5 Analysis to find the optimum regularization parameters for the proposed method

5.3.2 Experiment Results using Real Data

5.3.2.1 Reconstructed images of a rat forelimb bone data

The proposed algorithm along with four existing reconstruction methods was used to reconstruct two randomly selected transverse slices of the rat forelimb. A reference image with the size of 4000×4000 pixels was reconstructed by the FBP method using the full sinogram dataset derived from all 750 equally spaced projections spanning 180 degrees. Five images were reconstructed by FBP, ASD-POCS, POCS, SpBR-TV and the proposed algorithm using three different collections of subsampled sinogram data i.e. 20% (150 views), 30% (225 views) and 40% (300 views) that were uniformly sampled from the 750 equally spaced projections spanning 180 degrees.

Fig. 5.6, shows the rat forelimb including two bones (radius and ulna), soft tissues and a plastic positioning rod (round structure to the left) which are reconstructed by the different algorithms using 30% of full projection data (225 views).

Fig. 5.7, shows the zoomed regions (the white dotted boxes in Fig. 5.6) of the periphery of the rat forelimb consisting of restraining tape and fur (visible due to phase contrast). Fig. 5.8, shows the zoomed region (the white dotted boxes in Fig. 5.6) of the rat forelimb including the radius and ulna bones (left and right, respectively). As it is evident in this figure, the features of interest are vascular canals (black holes in the white background) with different sizes. Fig 5.9, shows the restraining tape and fur in the second slice which are reconstructed by the different algorithms using 20% of full projection data (150 views) and Fig. 5.10, shows the radius and ulna bones reconstructed by the different algorithms using 40% of full projection data (300 views). Table 5.3 shows three metrics PSNR, SSIM and RE to quantify the reconstruction accuracy and the amount of noise suppression. The metrics are shown individually in Fig. 5.11, to better illustrate the effectiveness of the proposed algorithm.

5.3.2.2 Parameters selection – real data

The proposed algorithm is successful in controlling the trade-off between suppressing artifacts/noise and preserving the spatial resolution, if the parameters λ set to the proper values. If the values of λ are selected too low, the problem remains inconsistent, and if $\lambda_1, \lambda_2, \lambda_3$ are selected too high, the final image will have aliasing, over smoothing and ringing artifacts, respectively. Based on our experience, the lowest reconstruction error for our datasets is obtained when approximately $\lambda_i = 0.1\lambda_{i_{max}}$ where $\lambda_{i_{max}}$ are the critical values above which the solutions are $u = u_p \quad and \quad u = 0$, respectively. Therefore, the $\lambda_1, \lambda_2, \lambda_3$ values were chosen to be $(\lambda_1, \lambda_2, \lambda_3) = (0.025, 0.1, 0.075)$, $(\lambda_1, \lambda_2, \lambda_3) = (0.019, 0.075, 0.056)$ and $(\lambda_1, \lambda_2, \lambda_3) = (0.008, 0.033, 0.025)$ for 150, 225 and 300-view in our bone dataset, respectively. As described in section 5.2.4, the other three parameters μ_1, μ_2, μ_3 can be determined by the following equations $\mu_1 = \frac{0.1}{\lambda_1}, \mu_2 = \frac{0.1}{\lambda_2}, \mu_3 = \frac{0.1}{\lambda_3}$. The regularization parameter in SpBR-TV method was empirically chosen to ensure the lowest reconstruction error. The values of this parameter for bone data were chosen to be 10, 13.3 and 30.3 for 150, 225 and 300-view, respectively. For any regularization parameter used in the SpBR-TV method, there is a corresponding ε which was used in the ASD-POCS method to ensure fair comparison between algorithms [C5.17]. For the ASD-POCS method, the values of ε per ray measurement for bone data were chosen to be 3.15×10^{-4}, $1.31 \times 10^{-4}$and 4.76×10^{-5} for 150, 225 and 300-view, respectively.

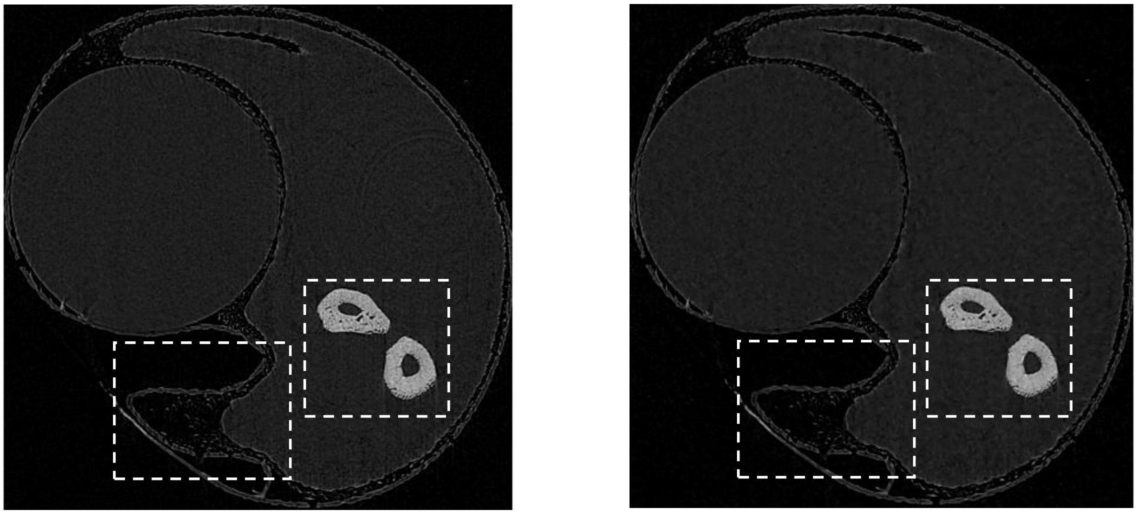

A) Reference (750 views)

B) Proposed (225 views)

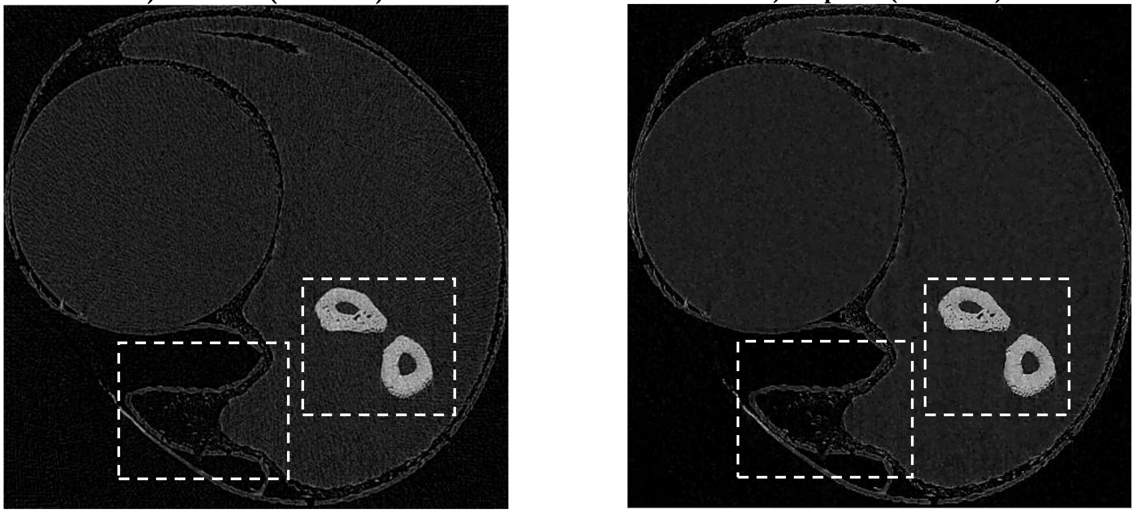

C) FBP (225 views)

D) SpBR-TV (225 views)

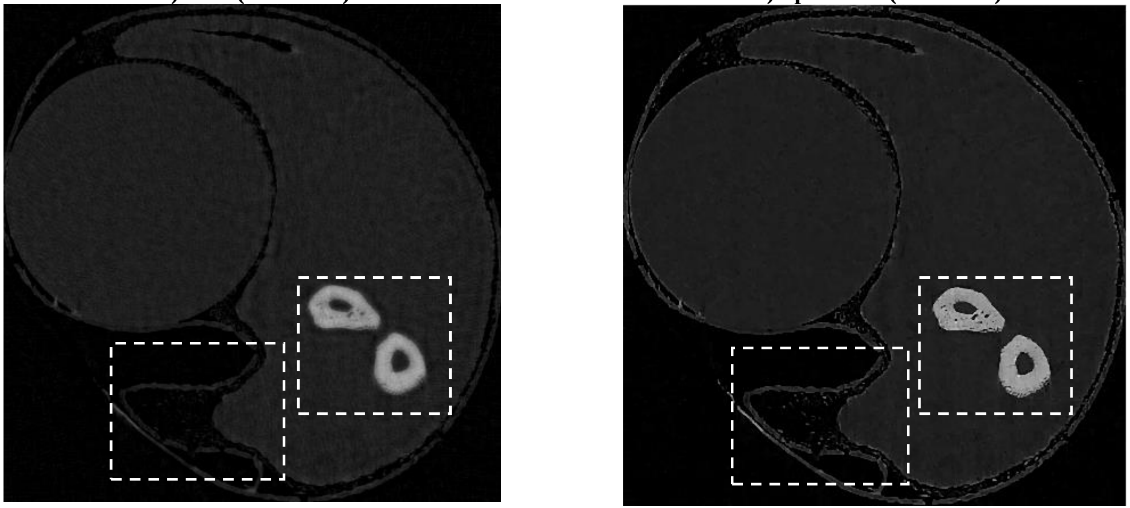

E) POCS (225 views)

F) ASD-POCS (225 views)

Figure 5.6 Slide 1: The rat forelimb showing the two bones (radius and ulna), soft tissues and a plastic positioning rod (round structure to the left) reconstructed by the different algorithms using 30% of full projection data (225 views)

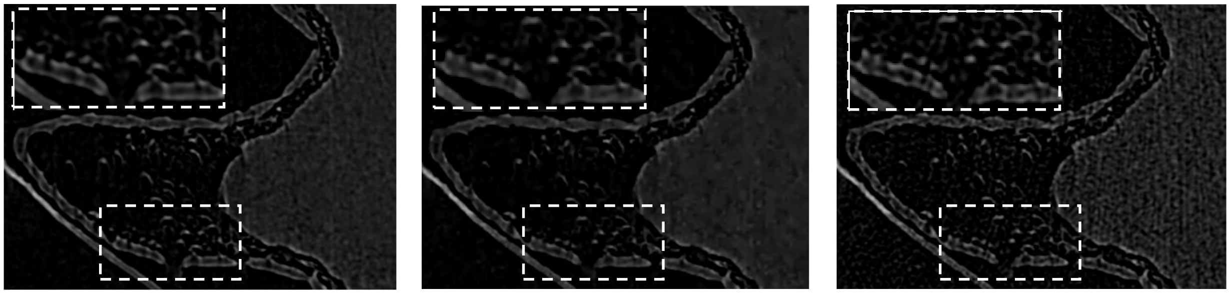

A) Reference (750 views) **B) Proposed (225 views)** **C) FBP (225 views)**

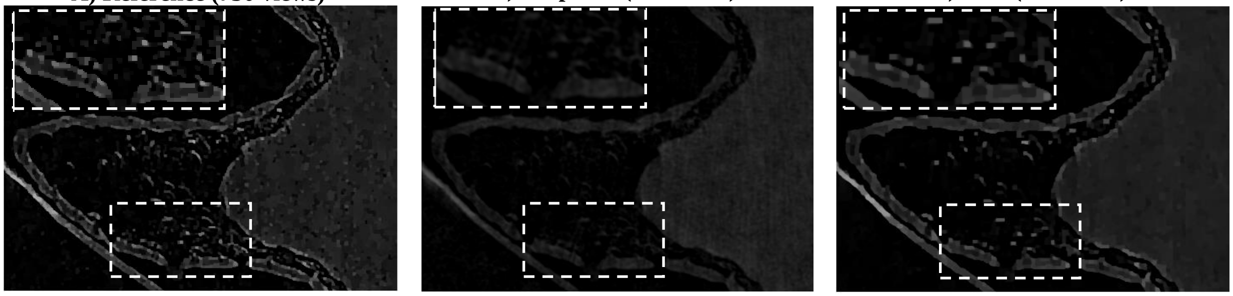

D) SpBR-TV (225 views) **E) POCS (225 views)** **F) ASD-POCS (225 views)**

Figure 5.7 Slice 1: The zoomed regions (the white dotted boxes in Fig. 5.6) of the periphery of the rat forelimb consisting of restraining tape and fur (visible due to phase contrast) reconstructed by the different algorithms using 30% of full projection data (225 views)

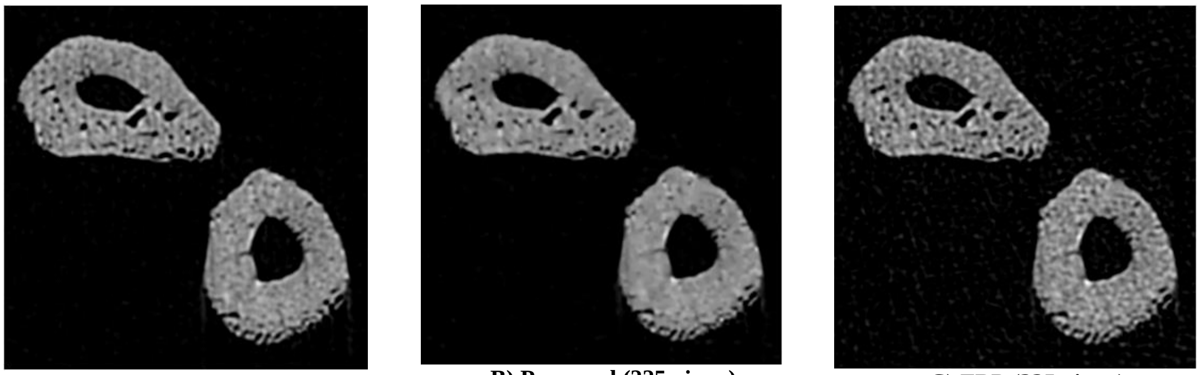

A) Reference (750 views) **B) Proposed (225 views)** **C) FBP (225 views)**

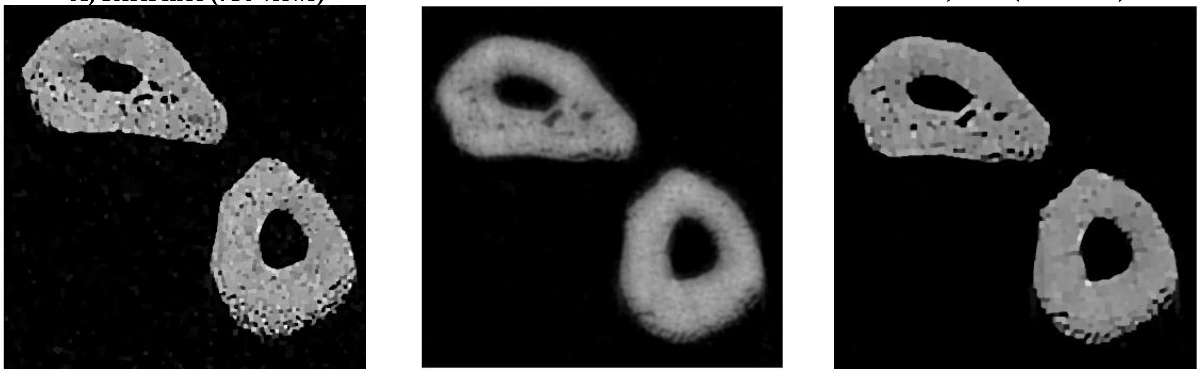

D) SpBR-TV (225 views) **E) POCS (225 views)** **F) ASD-POCS (225 views)**

Figure 5.8 Slice1: The zoomed regions (the white dotted boxes in Fig. 5.6) of the rat forelimb including the radius and ulna bones (left and right, respectively) reconstructed by the different algorithms using 30% of full projection data (225 views). The features of interest are cortical bone pores (vascular canals) with different sizes

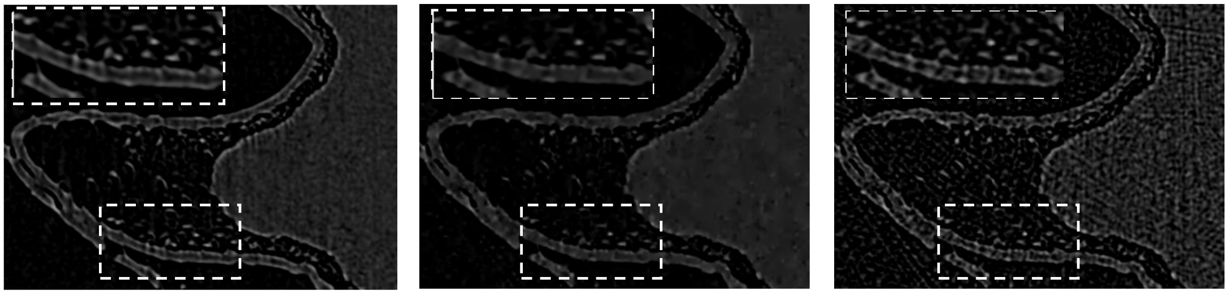

A) Reference (750 views) **B) Proposed (150 views)** **C) FBP (150 views)**

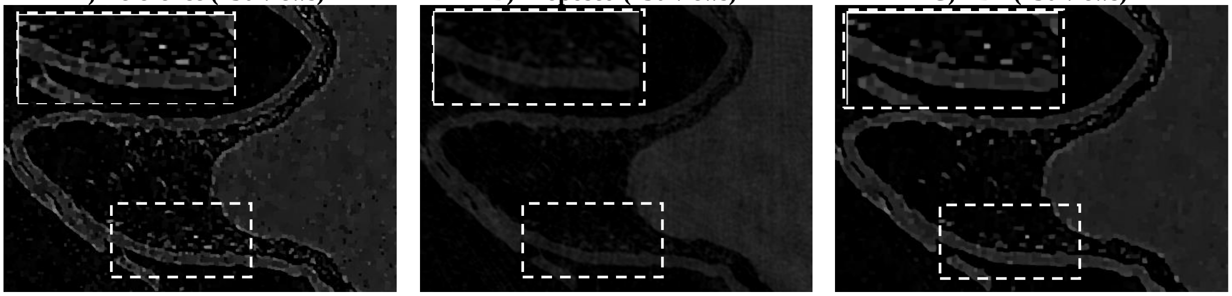

D) SpBR-TV (150 views) **E) POCS (150 views)** **F) ASD-POCS (150 views)**

Figure 5.9 Slice 2: The zoomed regions of the rat forelimb reconstructed by the different algorithms using 20% of full projection data (150 views). The details (the white dotted boxes) were zoomed in the left corner to better demonstrate the details

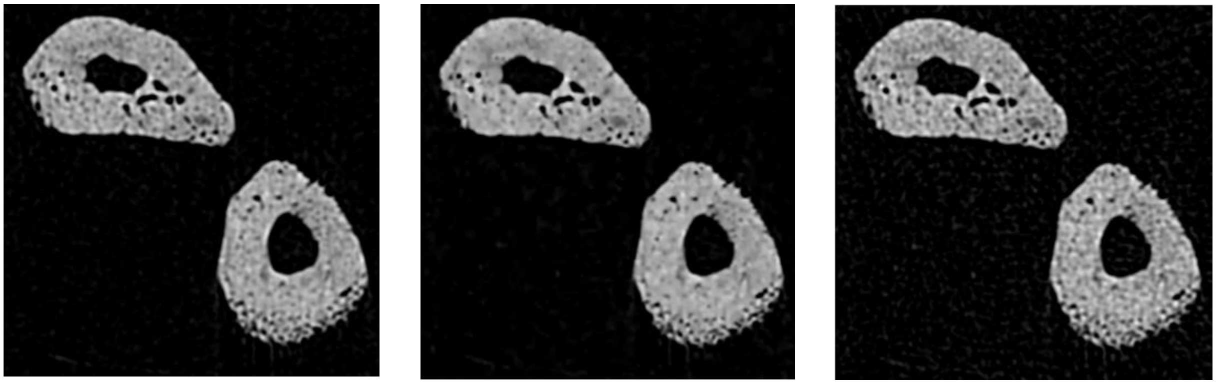

A) Reference (750 views) **B) Proposed (300 views)** **C) FBP (300 views)**

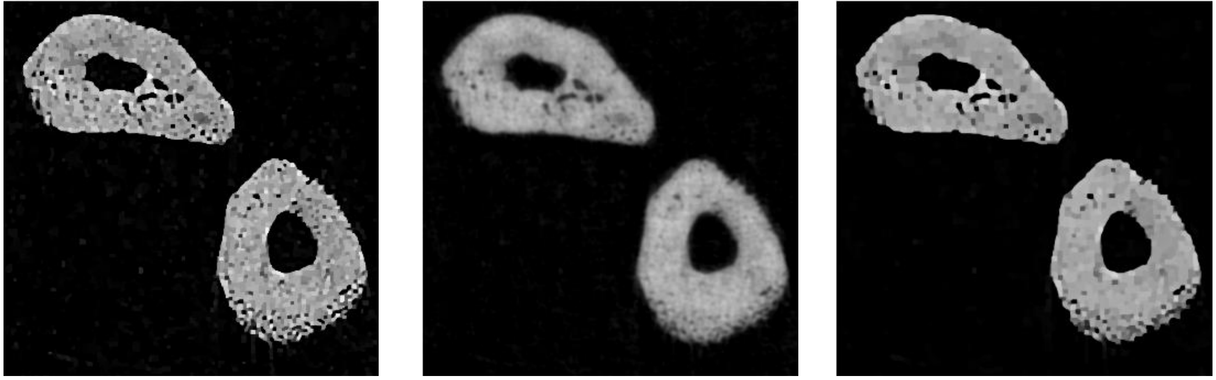

D) SpBR-TV (300 views) **E) POCS (300 views)** **F) ASD-POCS (300 views)**

Figure 5.10 Slice 2: The zoomed regions of the rat forelimb bones reconstructed by the different algorithms using 40% of full projection data (300 views). The features of interest are cortical bone pores (vascular canals) with different sizes

Table 5.3 Quality metrics of reconstructed rat forelimb bone image

Projection	20%			30%			40%		
Percentage	SSIM	PSNR (dB)	RE	SSIM	PSNR (dB)	RE	SSIM	PSNR (dB)	RE
Proposed	0.7014	30.49	0.2203	0.7627	32.95	0.1664	0.7877	33.74	0.1389
SpBR-TV	0.6587	27.71	0.2805	0.7013	28.58	0.2749	0.7120	29.10	0.2615
ASD-POCS	0.7023	29.84	0.2375	0.7461	31.25	0.2023	0.7537	31.60	0.1862
POCS	0.6123	25.68	0.3835	0.6523	26.98	0.3307	0.6769	27.60	0.2817
FBP	0.3606	23.86	0.4731	0.5011	27.09	0.3267	0.5949	28.93	0.2418

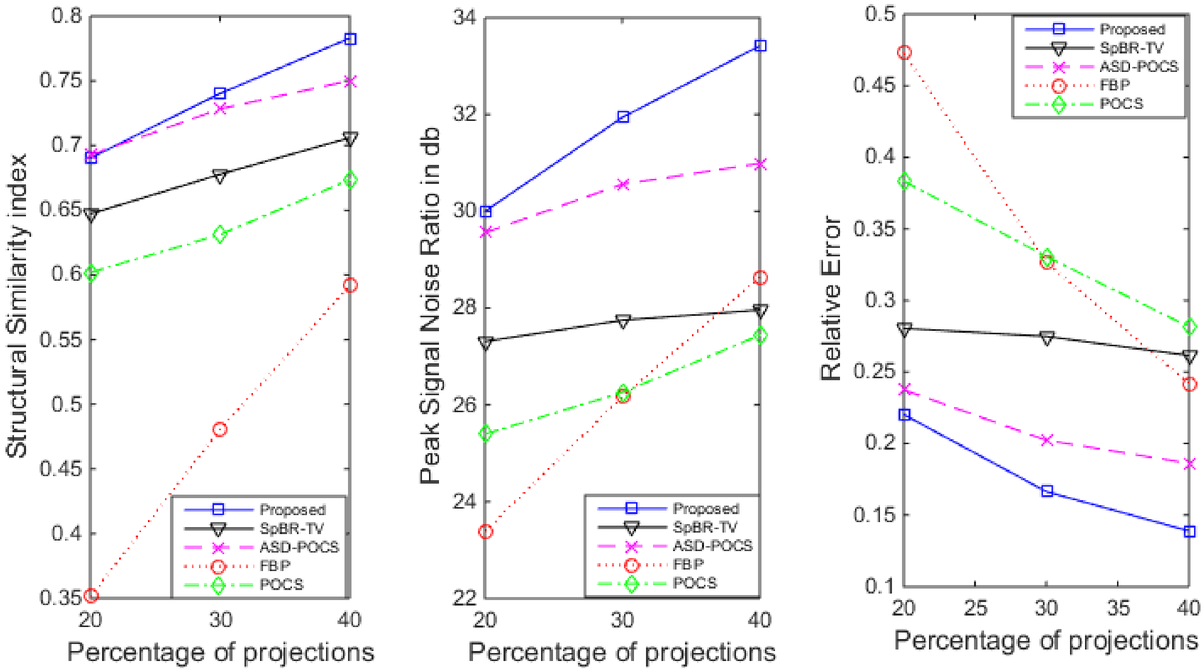

Figure 5.11 Rat forelimb bone image quality metrics vs percentage number of projections

5.4 Discussion

As expected, the images reconstructed by the FBP method in Figs. 5.10C show a great amount of aliasing artifact and noise over the entire image which are due to the limited number of projections (sampling rate lower than Nyquist rate). The image spatial resolution is significantly reduced, and, in some cases, it is difficult to view the features of interest i.e. vascular canals (cortical bone porosity) hidden by artifacts. Furthermore, these artifacts can mislead physicians to wrong diagnosis. In the Figs. 5.10E which show the images reconstructed by the POCS algorithm, the aliasing artifact and noise are reduced but edge blurring artifact reduces the spatial resolution and lower contrast and small details that are visible in the FBP reconstructed image are no longer be accurately distinguished. However, as illustrated in Table 5.3, and Fig. 5.11, the POCS method is superior to the FBP method especially at the highly incomplete number of projected data. The ASD-POCS method utilizes total-variation operator to reconstruct the sharp edges without generation of aliasing or blurring artifacts. As illustrated in Figs. 5.10F, although, this method is successful in recovering of the piecewise smooth area with the sharp edges, the lower contrast features are over-smoothed which obscure the presence of these features. The SpBR-TV method images in Figs. 5.10D show that the method is successful in preserving high-contrast edges without creating aliasing and blurring artifacts or generation of over-smoothed regions. However, this method leads to staircase (patchy) artifacts which in clinical practice, may mimic lesions. Finally, as demonstrated in Figs. 5.10B, the proposed algorithm is the most successful method in controlling the trade-off between artifact suppression and keeping spatial resolution. The proposed method minimizes noise and artifacts using both the gradient and wavelet domains and as shown in the zoomed area in Fig 5.8 and 5.10, almost all the vascular canals which are present in the reference image were reconstructed without generation of unwanted distortion.

The proposed algorithm has the highest PSNR and SSIM and lowest RE with respect to other methods even when the number of projections is only 150. From the SSIM values, one may conclude that the proposed algorithm is capable of suppressing artifacts and noise, leading to an image of acceptable quality at a lower number of view and the PSNR and RE values indicate that the highest reconstruction accuracy can be achieved using the proposed algorithm.

5.5 Conclusions

In this article, we have developed and investigated a wavelet-gradient based prior image constrained compressed sensing algorithm which aims to reconstruct diagnostically acceptable images from synchrotron datasets with potential for a significant reduction in the number of projections. The proposed algorithm was applied to a dataset collected at the Biomedical Imaging and Therapy Bending Magnet beamline at the Canadian Light Source. At present, a solution of large-scale CS optimization problems is poorly characterized with real synchrotron tomographic data which motivated us to propose a CS-based synchrotron CT reconstruction algorithm. The proposed algorithm achieved an optimal balance between artifact suppression and preserving spatial resolution which is assessed by visual and quantitative performance metrics. Using the proposed reconstruction algorithm to reduce the number of projections in synchrotron CT is an effective way to reduce the x-ray dose and scan time which improves in-vivo imaging protocols.

References

[C5.1] B. Wolkowski, E. Snead, M. Wesolowski, J. Singh, M. Pettitt, R. Chibbar, S. A. Melli, and J. Montgomery. "Assessment of freeware programs for the reconstruction of tomography datasets obtained with a monochromatic synchrotron-based X-ray source." Journal of synchrotron radiation, 22 (4), 1130-1138 (2015).

[C5.2] Spanne, P. and M.L. Rivers (1987). Computerized microtomography using synchrotron radiation from the NSLS. Nucl Instrum Meth B24/25: 1063–1067.

[C5.3] Sakamoto, K., Y. Suzuki, T. Hirano, and K. Usami (1988). Improvement of spatial resolution of monochromatic x-ray CT using synchrotron radiation. J Appl Phys 27: 127–132.

[C5.4] Tanaka T., Honda C., Matsuo S., Noma K., Oohara H., Nitta N. The first trial of phase contrast imaging for digital full-field mammography using a practical molybdenum X-ray tube. Invest Radiol 2005; 40(7):385-96.

[C5.5] Wu X, Liu H. Clarification of aspects in in-line phase-sensitive X-ray imaging. Med Phys 2007; 34(2):737-43.

[C5.6] Bravin A., Coan P., Suortti P. X-ray phase-contrast imaging: from pre-clinical applications towards clinics. Phys. Med. Biol 2013; 58:1–35.

[C5.7] Tang L., Li G., Sun YS., Li J., Zhang XP. Synchrotron-radiation phase-contrast imaging of human stomach and gastric cancer: in vitro studies. J Synchrotron Radiat. 2012; 19:319-22.

[C5.8] Snigirev A., Snigireva I., Kohn V., Kuznetsov S., Schelokov I., On the possibilities of x-ray phase contrast microimaging by coherent high-energy synchrotron radiation. Review of Scientific Instruments, 1995; 66 (12): 5486–5492.

[C5.9] Cloetens P., Pateyron-Salomé M., BuffièRe JY., Peix G., Baruchel J., Peyrin F., Schlenker M., Observation of microstructure and damage in materials by phase sensitive radiography and tomography. Journal of Applied Physics 1997; 81 (9): 5878–5886.

[C5.10] McEwen BF., Downing KH. Glaeser RM. The relevance of dose-fractionation in tomography of radiation-sensitive specimens. Ultramicroscopy 1995; 60:357‑373.

[C5.11] Crowther RA., DeRosier DJ. Klug A. The reconstruction of a three dimensional structure from projections and its application to electron microscopy. Proc. R. Soc. B, 1970; 317:319-340.

[C5.12] Kak AC and Slaney M, Principles of Computerized Tomographic Imaging, New York: IEEE Press 1988.

[C5.13] Herman G.T., Lent A. and Rowland S.W. ART: mathematics and applications. A report on the mathematical foundations and on the applicability to real data of the algebraic reconstruction techniques. Journal of Theoretical Biology, 1973; 42-1:1–32

[C5.14] Graff, Christian G., and Emil Y. Sidky. "Compressive sensing in medical imaging." Applied optics 54.8 (2015): C23-C44.

[C5.15] E. Y. Sidky and X. Pan, "Image reconstruction in circular cone-beam computed tomography by constrained, total-variation minimization," Phys. Med. Biol. 53, 4777-4807, 2008.

[C5.16] Sidky, E. Y., Kao, C. M., & Pan, X. (2006). Accurate image reconstruction from few-views and limited-angle data in divergent-beam CT. Journal of X-ray Science and Technology, 14(2), 119-139.

[C5.17] Bian, J., Siewerdsen, J. H., Han, X., Sidky, E. Y., Prince, J. L., Pelizzari, C. A., & Pan, X. (2010). Evaluation of sparse-view reconstruction from flat-panel-detector cone-beam CT. Physics in medicine and biology, 55(22), 6575.

[C5.18] Han, X., Bian, J., Eaker, D. R., Kline, T. L., Sidky, E. Y., Ritman, E. L., & Pan, X. (2011). Algorithm-enabled low-dose micro-CT imaging. Medical Imaging, IEEE Transactions on, 30(3), 606-620.

[C5.19] A. Beck and M. Teboulle, "A fast iterative shrinkage-thresholding algorithm for linear inverse problems," SIAM J. Imag. Sci., vol. 2, no. 1, pp. 183–202, 2009.

[C5.20] T. Goldstein and S. Osher, “The split Bregman method for L1-regularized problems,” SIAM J. Imag. Sci., vol. 2, no. 2, pp. 323–343, 2009.

[C5.21] Afonso, Manya V., José M. Bioucas-Dias, and Mário AT Figueiredo. "Fast image recovery using variable splitting and constrained optimization." Image Processing, IEEE Transactions on 19.9 (2010): 2345-2356.

[C5.22] B. Vandeghinste, B. Goossens, J. D. Beenhouwer, A. Pizurica, W. Philips, S. Vandenberghe, and S. Staelens, “Split-Bregman-based sparse-view CT reconstruction,” in Proc. Int. Meeting Fully 3-D Image Recon. Rad. Nucl. Med, 2011, pp. 431–434.

[C5.23] Ritschl, L., Bergner, F., Fleischmann, C., & Kachelrieß, M. (2011). Improved total variation-based CT image reconstruction applied to clinical data. Physics in medicine and biology, 56(6), 1545.

[C5.24] Song, J., Liu, Q. H., Johnson, G. A., & Badea, C. T. (2007). Sparseness prior based iterative image reconstruction for retrospectively gated cardiac micro-CT. Medical physics, 34(11), 4476-4483.

[C5.25] Donoho, D. L., & Huo, X. (1999, October). Combined image representation using edgelets and wavelets. In SPIE's International Symposium on Optical Science, Engineering, and Instrumentation (pp. 468-476). International Society for Optics and Photonics.

[C5.26] Chan, T. F., & Zhou, H. M. (2007). Total variation wavelet thresholding. Journal of Scientific Computing, 32(2), 315-341.

[C5.27] Ono, Shunsuke, Takamichi Miyata, and Katsunori Yamaoka. "Total variation-wavelet-curvelet regularized optimization for image restoration." Image Processing (ICIP), 2011 18th IEEE International Conference on. IEEE, 2011.

[C5.28] Chen, G. H., Tang, J., & Leng, S. (2008). Prior image constrained compressed sensing (PICCS): a method to accurately reconstruct dynamic CT images from highly undersampled projection data sets. Medical physics, 35(2), 660-663.

[C5.29] Lauzier, P. T., Chen, G. H. (2013). Characterization of statistical prior image constrained compressed sensing (PICCS): II. Application to dose reduction. Medical Physics, 40(2):021902.

[C5.30] Tang J., Lauzier P. T., and Chen, G. H (2011). Dose reduction using prior image constrained compressed sensing (DR-PICCS). In Proc. SPIE (Vol. 7961, p. 79612K).

[C5.31] Douglas J and Rachford HH, On the numerical solution of heat conduction problems in two or three space variables, Trans. Amer. Math. Soc 1956; 82:421–439.

[C5.32] G. L. Zeng, and G. T. Gullberg. "Unmatched projector/backprojector pairs in an iterative reconstruction algorithm." Medical Imaging, IEEE Transactions, 19 (5), 548-555 (2000).

[C5.33] D. S. Lalush and B. M.W. Tsui, "Improving the convergence of iterative filtered backprojection algorithm," Med. Phys., 21, 1283-1286 (1994).

[C5.34] C. L. Epstein. "Introduction to the Mathematics of Medical Imaging.", Prentice Hall, Upper Saddle River, N.J., 2003.

[C5.35] S. S. Chen, D. L. Donoho, and M. A. Saunders, "Atomic decomposition by basis pursuit," SIAM J. Sci. Comput., 20(1):33–61, 1998.

[C5.36] Cohen A., Daubechies I., and Vial P. Wavelets and fast wavelet transforms on an interval. Applied and Comput. Harmonic Ana., 1:54-81, 1993.

[C5.37] R. T. Rockafellar, Convex Analysis, Princeton University Press, Prince-ton, NJ, 1970.

[C5.38] Bertsekas Dimitri P. Constrained optimization and Lagrange multiplier methods. Athena Scientific, 1996.

[C5.39] J. Eckstein and D. P. Bertsekas. "On the Douglas—Rachford splitting method and the proximal point algorithm for maximal monotone operators." Mathematical Programming, 55 (1-3), 293-318 (1992).

[C5.40] M. R. Hestenes and E Stiefel. Methods of conjugate gradients for solving linear systems. 49, 1952.

[C5.41] Michailovich O. An iterative shrinkage approach to total-variation image restoration. IEEE Trans. Image Process. 2011; 20-5:1281–1299.

[C5.42] Donoho, David L. "De-noising by soft-thresholding." IEEE transactions on information theory 41, no. 3 (1995): 613-627.

[C5.43] Wang Z, Bovik AC, Sheikh HR, Simoncelli EP. Image quality assessment: from error visibility to structural similarity. IEEE Transactions on Image Processing 2004; 13: 600–612.

6. Summary and Suggestions for Further Studies

6.1 Summary of Work

Traditionally CT requires a large number of angular projections to reconstruct images with high resolution, which is necessary for detailed and accurate diagnosis. However, this poses great risks and challenges for in vivo human and animal imaging due to a large amount of x-ray radiation dose that can damage living specimens and induce genetic and cancerous diseases. In addition, longer scan times increase the risk of specimen movement, which introduces motion artifact in the reconstructed images. The CS field addresses the issue of how little data one can acquire and still be able to recover the image. Typically, N linearly independent samples are required to reconstruct an image $x \in R^N$. According to the CS theory, when the image x is sparse enough then by acquiring the right but fewer than N samples, the image x can be accurately reconstructed by solving a sparsity regularized (SR) minimization problem. Random sensing matrices that are dense and incoherent, play a key role in the CS theory and it is shown that random sampling gives higher recoverability performance than structured sampling [C6.1]. In contrast, the object in CT is scanned by line integrals, each line integral samples a small section of the object, so forming a highly structured, sparse and coherent CT sampling matrix. In chapter 3, CT projection views are collected using a realistic synchrotron imaging setup and a compressed sensing based algorithm is proposed to reconstruct the image of sufficient quality compared with the results of the conventional CT reconstruction methods. Simulated noise-free CT data are considered in this chapter to simplify the reconstruction challenges, such as application-specific varying noise levels and inconsistencies in the data.

We require a solver that can be applied to solve the non-smooth and high-resolution synchrotron CT reconstruction problem (3.3), where the reconstructed images may contain 2500×2500 or more pixels. In chapter 3, the Douglas–Rachford Splitting (DRS) method originally used in [C6.2] for solving matrix equations is proposed to solve the SR reconstruction problem (3.3). The convergence of this method is shown in a theorem by Eckstein and Bertsekas in [C6.3]. As discussed in [C6.4], the DRS method converges under much more relaxed conditions in the sense that the cost function does not need to be differentiable or finite so the DRS algorithm can handle non-smoothness in Eq. (3.3) without corner rounding technique. Furthermore, the DRS algorithm can perform distributive optimization, which is useful in solving large-scale problems such as synchrotron CT reconstruction. Finally, the spirit of CS-style image reconstruction involves solving unconstraint optimization problems for small λ as is the case in Eq. (3.3) which is technically challenging. DRS method can work with small values of λ because in addition to the Lagrange term, a quadratic penalty term is also included in the DRS cost function.

The lowest reconstruction error will be achieved if the regularization parameter λ set to a proper value. The proper value of λ shifts if the dataset and/or the system matrix change. Generally speaking, the greater number of projection views or the greater number of nonzero entries in the gradient of the final image, the smaller the value of optimal λ, and vice versa. Based on our experience, the SR reconstruction problem (3.3) is first solved with the regularization parameter $\lambda = 0.2\lambda_{max}$ where $\lambda_{max} = \|A^T b\|_\infty$ is an estimation of the critical value of λ above which the solution of the problem (3.3) is zero. If the selected $\lambda = 0.2\lambda_{max}$ is too low, the final image will have the aliasing artifact and if it is too high, the final image will be over smoothed. Depending on the result of this experiment, the other values of λ that are spaced from $0.01\lambda_{max}$to $0.95\lambda_{max}$will be tested to find the lowest reconstruction error. The benefit of including the penalty term $\frac{\rho}{2}\|Fx - z\|_2^2$ in Eq. (3.6) is to improve the conditioning of the problem and thus improve the convergence of the randomized Kaczmarz method for updating x. One method for adjusting the parameter ρ is to increase it until the randomized Kaczmarz method converges quickly enough. Based on our experience, the penalty parameter is set to $\rho = 20\,\lambda$ for the iterations. The variables u, z and x are initialized to zero. The SR reconstruction problem (3.3) is a convex optimization problem and there is only one globally optimal solution; so, the final result is not dependent on the choice of ρ and the initial values for u, z and x.

The Kaczmarz algorithm is used to solve linear Eq. (3.14). It requires an initial guess and generates a sequence of iterations $\{x^k\}$ that converge. The reason for selecting this method is because only one matrix row is used in each iteration and the iterations are faster when the matrix is sparse. This is especially useful when the number of rows is very large. Both conditions are true in Eq. (3.14). The convergence rate of the algorithm depends on the angle between the convex sets formed by the rows of the matrix [C6.5]. It is demonstrated that a random selection of the matrix rows (randomized Kaczmarz algorithm) can improve the convergence rate [C6.6]. The guarantee of randomized Kaczmarz algorithm convergence is shown in [C6.7].

In selecting a test phantom, we look for an image with a sparse gradient domain to demonstrate the efficacy of total variation in reducing the number of projection views. A computer abdomen phantom of 512×512 pixels is used for the first experiment because it covers large and small-scale structures. Five images were reconstructed by the proposed algorithm and other reconstruction methods using four different collections of subsampled sinogram data i.e. 7% (25 views), 10% (36 views), 20% (72 views) and 40% (144 views) that were uniformly sampled from the 360 equally spaced projections spanning 180 degrees. As it is evident from Table 3.1, a sharp recovery transition takes place when the number of projection views is increased from 7% (25 views) to 20% (72 views). As shown in Fig. 3.1, the proposed algorithm is able to perfectly reconstruct the abdomen phantom using only 20% (72 views) of the projected data. Simple geometric shapes of uniform grey levels are used in the computer phantoms that are typically utilized in the CT image reconstruction. However, phantoms should also include texture features that are somewhat reflective of what is found in CT applications. Thus, we generate a parallel-beam synchrotron CT dataset of a canine prostate. The data consists of 3751 equiangular projections acquired on a photonic Science VHR-90 array radiation camera at the Canadian Light Source (CLS) operated at 30 kV monochromatic synchrotron x-ray source, 25m source-to-sample and 5m sample-to-detector distances. The central slice is reconstructed onto a 2500-pixel image (pixel size 18.67 µm) from the corresponding rows of data using the Filtered Back Projection (FBP) reconstruction method. Five images were reconstructed by the proposed algorithm and other reconstruction methods using four different collections of subsampled sinogram data i.e. 20% (750 views), 30% (1125 views), 40% (1500 views) and 50% (1875 views) that were uniformly sampled from the 3751 equally spaced projections spanning 180 degrees. As it is evident from Table 3.2 and Fig. 3.7, the results for the texture phantom are visually accurate for as few views as 50% (1875 views) of the projection views, however, there is no sharp recovery transition for the texture phantom.

In contrast with chapter 3, where consistent simulated projection data are generated for image reconstruction, the reduced-view inconsistent real ex-vivo synchrotron absorption contrast bone data are used in chapter 4. A gradient based SR image reconstruction problem is formulated, and the DRS and the preconditioned conjugate gradient methods are utilized to solve the optimization problem. The wavelet image denoising algorithm is used as the post-processing algorithm to attenuate the unwanted staircase artifact generated by the reconstruction algorithm.

Depending on the final image gradient sparsity and the number of projection views, the values of λ that are spaced from $0.01\lambda_{max}$to $0.95\lambda_{max}$ where λ_{max} is the critical value of λ above which the solution of the problem (4.4) is zero, should be tested to find the lowest reconstruction error. If the selected λ is too low, the final image will have the aliasing artifact and if it is too high, the final image will be over smoothed. After some trial and error, the SR reconstruction problem (4.4) is solved with the regularization parameter $\lambda = 0.1\lambda_{max}$ to achieve the lowest reconstruction error. The variables u, v and d are initialized to zero. The initial value of the penalty parameter was set to $\mu = 0.1\lambda^{-1}$ and then a varying penalty parameter scheme discussed in [C6.8] is used to make the performance less dependent on the initial value. The SR reconstruction problem (4.4) is a convex optimization problem; so, the final optimal result is not dependent on the choice of μ and the initial values for u, v and d.

In addition to the Kaczmarz algorithm, which is very popular in the computed tomography image reconstruction, there are other methods to solve linear equations. It is shown in [C6.7] that the conjugate gradient algorithm can outperform the randomized Kaczmarz algorithm in terms of computational efficiency when the number of equations and unknowns are close in value. Therefore, the conjugate gradient algorithm is used in this chapter. Also, an unmatched backprojector is used to speed up the conjugate gradient algorithm. As shown in Eq. (4.2), a ramp filter R is used to form the unmatched backprojector $F = A^T R$ where matrix A is the projector in Eq. (4.1) and the transposed matrix $A^T$is the matched backprojector. A valid backprojector should not have negative eigenvalues in the backprojector–projector matrix to guarantee the convergence. As shown in [C6.9], the eigenvalues of the square matrix FA are positive because the matrix is diagonally dominant with positive diagonal elements. Furthermore, the conjugate gradient algorithm converges faster using unmatched backprojector F, because the square matrix FA is closer to the identity matrix, in the sense that the eigenvalues of the matrix are clustered closer together than the eigenvalues of the square matrix $A^T A$ [C6.9].

In selecting a test phantom, we look for an approximately piecewise smooth bone image with the gradient domain sparsity to demonstrate the efficacy of total variation in reducing the number of projection views. Furthermore, an exposure time of 1 second per frame and two-frame averaging are employed for each projection to increase the data signal to noise ratio. The data consists of 1800 equiangular projections of a block of femoral cortical bone acquired with a Hamamatsu

C9300 CCD camera at the Canadian Light Source (CLS). The detector is placed directly behind the sample in the experimental setup used for acquiring the synchrotron absorption contrast micro-CT dataset and the sample was placed on a rotating mechanical stage that was 26 m away from the synchrotron source. The central slice is reconstructed onto a 2791-pixel reference image (pixel size 5 µm) from the corresponding rows of data using the Filtered Back Projection (FBP) reconstruction method. Five images were reconstructed by the proposed algorithm and other reconstruction methods using three different collections of subsampled sinogram data i.e. 5% (90 views), 10% (180 views) and 15% (270 views) that were uniformly sampled from 1800 equally spaced projections spanning 180 degrees. The features of interest in the reconstructed images are holes (vascular canals) with different sizes. As it is evident from Table 4.2, Fig. 4.5 and Fig. 4.6, the results for the phantom is visually accurate for as few views as 15% (270 views) of the projection views.

In contrast with chapter 4, where the reduced-view real ex-vivo synchrotron absorption contrast bone data are utilized for image reconstruction, the highly reduced-view noisy real in-vivo synchrotron phase contrast CT bone data are used in chapter 5. A multi-regularization constraint SR image reconstruction problem which is a combination of prior image constrained CS framework, and the wavelet regularization is formulated, and the DRS and the preconditioned conjugate gradient methods are utilized to solve the optimization problem. The prior image constrained CS framework takes advantage of the prior image to promote the sparsity of the target image. It may lead to an unwanted staircase artifact when applied to noisy and texture images, so the wavelet regularization is used to attenuate the unwanted staircase artifact generated by the prior image constrained CS reconstruction algorithm.

As described in the parameter selection section of chapter 5, if the selected values of λ are too low, the problem remains inconsistent and if $\lambda_1, \lambda_2, \lambda_3$ are selected too high, the final image will have the aliasing, over smoothing and ringing artifacts, respectively. Based on the result of the experiment, the values of λ that are spaced logarithmically from $0.01\lambda_{i_{max}}$ to $0.95\lambda_{i_{max}}$ where $\lambda_{i_{max}}$ are the critical values above which the solutions are $u = u_p$ and $u = 0$ respectively, will be tested to find the lowest reconstruction error. After some trial and error, the lowest reconstruction error for the SR reconstruction problem (5.7) is obtained when approximately $\lambda_i = 0.1\lambda_{i_{max}}$. After some trial and error, the penalty parameters μ_1, μ_2, μ_3 are set to $\mu_1 = \frac{0.1}{\lambda_1}, \mu_2 = \frac{0.1}{\lambda_2}, \mu_3 = \frac{0.1}{\lambda_3}$

for the iterations. The variables u, v^1, v^2, v^3 and d^1, d^2, d^3 are initialized to zero. The SR reconstruction problem (5.7) is a convex optimization problem; so, the final optimal result is not dependent on the choice of μ and the initial values of u, v^1, v^2, v^3 and d^1, d^2, d^3. Prior image u_p in Eq. (5.4) is a low noise low spatial resolution image obtained by filtering FBP reconstructed image with a 2D rotationally symmetric Gaussian smoothing kernel of size [3, 3] with standard deviation of 1. The Gaussian filter kernel size and the standard deviation are determined by trial and error. The difference image $u - u_p$ should contain two main high spatial frequency signals: edges and noise. Since noise is not inherently sparse, it is minimized preferably in the reconstructed image. However, the data fidelity term in Eq. (5.4) enforces consistency with the projection data to recover the edges in the final image.

In selecting a test phantom, we aim to illustrate the effectiveness of the combination of prior image constrained CS framework, and the wavelet regularization in reducing the necessary number of projection views. The in-vivo phase contrast projection dataset used in this chapter is noisier than the absorption contrast micro-CT projection dataset used for the ex-vivo study proposed in the previous chapter. Furthermore, the number of acquired projections and the radiation exposure time per projection are less than the values set for the ex-vivo study. The data consists of 750 equiangular projections of a rat forelimb (including the radius and ulna bones) acquired with a C4742-95 – 12HR camera which includes a C4742-56 – 12HR CCD Detector at the Canadian Light Source (CLS). The sample was rotated continuously with a rotation velocity of 0.20 degree/sec through 0 to 180°, generating 750 projections. The central slice is reconstructed onto a 4000-pixel reference image (pixel size 13 µm) from the corresponding rows of data using the Filtered Back Projection (FBP) reconstruction method. Five images were reconstructed by the proposed algorithm and other reconstruction methods using three different collections of subsampled sinogram data i.e. 20% (150 views), 30% (225 views) and 40% (300 views) that were uniformly sampled from the 750 equally spaced projections spanning 180 degrees. As it is evident from Table 5.3, Fig. 5.6, Fig. 5.7 and Fig. 5.8, the results for the phantom is visually accurate for as few views as 30% (225 views) of the projection views.

6.2 Suggestions for Further Study

Although the reconstruction algorithms proposed in this thesis can solve very large problems such as high-resolution CT reconstruction on a multicore processor, it is also well suited to distributed computing. As a future study, we aim to demonstrate the feasibility of the implementation of the proposed reconstruction algorithms on a cluster of CPUs and/or graphics processing units (GPUs) to speed performance. We expect the result shows speed-ups of several orders of magnitude, with a negligible impact on image accuracy. This solves the compressed sensing-based CT problem much faster which helps us to reconstruct images quickly after the acquisition of the last projection dataset.

One way for decreasing the total scan time and radiation dose is to reduce the number of projections needed to reconstruct the tomographic images which is addressed in this thesis. Another approach is to reduce the time of radiation or radiation intensity at each projection without decreasing the number of projections. Reducing the time of radiation or radiation intensity generates noisy projection data which results in a lower quality reconstructed image. In this case, the goal is to transfer an image whose quality is poor due to low-dose imaging to a higher quality image. One approach is to use a learning algorithm such as sparse dictionary learning [C6.10] to recognize patterns in the training high-dose tomographic images within the same class, then the general dictionaries such as wavelet dictionary which is often used as the regularization term in the compressed sensing reconstruction can be replaced by this learned dictionary. It is expected the learned dictionaries to show a better performance in distinguishing weak structures than general dictionaries.

This study focuses on computer phantoms and preclinical imaging of animals with synchrotron as a test platform. The algorithm benefits can be used to image human subjects with the proximate goals of producing faster and safer scans. This, in turn, will advance the goal of pushing the limits of safe imaging of human subjects in terms of improved resolution in the future.

References

[C6.1] DL. Donoho, “Compressed sensing”. IEEE Trans. Inf. Theory 52, 1289–1306, 2006.

[C6.2] J. Douglas and HH Rachford, “On the numerical solution of heat conduction problems in two or three space variables”, Trans. Amer. Math. Soc; 82:421–439, 1956.

[C6.3] J. Eckstein and D. Bertsekas, “On the Douglas Rachford splitting method and the proximal point algorithm for maximal monotone operators”, Mathematical Programming, vol. 5, pp. 293-318, 1992.

[C6.4] S. Boyd, N. Parikh, E. Chu, B. Peleato, & J. Eckstein. “Distributed optimization and statistical learning via the alternating direction method of multipliers”. Foundations and Trends® in Machine Learning, 3(1), 1-122, 2011.

[C6.5] A. Galántai “On the rate of convergence of the alternating projection method in finite dimensional spaces”. Journal of Mathematical Analysis and Applications. 310(1):30–44, 2005.

[C6.6] F. Natterer. “The Mathematics of Computerized Tomography”. Wiley, New York, 1986.

[C6.7] T. Strohmer, R. Vershynin, “A randomized Kaczmarz algorithm for linear systems with exponential convergence”, J. Fourier analysis Appl; 15:262–278, 2009.

[C6.8] S. L. Wang and L. Z. Liao, "Decomposition method with a variable parameter for a class of monotone variational inequality problems," Journal of Optimization Theory and Applications, 109 (2), 415-429 (2001).

[C6.9] G. L. Zeng, and G. T. Gullberg. "Unmatched projector/backprojector pairs in an iterative reconstruction algorithm." Medical Imaging, IEEE Transactions, 19 (5), 548-555 (2000).

[C6.10] M. Elad and M. Aharon, “Image denoising via sparse and redundant representations over learned dictionaries,” IEEE Trans. Image Process., vol. 15, no. 12, pp. 3736–3745, Dec. 2006.